Low-Scaling Many-Body Perturbation Theory for Nanoscopic Systems

---

Dissertation

zur

Erlangung der naturwissenschaftlichen Doktorwürde (Dr. sc. nat.)

vorgelegt der

Mathematisch-naturwissenschaftlichen Fakultät

der

Universität Zürich

von

Jan Wilhelm

aus

Deutschland

Promotionskommission

Prof. Dr. Jürg Hutter (Vorsitz)

Prof. Dr. Jürg Osterwalder

Dr. Joost VandeVondele

Zürich, 2017

Abstract

Many-body perturbation theory in the form of the *GW* approximation has become the most widely used quantum mechanical tool to predict bandgaps of molecules and materials. Theoretical knowledge of the bandgap is essential to support the design of novel electric devices and photovoltaic materials. A drawback of *GW* is its high computational cost which increases with the fourth order of the system size N, $O(N^4)$. In this thesis, a novel efficient *GW* algorithm based on Gaussian basis functions is presented where the computational cost scales as $O(N^3)$ with the system size. The algorithm is based on a new cubic-scaling method for the Random Phase Approximation (RPA) for the correlation energy. The scaling of RPA can be reduced from $O(N^4)$ to $O(N^3)$ if it is reformulated in the Gaussian basis together with the resolution of the identity (RI) with the overlap metric. Moreover, imaginary time and imaginary frequency integration techniques as well as sparse linear algebra are necessary for cubic-scaling RPA. Cubic-scaling RPA has been applied to two thousand water molecules using a correlation-consistent triple-zeta quality basis which is the largest RPA calculation that has been reported in the literature so far. All algorithms presented in this thesis have been designed in a way that they could be implemented for massively parallel use on modern supercomputer infrastructures which is the key for the application to large systems. As application of the cubic-scaling *GW* algorithm, graphene nanoribbons have been treated. The largest graphene nanoribbon that could be adressed with the cubic-scaling *GW* algorithm contains 1734 atoms which is the largest *GW* calculation that has been reported in the literature so far. The cubic-scaling *GW* algorithm can also be applied to periodic systems in a Γ-point-only approach where a correction scheme is needed. This correction scheme has been specifically derived for the use with Gaussian basis functions.

Deutsche Zusammenfassung

Vielteichenstörungsrechnung in Form der *GW*-Näherung ist ein weit verbreitetes Verfahren, um Bandlücken von Molekülen und Festkörpern quantenmechanisch zu berechnen. Diese Rechnungen können dazu beitragen, neue elektronische Bauteile oder neue Photovoltaik-Materialien zu entwickeln. Ein Nachteil der *GW*-Methode ist der hohe Rechenaufwand, der mit der vierten Potenz der Systemgrösse N wächst, $O(N^4)$. In dieser Arbeit wird ein neuer, effizienter *GW*-Algorithmus basierend auf Gauss-Funktionen vorgestellt, dessen Rechenaufwand mit $O(N^3)$ mit der Systemgrösse skaliert. Der Algorithmus basiert auf einer kubisch skalierenden Methode für die "Random Phase Approximation" (RPA) für die Korrelationsenergie. Die Skalierung von RPA kann von $O(N^4)$ auf $O(N^3)$ reduziert werden, wenn RPA in der Gauss-Basis umformuliert wird und die "Resolution of the Identity" (RI) mit der Überlapp-Metrik verwendet wird. Ausserdem sind Integrationstechniken in imaginärer Zeit und imaginärer Frequenz sowie die Ausnutzung dünn besetzter Matrizen nötig, um kubisch skalierendes RPA zu erhalten. Kubisch skalierendes RPA wurde auf zweitausend Wassermoleküle in einer korrelationskonsistenten tripel-zeta Basis angewendet, was die grösste RPA-Rechnung in der Literatur bisher ist. Alle Algorithmen, die in dieser Arbeit vorgestellt werden, wurden für die Verwendung auf massiv-parallelen modernen Grossrechnern implementiert, was eine Schlüsselrolle für die Anwendung der Algorithmen auf grosse Systeme spielt. Als Anwendung der kubisch skalierenden *GW*-Methode wurden Graphen-Nanoribbon untersucht. Das grösste Graphen-Nanoribbon, das mit der *GW*-Methode behandelt wurde, enthält 1734 Atome, was die grösste *GW*-Rechnung darstellt, die bisher publiziert wurde. Der kubisch-skalierende *GW*-Algorithmus kann auch auf periodische Systeme mit einer Γ-Punkt-Implementierung angewendet werden, wobei eine periodische Korrektur nötig ist, die speziell auf die Implementierung von *GW* mit Gauss-Funktionen angepasst wurde.

Contents

Chapter 1

Introduction

Theoretical knowledge about the electronic structure of molecules and materials is of major interest for science and technology. The calculated total energy of the many-electron system can be employed to determine barrier heights of chemical reactions or the stability of materials. Such theoretical studies can help to improve catalysists [1] or to suggest new materials for photovoltaics [2]. Another important electronic property is the fundamental gap, namely the difference between the first ionization energy and the lowest electron affinity of a material or a molecule. The fundamental gap determines whether a material is an insulator, a semiconductor or exhibits metallic conductance. As an example, computing the fundamental gap of materials can support the design of novel electric devices at the nanoscale, e.g. formed of graphene nanoribbons which are strips of graphene with < 50 nm width [3, 4].

In practice, computing the electronic structure of larger atoms, complex molecules or solids can be a challenging task. The reason is that an exact analytical solution for a system of many interacting electrons has not been achieved yet. Usually, the many-body nature of the problem is tackled with approximate methods and the use of numerical techniques on computers.

For computing the total energy of many-electron systems, density functional theory (DFT) [5] is the by far most established method at present. DFT at one hand offers reasonable accuracy for the total energy at relatively low computational cost which scales as $O(N^3)$ with the number of electrons N in a canonical implementation. Nowadays, DFT in its canonical formulation is routinely applied to systems containing up to ten thousand atoms [6]. DFT can be reformulated in linear-scaling algorithms [7] which are efficient for non-metallic systems with large spatial extend. Exploiting this fact, it was possible to apply linear-scaling DFT to a million hydrogen atoms [8].

For computing the fundamental gap of a material with high accuracy, *GW* [9] is one of the most established methods at present involving $O(N^4)$ computational cost in a canonical implementation which is significantly higher than the computational cost of DFT. *GW* is a method originating from many-body perturbation theory [9] and was first applied to real materials in 1985 by Hybertsen and Louie [10]. Recently, *GW* has been applied to molecules [11–13] for studying the ionization potential, electron affinity and the fundamental gap where good agreement to experimental values has been obtained. The largest application of *GW* to a silicon nanocluster with 1000 atoms was carried out using an optimized $O(N^4)$-scaling algorithm [14]. Compared to other materials, *GW* calculations are computationally less challenging for silicon since low plane-wave cutoffs are already sufficient to reach convergence. In contrast, *GW* studies of more challenging systems as low-dimensional materials like graphene nanoribbons or transistion metal compounds [15] are restricted to by far less atoms at presence.

Many interesting systems can only be modelled if well above thousand atoms are used in the *GW* calculation. As an example, a heterojunction can be build from a graphene nanoribbon when

one half of the nanoribbon is doped with Boron atoms (p-doping) and the other half with nitrogen atoms (n-doping) what already has been demonstrated experimentally [4, 16]. Due to additional charge carriers, the Fermi level of the p-doped side is decreasing while the Fermi level of the n-doped side increases. For a meaningful GW study of this effect, a large extend of the n-doped and the p-doped region is needed in the calculation. Nanoelectrical devices are attached to a surface resulting in a renormalization of the fundamental gap [17] due to screening. This effect can be taken into account by image charge models [17–19] in case of a metallic surface and absence of a chemical bond between device and surface. In all other cases, a large number of surface atoms are required in the GW calculation. In summary, it is highly desirable to develop efficient GW algorithms for the treatment of large systems containing more than thousand atoms. One way to achieve this is to reduce the scaling of the computational cost from $O(N^4)$ to lower order.

Already three low-scaling GW algorithms have been reported in the literature [20–22]: The cubic-scaling algorithm by Foerster *et al.* from 2011 [20] employs a Gaussian basis and locality of electronic interactions. The method has been applied to molecules with a few tens of atoms. Larger applications seem to lie out of reach at presence since a parallel implementation has not been reported which is crucial for applying low-scaling algorithms to large systems as they are intended. The second low-scaling GW algorithm has been reported by Neuhauser *et al.* [21] in 2014 which even scales linearly with the system size and relies on stochastic evaluation of the involved quantities. This algorithm can be easily parallelized and has been applied to a silicon nanocluster with one thousand atoms. However, it remains to be explored whether stochastic GW can be a useful tool for more complex systems than silicon nanoclusters [23]. The recent cubic-scaling GW algorithm by Liu *et al.* [22] is a variant of the GW space-time method by Rojas *et al.* [24] and has been implemented in the VASP package [25]. In this algorithm, a plane-wave basis, real-space grids and sophisticated minimax quadratures for the time and frequency domain are employed. The linear-scaling behaviour in the number of k-points seems to be promising when applying the method to large and numerically challenging periodic systems. For molecular applications of GW as graphene nanoribbons [26], the plane-waves basis is a major bottleneck compared to an atom-centered basis. In practice, all three low-scaling GW algorithms [20–22] could not yet prove their capability for new GW applications to larger systems.

The central objective of this work is to develop a low-scaling GW method which can be applied to systems containing more than thousand atoms. Several steps are necessary for this purpose which are each presented in an individual chapter: In Chapter 2, the theoretical framework of GW is presented. As a first step towards low-scaling GW, canonical $O(N^4)$-scaling GW has been adapted to the Gaussian and plane waves scheme (GPW) [27] which enables efficient calculations for molecules containing hundrets of atoms, see Chapter 3. Periodic boundary conditions require a special treatment for GW calculations in GPW, where details on this special treatment are given in Chapter 4. The focus of Chapter 5 is on the $O(N^3)$-scaling random phase approximation (RPA). RPA is a method for computing the correlation energy of a many-electron system and it is the computationally most expensive step in GW calculations. Cubic-scaling RPA has been implemented for massively parallel use which is the key for the application to large systems. It was possible to apply cubic-scaling RPA to two thousand water molecules. Based on the $O(N^3)$-scaling RPA algorithm, the $O(N^3)$-scaling GW algorithm is presented in Chapter 6. As application of the cubic-scaling GW algorithm, an alternative route to compute the fundamental gap of periodic, one-dimensional armchair graphene nanoribbons from GW is presented: The length of non-periodic ribbons is increased until convergence of the electronic levels is reached. The largest graphene nanoribbon that could be adressed with the cubic-scaling GW algorithm contains 1734 atoms which is the GW calculation with the largest number of atoms in the literature so far. Chapter 7 summarizes the main achievements and gives an overview for further developments.

Chapter 2

Quasiparticle energies in the framework of many-body perturbation theory

In this chapter, the theoretical basics of quasiparticles are introduced, see Sec. 2.1. For computing the energy of a quasiparticle, Hedin's equations or the GW approximation can be used, as shown in Sec. 2.2. For applications, the quasiparticles energies are commonly computed by the G_0W_0 method which employs a start from density functional theory (DFT) as explained in Sec. 2.3. This chapter builds on the work of Hüser *et al.* [28, 29]

2.1 Definition and properties of quasiparticles

One of the central goals in quantum chemistry, theoretical condensed matter physics and materials science is to find approximate solutions $\Psi_i^N(\mathbf{r}_1, \mathbf{r}_2, \ldots, \mathbf{r}_N)$ to the Schrödinger equation of N electrons in an external potential $V_{\text{ext}}(\mathbf{r})$, [28]

$$\hat{H}^N \Psi_i^N(\mathbf{r}_1, \mathbf{r}_2, \ldots, \mathbf{r}_N) = E_i^N \Psi_i^N(\mathbf{r}_1, \mathbf{r}_2, \ldots, \mathbf{r}_N)\,, \tag{2.1}$$

where $\hat{H}$ is the Hamiltonian describing the N-electron system

$$\hat{H}^N = -\sum_{n=1}^{N} \frac{\nabla_n^2}{2} + \sum_{n<m}^{N} \frac{1}{|\mathbf{r}_n - \mathbf{r}_m|} + \sum_{n=1}^{N} V_{\text{ext}}(\mathbf{r}_n)\,. \tag{2.2}$$

The index i in Eq. (2.1) refers to the i-th eigenstate, where $i = 0$ denotes the groundstate.

Occupied and virtual quasiparticle (QP) orbitals $\psi_{i-}^{\text{QP}}(\mathbf{r})$ and $\psi_{i+}^{\text{QP}}(\mathbf{r})$ are defined as [28]

$$\begin{aligned} \psi_{i-}^{\text{QP}}(\mathbf{r}) &= \left\langle \Psi_i^{N-1} \middle| \hat{\Psi}(\mathbf{r}) \middle| \Psi_0^N \right\rangle^*\,, \\ \psi_{i+}^{\text{QP}}(\mathbf{r}) &= \left\langle \Psi_i^{N+1} \middle| \hat{\Psi}^\dagger(\mathbf{r}) \middle| \Psi_0^N \right\rangle\,, \end{aligned} \tag{2.3}$$

where $\hat{\Psi}(\mathbf{r})$ and $\hat{\Psi}^\dagger(\mathbf{r})$ are the field operators annihilating and creating an electron at point $\mathbf{r}$, respectively. According to their definition in Eq. (2.3), the QP orbitals can be interpreted as single-particle wavefunctions in a many-particle system as an atom, a molecule or a solid. In quantum chemistry, the QP orbitals are also referred to as Dyson orbitals.

The corresponding QP energies are defined by

$$\varepsilon_{i-}^{\text{QP}} = E_0^N - E_i^{N-1} \tag{2.4}$$

$$\varepsilon_{i+}^{\text{QP}} = E_i^{N+1} - E_0^N\,. \tag{2.5}$$

They represent the excitation energies of the $(N\pm1)$-particle system relative to E_0^N and thus correspond to electron addition and removal energies. According to the definition of the chemical potential μ, it holds that $\varepsilon_{i-}^{\mathrm{QP}} > \mu$ and $\varepsilon_{i+}^{\mathrm{QP}} \leq \mu$. Having noted this we can drop the $\pm$ subscripts on the QP states and energies.

Then, the fundamental gap is defined as

$$E_{\mathrm{gap}} = \varepsilon_{0+}^{\mathrm{QP}} - \varepsilon_{0-}^{\mathrm{QP}} \,. \tag{2.6}$$

The fundamental gap is an important property of materials since it strongly affects their electric properties: A very small or vanishing fundamental gap is leading to metallic behaviour while an insulator is charaterized by a high fundamental gap.

Now, we introduce the formulas for computing the QP energies in practice. We assume a weakly correlated system where a single Slater determinant is a good approximation to the full many-body wavefunction. In this case, it can be shown by many-body perturbation theory that ψ_i^{QP} and $\varepsilon_i^{\mathrm{QP}}$ can be computed as solutions of the QP equation

$$\left(-\frac{\nabla^2}{2} + v_{\mathrm{H}}(\mathbf{r}) + v_{\mathrm{ext}}(\mathbf{r})\right)\psi_i^{\mathrm{QP}}(\mathbf{r}) + \int d\mathbf{r}'\; \Sigma(\mathbf{r},\mathbf{r}',\varepsilon_i^{\mathrm{QP}})\,\psi_i^{\mathrm{QP}}(\mathbf{r}') = \varepsilon_i^{\mathrm{QP}}\psi_i^{\mathrm{QP}}(\mathbf{r}) \tag{2.7}$$

where v_{H} denotes the Hartree potential and Σ the exchange-correlation self-energy which contains the whole electron-electron interaction beyond the Hartree interaction. Note that the Hartree-Fock or a density functional approximation to the self-energy leads to an energy-independent function $\Sigma^{\mathrm{HF/DF}}(\mathbf{r},\mathbf{r}')$. As a consequence, using $\Sigma^{\mathrm{HF/DF}}(\mathbf{r},\mathbf{r}')$ in Eq. (2.7) does not guarantee to yield correct QP wavefunctions ψ_i^{QP} and, more importantly, correct QP energies $\varepsilon_i^{\mathrm{QP}}$.

2.2 Many-body perturbation theory: Hedin's equations and *GW* approximation

An exact way of calculating the self-energy from Eq. (2.7) is given by a set of five coupled equations, known as Hedin's equations [9]:

$$\text{self-energy:} \qquad \Sigma(1,2) = i\int d(34)G(1,3)\Gamma(3,2,4)W(4,1^+)\,, \tag{2.8}$$

$$\text{Green's function:} \qquad G(1,2) = G_0(1,2) + \int d(34)G_0(1,3)\Sigma(3,4)G(4,2)\,, \tag{2.9}$$

$$\text{screened interaction:} \qquad W(1,2) = V(1,2) + \int d(34)V(1,3)P(3,4)W(4,2)\,, \tag{2.10}$$

$$\text{polarization:} \qquad P(1,2) = -i\int d(34)G(1,3)G(4,1^+)\Gamma(3,4,2)\,, \tag{2.11}$$

$$\text{vertex function:} \qquad \Gamma(1,2,3) = \delta(1,2)\delta(1,3) + \int d(4567)\frac{\partial\Sigma(1,2)}{\partial G(4,5)}G(4,6)G(7,5)\Gamma(6,7,3)\,, \tag{2.12}$$

where the argument has been combined to $(j) \equiv (\mathbf{r}_j, t_j)$ and the bare Coulomb interaction is given by $V(1,2) = 1/|\mathbf{r}_1 - \mathbf{r}_2|\delta(t_1 - t_2)$. The non-interacting Green's function

$$G_0(\mathbf{r},\mathbf{r}';\omega) = \sum_i \frac{\psi_i(\mathbf{r})^*\psi_i(\mathbf{r}')}{\omega - \varepsilon_i + i\eta\,\mathrm{sgn}(\varepsilon_i - \mu)} \tag{2.13}$$

can be computed using the single-particle wavefunctions $\psi_i(\mathbf{r})$ from the non-interacting problem [Eq. (2.7) with $\Sigma = 0$], a positive infinitesimal number η and the chemical potential μ. In principle, the equations (2.8) - (2.13) can be solved self-consistently which has not yet been done in practice due to their complicated structure.

A simple ansatz can be made by neglecting the second term in the vertex function, which yields

$$P(1,2) = -iG(1,2)G(2,1^+) \qquad \text{and} \qquad \Sigma^{GW}(1,2) = iG(1,2)W(1,2)\,. \tag{2.14}$$

Due to the form of the self-energy, this approximation is called GW approximation. We interpret this choice when comparing to Hartree-Fock theory, in which the self-energy is given as a product of the Green's function and the bare Coulomb interaction:

$$\Sigma^{\mathrm{HF}}(1,2) = iG(1,2)V(1,2)\,. \tag{2.15}$$

Here, electron-electron interaction only occurs through the Hartree- and the exchange potential, that means that there is no correlation – the electrons are moving independently of their Coulomb repulsion beyond the Hartree mean-field interaction. On the other hand, correlation is to a large extent determined by screening. Thus, by replacing the bare Coulomb interaction V by the screened interaction W in the self-energy, dynamical correlation is introduced in the GW approximation by means of screening.

In real space and time domain, the GW self-energy is simply given as a product, see Eq. (2.14), which turns into a convolution in frequency domain,

$$\Sigma^{GW}(\mathbf{r},\mathbf{r}',\omega) = \frac{i}{2\pi}\int d\omega' e^{i\delta\omega'} G(\mathbf{r},\mathbf{r}',\omega-\omega')W(\mathbf{r},\mathbf{r}',\omega')\,, \tag{2.16}$$

where the inifinitesimal δ ensures the correct time-ordering in case of a static potential, $W(\omega = 0)$.

2.3 G_0W_0 method for computing quasiparticle energies

In practice, Kohn-Sham (KS) orbitals ψ_i^{DFT} and eigenvalues $\varepsilon_i^{\mathrm{DFT}}$ from a DFT calculation

$$\left(-\frac{\nabla^2}{2} + v_{\mathrm{H}}(\mathbf{r}) + v_{\mathrm{ext}}(\mathbf{r}) + v_{\mathrm{xc}}(\mathbf{r})\right)\psi_i^{\mathrm{DFT}}(\mathbf{r}) = \varepsilon_i^{\mathrm{DFT}}\psi_i^{\mathrm{DFT}}(\mathbf{r}) \tag{2.17}$$

are often used as input for a GW calculation. In the widely used G_0W_0 scheme, the quasiparticle wavefunctions are approximated by the DFT wavefunctions, $\psi_i^{\mathrm{QP}} \approx \psi_i^{\mathrm{DFT}}$. This approximation is justified in the sense that the exchange-correlation potential $v_{\mathrm{xc}}(\mathbf{r})$ is small and has few spatial structure compared to the kinetic energy, the Hartree potential and the external potential. Therefore, the KS orbitals can be expected to be close to the QP orbitals from Eq. (2.7). The G_0W_0 self-energy $\Sigma^{G_0W_0}$ is computed from Eq. (2.14) using the non-interacting DFT Green's function G_0 from Eq. (2.13),

$$G_0(\mathbf{r},\mathbf{r}';\omega) = \sum_i \frac{\psi_i^{\mathrm{DFT}}(\mathbf{r})\psi_i^{\mathrm{DFT}}(\mathbf{r}')}{\omega - \varepsilon_i^{\mathrm{DFT}} + i\eta\,\mathrm{sgn}(\varepsilon_i^{\mathrm{DFT}} - \mu)}\,. \tag{2.18}$$

to approximate the interacting Green's function G.

For the quasiparticle energies, we start from Eq. (2.7) inserting the G_0W_0 self-energy $\Sigma^{G_0W_0}$ with $\psi_i^{\mathrm{DFT}} \approx \psi_i^{\mathrm{QP}}$ on both sides and integrating over $\mathbf{r}$,

$$\left\langle\psi_i^{\mathrm{DFT}}\right| -\frac{\nabla^2}{2} + v_{\mathrm{H}} + v_{\mathrm{ext}}\left|\psi_i^{\mathrm{DFT}}\right\rangle + \left\langle\psi_i^{\mathrm{DFT}}\left|\Sigma^{G_0W_0}(\varepsilon_i^{\mathrm{QP}})\right|\psi_i^{\mathrm{DFT}}\right\rangle = \varepsilon_i^{\mathrm{QP}}\,. \tag{2.19}$$

Using Eq. (2.17) and first order Taylor expansion of $\Sigma(\varepsilon_i^{\mathrm{QP}})$ around $\varepsilon_i^{\mathrm{DFT}}$, we obtain from Eq. (2.19)

$$\varepsilon_i^{\mathrm{DFT}} - \left\langle \psi_i^{\mathrm{DFT}} \middle| v_{\mathrm{xc}} \middle| \psi_i^{\mathrm{DFT}} \right\rangle + \left\langle \psi_i^{\mathrm{DFT}} \middle| \Sigma^{G_0W_0}(\varepsilon_i^{\mathrm{DFT}}) + (\varepsilon_i^{\mathrm{QP}} - \varepsilon_i^{\mathrm{DFT}}) \cdot \partial\Sigma^{G_0W_0}/\partial\omega|_{\omega=\varepsilon_i^{\mathrm{DFT}}} \middle| \psi_i^{\mathrm{DFT}} \right\rangle = \varepsilon_i^{\mathrm{QP}} \,. \tag{2.20}$$

After rearranging Eq. (2.20), we arrive at

$$\varepsilon_i^{\mathrm{QP}} = \varepsilon_i^{\mathrm{DFT}} + Z_i \left\langle \psi_i^{\mathrm{DFT}} \middle| \Sigma^{G_0W_0}(\varepsilon_i^{\mathrm{DFT}}) - v_{\mathrm{xc}} \middle| \psi_i^{\mathrm{DFT}} \right\rangle , \qquad Z_i = \left(1 + \partial\Sigma^{G_0W_0}/\partial\omega|_{\omega=\varepsilon_i^{\mathrm{DFT}}}\right)^{-1} . \tag{2.21}$$

From Eq. (2.21), we see that the exchange-correlation part from DFT is subtracted from the DFT-eigenvalue $\varepsilon_i^{\mathrm{DFT}}$, while the self-energy from G_0W_0 is added to account for exchange and correlation effects. In this way, correlation from dynamic screening is included in the G_0W_0 quasiparticle energies. A more detailed introduction to the G_0W_0 method is given in Sec. 3.2 with a focus on the implementation in a Gaussian basis.

Chapter 3

GW in the Gaussian and plane waves scheme with application to linear acenes

The following chapter is a reprint of Ref. [30]. We present an implementation of G_0W_0 and eigenvalue-self-consistent *GW* (ev*GW*) in the Gaussian and plane waves scheme for molecules. We calculate the correlation self-energy for imaginary frequencies employing the resolution of the identity. The correlation self-energy for real frequencies is then evaluated by analytic continuation. This technique allows an efficient parallel implementation and application to systems with several hundreds of atoms. Various benchmark calculations are presented. In particular, the convergence with respect to the most important numerical parameters is assessed for the benzene molecule. Comparisons with respect to other G_0W_0 implementations are reported for a set of molecules, while the performance of the method has been measured for water clusters containing up to 480 atoms in a cc-TZVP basis. Additionally, G_0W_0 has been applied for studying the influence of the ligands on the gap of small CdSe nanoparticles. ev*GW* has been employed to calculate the HOMO-LUMO gaps of linear acenes, linear chains formed of connected benzene rings. Distinct differences between the closed and the open-shell (broken-symmetry) ev*GW* HOMO-LUMO gaps for long acenes are found. In future experiments, a comparison of measured HOMO-LUMO gaps and our calculated ev*GW* values may be helpful to determine the electronic ground state of long acenes.

3.1 Introduction

In recent years, *GW* with localized basis sets has emerged as an accurate method for the calculation of quasiparticle energies of molecules [11–13, 20, 21, 31–44]. Additionally, in combination with the Bethe-Salpeter equation, *GW* is a promising method for computing molecular electronic excitations with high accuracy [34, 45–50]. Most of the traditional *GW* implementations employ a plane-wave (PW) or augmented plane-wave (APW) basis [10, 51–68]. While the main field of application of PW and APW *GW* is still the condensed phase, they have also been employed recently to calculate quasiparticle levels of molecules [14, 28, 69, 70]. When treating molecules, the main advantage of a localized basis compared to PWs is the reduced number of basis functions required to represent the Hamiltonian and thus the wavefunctions. The number of PWs can be a factor 100-1000 larger compared to that of a localized basis, [71] mainly due to the need of a large supercell in the former method in order to decouple the periodic images. On the other hand, the generation of a localized basis that provides systematic convergence is much harder to be obtained and the convergence of the *GW* quasiparticle energies with respect to the basis parameters is still under investigation. [31, 36, 38, 40]

The computational effort of G_0W_0 is quickly growing for increasing system size N with a scaling $O(N^4)$ for state-of-the-art implementations [13]. As a consequence, an efficient implementation for high-performance computing is needed to study large systems with G_0W_0 [14, 52]. As basis of our G_0W_0 implementation in the Gaussian and plane waves scheme [27] in CP2K [72,73], we employ the previous efficient implementation of wavefunction correlation methods [74–77] which enabled large-scale molecular-dynamics and Monte Carlo simulations based on second order Møller-Plesset (MP2) and random phase approximation (RPA) total energies [78–80]. We use the G_0W_0 framework in the resolution-of-the-identity approach as elaborated by Ren *et al.* [13] Our G_0W_0 methodology can be applied to systems containing hundreds of atoms. As starting point for G_0W_0, a wide range of local, semilocal, hybrid and range-separated hybrid functionals can be employed [81]. In agreement with the literature [13, 14, 31, 40, 46, 47, 82–84], we find that the PBE0 [85] and the tuned CAM-B3LYP [86] starting points perform remarkably well for molecules with an average deviation of $0.1-0.2$ eV between the computed G_0W_0-HOMO energy and the experimental vertical ionization potential [87]. Moreover, our G_0W_0 and evGW implementation can treat systems with unpaired electrons.

We apply our GW implementation to compute the HOMO-LUMO gap of linear acenes, molecules consisting of repeating units of benzene rings. This application is motivated by a recent study by Korytár *et al.* [88] indicating that the HOMO-LUMO gaps of acenes may not decay monotonously with increasing number of benzene rings, but can oscillate. The reason is the presence of a level crossing in the one-dimensional band structure of polyacene [89] which is shifted from the Γ-point. Such HOMO-LUMO gap oscillations are well-known in carbon nanotubes [90, 91] and armchair graphene nanoribbons [3,92–94] due to the presence of the Dirac cone in the band structure of graphene [95]. Remarkably, the HOMO-LUMO gap oscillations in acenes on the level of closed-shell PBE [96] have not been reported before Ref. [88] despite of the intensive research on the electronic ground state properties of acenes [97–104], which is driven by organic electronics [105–109] and photovoltaics [110–113]. In Ref. [88], G_0W_0 HOMO-LUMO gaps have been presented up to tetracene. We report G_0W_0 and eigenvalue-selfconsistent GW [11,34] calculations of the HOMO-LUMO gap up to 11-acene.

This chapter is organized as follows: First, we introduce the GW methodology of the implementation (Sec. 3.2). In Sec. 3.3, we perform extensive benchmark calculations with our implementation: the convergence of a wide range of numerical parameters is illustratively tested for benzene. We report execution times, system size scaling and the parallel speedup measured for water clusters containing up to 160 molecules. Also, G_0W_0-HOMO energies of molecules and G_0W_0 gaps of CdSe nanoclusters are reported. In Sec. 3.4, we apply eigenvalue-self-consistent GW to predict the HOMO-LUMO gap of linear acenes.

3.2 Theory and implementation

In this section, the theoretical and computational framework of the G_0W_0 implementation is briefly presented. In Sec. 3.2, we describe the evaluation of the quasiparticle energies starting from the precomputed frequency-dependent correlation-self-energy $\Sigma^c(\omega)$. [13, 31] The resolution-of-the-identity (RI) approximation for four-center two electron repulsion integrals (ERIs) is introduced in Sec. 4.2. [75] In Sec. 3.2, we apply RI to G_0W_0 and we give the working expressions as employed in the implementation. [13, 75]

The following index notation has been adopted: μ, ν, λ refer to Gaussian functions ϕ of the primary basis, n, m, k, l refer to general molecular orbitals (MOs) ψ, i to an occupied MO, a to a virtual one and P, Q to auxiliary RI Gaussian basis functions φ.

Starting point and quasiparticle energies

For G_0W_0, we start from a self-consistent generalized Kohn-Sham (GKS) DFT [5] calculation, including hybrid functionals and Hartree-Fock (HF) [114]. The total energy of a many-electron system in GKS-DFT is obtained by solving the eigenvalue problem

$$h^0\psi_n(\mathbf{r}) + \int d\mathbf{r}'\, v^{\mathrm{xc}}(\mathbf{r},\mathbf{r}')\psi_n(\mathbf{r}') = \varepsilon_n\psi_n(\mathbf{r})\,. \tag{3.1}$$

h^0 contains the external and the Hartree potential as well as the kinetic energy. $v^{\mathrm{xc}}(\mathbf{r},\mathbf{r}')$ denotes the exchange-correlation potential which is local for most non-hybrid density functional approximations, $v^{\mathrm{xc}}(\mathbf{r},\mathbf{r}') = \delta(\mathbf{r},\mathbf{r}')v^{\mathrm{xc}}_{\mathrm{KS}}(\mathbf{r})$. In HF, exact exchange [115–117]

$$\Sigma^{\mathrm{x}}(\mathbf{r},\mathbf{r}') = -\sum_i^{\mathrm{occ}} \psi_i(\mathbf{r})\psi_i(\mathbf{r}')v(\mathbf{r},\mathbf{r}') \tag{3.2}$$

is the only term included in $v^{\mathrm{xc}}(\mathbf{r},\mathbf{r}')$, where $v(\mathbf{r},\mathbf{r}') = 1/|\mathbf{r}-\mathbf{r}'|$ denotes the bare Coulomb interaction. In this case the potential is fully non-local and no correlation effects are accounted. Note that the spin variable has been dropped for convenience.

In the following, we briefly introduce the G_0W_0 method giving the equation to compute the quasiparticle energies $\varepsilon_n^{G_0W_0}$. For a concise introduction into quasiparticles and the GW method in the Green's function framework, we refer to the work of Hüser *et al.* [28] By construction, the GKS-DFT MOs $\psi_n(\mathbf{r})$ and their corresponding eigenvalues ε_n are auxiliary quantities for computing the total energy of the many-body problem. In contrast, the poles of the Green's function correspond to vertical electron addition or removal energies and consequently, these poles are interpreted as quasiparticle energies. [28] In G_0W_0, the MOs from GKS-DFT serve as quasiparticle wavefunctions and only their quasiparticle energies (poles of the Green's function) are computed by means of G_0W_0:

$$\varepsilon_n^{G_0W_0} = \varepsilon_n + Z_n(n|\Sigma^{\mathrm{x}} + \mathrm{Re}\,\Sigma^{\mathrm{c}}(\varepsilon_n) - v^{\mathrm{xc}}|n)\,, \tag{3.3}$$

where $\Sigma^{\mathrm{c}}(\varepsilon)$ stands for the G_0W_0 correlation self-energy which is calculated according to the algorithm described in the following sections. The renormalization factor Z_n,

$$Z_n = \left(1 - \partial(n|\mathrm{Re}\,\Sigma^{\mathrm{c}}(\omega)|n)/\partial\omega|_{\omega=\varepsilon_n}\right)^{-1}\,, \tag{3.4}$$

accounts for the linearized energy-dependence of $\Sigma^{\mathrm{c}}(\omega)$. [31]

RI approximation

The four-center electron repulsion integrals (ERIs) are of central importance for calculating the correlation self-energy $\Sigma^{\mathrm{c}}(\varepsilon)$ in the G_0W_0 approximation. These integrals, in Mulliken notation, are defined as

$$(nm|kl) := \int d\mathbf{r}\,d\mathbf{r}'\,\psi_n(\mathbf{r}')\psi_m(\mathbf{r}')\psi_k(\mathbf{r})\psi_l(\mathbf{r})v(\mathbf{r},\mathbf{r}') \tag{3.5}$$

where $v(\mathbf{r},\mathbf{r}') = 1/|\mathbf{r}-\mathbf{r}'|$ is the Coulomb interaction. Within the RI approximation [118,119] based on the Coulomb metric [120], these integrals are factorized to

$$(nm|kl)_{\mathrm{RI}} = \sum_{PQ}(nm|P)V^{-1}_{PQ}(Q|kl)\,. \tag{3.6}$$

Here, V_{PQ}^{-1} is the inverse of the Coulomb matrix V_{PQ}:

$$V_{PQ} \equiv (P|Q) = \int d\mathbf{r} d\mathbf{r}' \varphi_P(\mathbf{r}') \varphi_Q(\mathbf{r}) v(\mathbf{r}, \mathbf{r}') \,. \tag{3.7}$$

The matrix elements $(nm|P)$ are given by

$$(nm|P) = \sum_{\mu\nu} C_{\mu n} C_{\nu m} (\mu\nu|P) \,, \qquad (\mu\nu|P) = \int d\mathbf{r} d\mathbf{r}' \phi_\mu(\mathbf{r}') \phi_\nu(\mathbf{r}') \varphi_P(\mathbf{r}) v(\mathbf{r}, \mathbf{r}') \tag{3.8}$$

where the $C_{\lambda k}$ are the MO coefficients obtained as solution of the KS equations.

The RI-basis functions P, Q are Gaussian functions, which are local for gas phase systems and periodically repeated for the condensed phase. The two- and three-center ERIs are computed by direct integration between the Gaussian basis functions [bra in Eq. (3.7) and (3.8)] and the electrostatic potential associated to auxiliary RI Gaussian basis functions [ket in Eq. (3.7) and (3.8)]. The electrostatic potential is obtained in a plane wave basis set after solving the Poisson equation in Fourier space. The advantage of this method is that, for each electrostatic potential, the evaluation of the matrix elements of Eq. (3.8) is obtained in linear scaling time, since only integrals over overlapping basis function product $\phi_\mu(\mathbf{r}')\phi_\nu(\mathbf{r}')$ need to be evaluated. Additionally, due to the introduction of an auxiliary PW basis for the expansion of the electrostatic densities, periodic boundary conditions can be included straightforwardly. On the other hand, pseudopotentials have to be employed in order to remove core states and to provide smooth densities. For more details, we refer to Ref. [75].

The main advantage of the RI approximation [Eq. (5.4)] is that four center electron repulsion integrals of the type $(nm|kl)$ are computed from three and two center ERIs. This allows to reduce the storage requirement as well as the computational effort for the integral evaluation and subsequent matrix operations without significant loss of accuracy. [119, 121]

Since the Coulomb matrix V_{PQ} is positive definite, the calculation of V_{PQ}^{-1} can be efficiently performed by a Cholesky followed by the efficient inversion of the triangular matrix $\mathbf{L}$, decomposition of V_{PQ},

$$V_{PQ} = \sum_R L_{PR} L_{RQ}^T \,, \qquad V_{PQ}^{-1} = \sum_R L_{PR}^{-T} L_{RQ}^{-1} \,. \tag{3.9}$$

In this way, the factorization of the $(nm|kl)$ ERIs can be expressed in a compact form as

$$(nm|kl)_{\mathrm{RI}} = \sum_P B_P^{nm} B_P^{kl} \,, \qquad B_P^{nm} = \sum_R (nm|R) L_{PR}^{-1} \,. \tag{3.10}$$

G_0W_0 self-energy

In the *GW* approximation [9], the G_0W_0 self-energy $\Sigma = \Sigma^{\mathrm{x}} + \Sigma^{\mathrm{c}}$ for an imaginary frequency $i\omega$ is given by [13]

$$\Sigma(\mathbf{r}, \mathbf{r}', i\omega) = -\frac{1}{2\pi} \int_{-\infty}^{\infty} d\omega' G_0(\mathbf{r}, \mathbf{r}', i\omega - i\omega') W_0(\mathbf{r}, \mathbf{r}', i\omega') \tag{3.11}$$

where $G_0(\mathbf{r}, \mathbf{r}', i\omega)$ is the Green's function of the KS reference system [Eq. (3.1)],

$$G_0(\mathbf{r}, \mathbf{r}', i\omega) = \sum_m \frac{\psi_m(\mathbf{r}')\psi_m(\mathbf{r})}{i\omega + \varepsilon_{\mathrm{F}} - \varepsilon_m} \,, \tag{3.12}$$

and $W_0(\mathbf{r}, \mathbf{r}', i\omega)$ the screened Coulomb interaction,

$$W_0(\mathbf{r}, \mathbf{r}', i\omega) = \int d\mathbf{r}'' \epsilon^{-1}(\mathbf{r}, \mathbf{r}'', i\omega) v(\mathbf{r}'', \mathbf{r}') \,. \tag{3.13}$$

The dielectric function $\epsilon(\mathbf{r}, \mathbf{r}', i\omega)$ is defined as

$$\epsilon(\mathbf{r}, \mathbf{r}', i\omega) = \delta(\mathbf{r}, \mathbf{r}') - \int d\mathbf{r}'' v(\mathbf{r}, \mathbf{r}'') \chi(\mathbf{r}'', \mathbf{r}', i\omega) \,. \tag{3.14}$$

where the density response $\chi(\mathbf{r}, \mathbf{r}', i\omega)$ is given by

$$\chi(\mathbf{r}, \mathbf{r}', i\omega) = 2 \sum_{i}^{\text{occ}} \sum_{a}^{\text{virt}} \psi_a(\mathbf{r}') \psi_i(\mathbf{r}') \psi_i(\mathbf{r}) \psi_a(\mathbf{r}) \frac{\varepsilon_i - \varepsilon_a}{\omega^2 + (\varepsilon_i - \varepsilon_a)^2} \,. \tag{3.15}$$

In order to employ Eq. (3.3), we calculate the (n, n)-diagonal matrix element of $\Sigma(i\omega)$,

$$\Sigma_n(i\omega) \equiv (n|\Sigma(i\omega)|n) = \int d\mathbf{r} d\mathbf{r}' \psi_n(\mathbf{r}') \psi_n(\mathbf{r}) \Sigma(\mathbf{r}, \mathbf{r}', i\omega) \tag{3.16}$$

for considered quasiparticle state n and for a given set of $i\omega$ grid points. By considering N_{aux} RI-auxiliary Gaussian functions P and Q, inserting the Eqs. (3.11) – (3.13), (3.14), (3.15) and then Eq. (5.4) and (5.10) into Eq. (3.16), we obtain [13]

$$\Sigma_n(i\omega) = -\frac{1}{2\pi} \sum_m \int_{-\infty}^{\infty} d\omega' \frac{1}{i(\omega - \omega') + \varepsilon_{\text{F}} - \varepsilon_m} \sum_{PQ} B_P^{nm} \left[1 - \Pi(i\omega')\right]^{-1}_{PQ} B_Q^{mn} \,, \tag{3.17}$$

where $\Pi_{PQ}(i\omega)$ is the $N_{\text{aux}} \times N_{\text{aux}}$ matrix representation of the density response function,

$$\Pi_{PQ}(i\omega) = 2 \sum_{ia} B_P^{ia} \frac{\varepsilon_i - \varepsilon_a}{\omega^2 + (\varepsilon_i - \varepsilon_a)^2} B_Q^{ia} \,. \tag{3.18}$$

For numerical stability and to avoid the RI-approximation for Σ_n^{x}, we calculate the exact exchange self-energy by means of Eq. (3.2):

$$\Sigma_n^{\text{x}} := (n|\Sigma^{\text{x}}|n) = -\sum_{i}^{\text{occ}} (ni|in) \,. \tag{3.19}$$

The exchange self-energy [Eq. (3.19)] is subtracted from the total self-energy to obtain the correlation part. Similarly to Eq. (3.17), we get [39]

$$\Sigma_n^{\text{c}}(i\omega) = -\frac{1}{2\pi} \sum_m \int_{-\infty}^{\infty} d\omega' \frac{1}{i(\omega - \omega') + \varepsilon_{\text{F}} - \varepsilon_m} \sum_{PQ} B_P^{nm} \left[\left[1 - \Pi(i\omega')\right]^{-1}_{PQ} - \delta_{PQ} \right] B_Q^{mn} \,. \tag{3.20}$$

The integration over ω' is computed employing a Clenshaw-Curtis grid [122] as proposed by Eshuis *et al.* [123] We employ the same grid to evaluate $\Sigma_n^{\text{c}}(i\omega)$.

To evaluate Eq. (3.3), we obtain the real-frequency self-energy by means of analytic continuation [24, 124] which has been shown to be accurate [13, 38, 39, 59, 125, 126]. In this approach, $\Sigma_n^{\text{c}}(i\omega)$ from Eq. (4.22) is fit to a two-pole model P_n for every quasiparticle state n ($N_{\text{poles}} = 2$):

$$\Sigma_n^{\text{c}}(i\omega) \simeq P_n(i\omega) := \sum_{j=1}^{N_{\text{poles}}} \frac{a_{n,j}}{i\omega + b_{n,j}} + a_{n,0} \,. \tag{3.21}$$

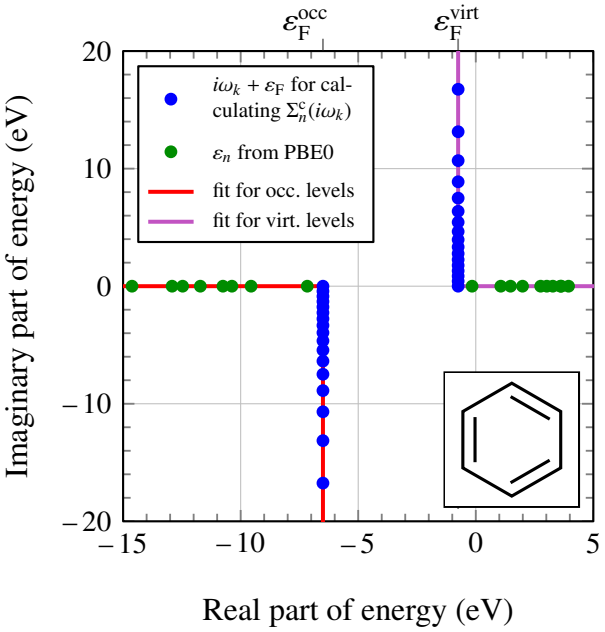

Figure 3.1: Clenshaw-Curtis grid points $i\omega_k$ (blue dots), fit of the self-energy [Eq. (4.22)] on imaginary frequencies (red and magenta lines) and evaluation of the fitting function at the GKS eigenvalues ε_n (green dots). We set the Fermi level ε_F in Eq. (4.22) as $\varepsilon_{HOMO} + 0.3\,eV$ for occupied orbitals and as $\varepsilon_{LUMO} - 0.3\,eV$ for virtual orbitals.

The complex coefficients $a_{n,j}$ and $b_{n,j}$ are determined by a nonlinear least-square fit, solved with a Levenberg-Marquardt algorithm. During the fitting procedure, we apply the constraint $P_n(0) = \Sigma_n^c(i0)$ to fix the fit at $\omega = 0$ to the computed self-energy $\Sigma_n^c(i0)$. To avoid branch cuts, the self-energy of an occupied orbital n is fitted for negative imaginary frequencies while the self-energy of a virtual orbital is fitted for positive imaginary frequencies, see Fig. 3.1. [24, 124] As also sketched in Fig. 3.1, we set the Fermi level ε_F in Eq. (4.22) for occupied orbitals n as $\varepsilon_F = \varepsilon_{HOMO} + 0.3\,eV$ and for virtual orbitals n as $\varepsilon_F = \varepsilon_{LUMO} - 0.3\,eV$. The advantage of this procedure is that the fit has an anchor point $\Sigma_n^c(i0)$ close to the eigenvalues ε_n of the SCF, see Fig. 3.1.

By replacing $i\omega$ with ω in P_n in Eq. (3.21), the self-energy can be evaluated on the real-frequency axis. Then, Eq. (3.3) to determine the quasiparticle energies turns into the working expression

$$\varepsilon_n^{G_0W_0} = \varepsilon_n + Z_n \left[\Sigma_n^x + \mathrm{Re}\, P_n(\varepsilon_n - \varepsilon_F) - v_{nn}^{xc}\right] , \tag{3.22}$$

with $Z_n = 1/[1 - \mathrm{Re}\, P_n'(\varepsilon_n - \varepsilon_F)]$ and the diagonal element v_{nn}^{xc} of the exchange-correlation matrix.

3.3 G_0W_0 benchmark calculations

In this section, we report G_0W_0 benchmark results to validate the implementation. The section is organized as follows: In Sec. 3.3, we give the computational parameters which have been used for all calculations. Then, we investigate the convergence of the benzene-G_0W_0-HOMO energy and the G_0W_0-HOMO-LUMO gap with respect to the most important numerical parameters (Sec. 3.3). Execution times, parallel speedup and the system size scaling of the implementation are reported in Sec. 3.3. As an application of the implementation, we study the influence of different ligands on the gap of CdSe nanoclusters and we compare G_0W_0-HOMO energies of small molecules to experimental values and other G_0W_0 implementations (Sec. 3.3).

Computational details

For all calculations reported here, we employ the Gaussian and plane waves scheme (GPW) [27] for the underlying generalized Kohn-Sham (KS) equations as implemented in CP2K [72, 73, 127–

129]. The GPW scheme makes use of a Gaussian basis to expand molecular orbitals and an auxiliary plane-wave basis for the expansion of the electronic density. This dual representation allows for evaluating the Hartree contribution to the KS matrix in linear scaling time at full accuracy. [127] In order to have an efficient expansion of the density in plane waves, core electrons are replaced by pseudopotentials. We use dual-space pseudopotentials of the Goedecker-Teter-Hutter (GTH) type [130,131] specifically parameterized for LDA [132], PBE [96], PBE0 [85] and B3LYP [86].

Regarding the Gaussian basis, we employ valence-only correlation-consistent basis sets [133, 134], generated specifically for the use with GTH pseudopotentials [135]. The basis sets have been labeled as cc-DZVP, cc-TZVP, cc-QZVP and cc-5ZVP, denoting double, triple, quadruple and quintuple-zeta quality, respectively. For each primary basis set, the corresponding auxiliary RI basis has been generated [75] according to the procedure proposed by Weigend *et al.* [136]

The plane-wave cutoff for the DFT part of the calculations is $E_{\text{cut}} = 1200\,\text{Ry}$ to guarantee convergence of the SCF, at small cost compared to the *GW* calculations. For the calculations of two- and three-center ERIs for *GW*, we employed a high quality plane-wave cutoff of $E_{\text{cut}} = 300\,\text{Ry}$ for the expansion of the RI fitting densities. Gas phase systems have been computed using cluster boundary conditions for solving the Poisson equation [137].

As input geometries for the SCF and the subsequent G_0W_0 calculations, we take B3LYP-relaxed molecular geometries from the nistgov database [87]. As general computational G_0W_0 setup, we use 100 grid points for the frequency integration in Eq. (4.22) and a Fermi level which is 0.3 eV above $\varepsilon_{\text{HOMO}}$ for occupied MOs and 0.3 eV below $\varepsilon_{\text{LUMO}}$ for virtual MOs. The range for fitting the correlation self-energy [Eq. (3.21)] is chosen as $[0, \pm 10\,\text{eV}]i$ on the imaginary-frequency axis, where '−' refers to quasiparticles and '+' to quasiholes.

Convergence of numerical parameters: the benzene molecule

In this section, we present convergence tests of the HOMO level and the HOMO-LUMO gap of benzene for the PBE0 starting point with respect to the main computational parameters. Similar convergence has been obtained for other systems and different starting wavefunctions. We are also testing auxiliary density matrix methods (ADMM) [138, 139] for the approximate, but faster computation of exact exchange at the SCF level. The reference value for benzene is $\varepsilon_{\text{HOMO}}^{G_0W_0@\text{PBE0}} = -9.29\,\text{eV}$, which has been obtained employing the cc-5ZVP basis and numerical parameters as described in the previous section. Our reference is in good agreement with the experimental vertical ionization potential of 9.24 eV [140] and G_0W_0@PBE0 HOMO energies from other implementations (−9.20 eV from Ref. [13] and −9.32 eV from Ref. [14]).

Primary basis set

In Figure 3.2, the convergence and the extrapolation of the G_0W_0@PBE0-HOMO energy with the size of the basis set is sketched. As previously reported in the literature [31, 36, 38, 40], the convergence of single G_0W_0 quasiparticle levels in a Gaussian basis is very slow. An accuracy of 0.1 eV compared to the complete-basis limit is only reached at the level of a cc-5ZVP basis set, which means as many as 816 basis functions for the benzene molecule.

Figure 3.3 displays the convergence of the G_0W_0@PBE0-HOMO-LUMO gap with the size of the basis set. As previously reported in the literature [11, 35, 40, 45, 46], the convergence of the G_0W_0-HOMO-LUMO gap in an augmented Gaussian basis is very fast and already reached using an aug-DZVP basis with an accuracy of better than 0.02 eV for benzene. In contrast, the HOMO-LUMO gap converges much slower employing a correlation-consistent basis without augmentation functions.

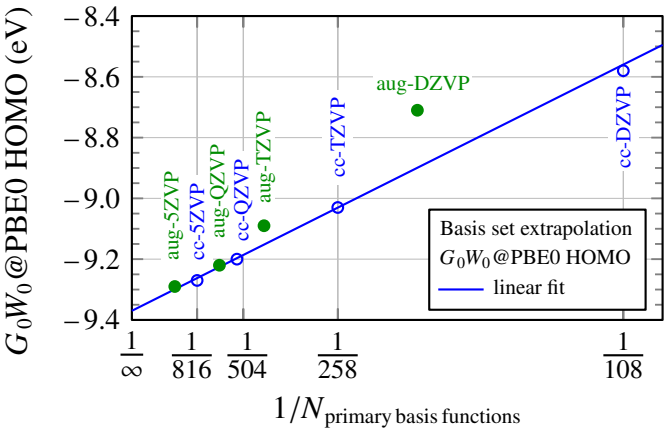

Figure 3.2: Extrapolating the basis set size of the G_0W_0@PBE0 HOMO energy of benzene in the correlation-consistent (cc) basis. As comparison, we show the basis set convergence in the augmented (aug) basis. We observe that an accuracy of 0.1 eV compared to the complete-basis limit is only reached at the level of a cc-5ZVP basis set.

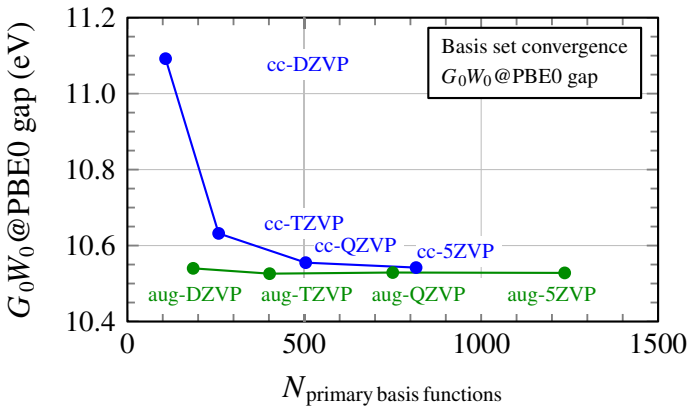

Figure 3.3: G_0W_0@PBE0 HOMO-LUMO gap of benzene for various cc and aug basis sets. We observe that the convergence of the G_0W_0-HOMO-LUMO gap in an augmented Gaussian basis is already reached using an aug-DZVP basis with an accuracy below 0.02 eV compared to the complete basis-set limit.

RI-basis set

Figure 3.4 shows the convergence of the G_0W_0@PBE0-HOMO energy with the size of the RI-basis set for benzene. As primary basis, we use the cc-5ZVP basis. The RI basis sets have been generated specifically for GTH pseudopotentials [75] employing the procedure of Weigend and co-workers [136]. The maximum angular momentum of the RI basis is identical to the RI basis sets of Weigend *et al.* [136] and the size of the RI basis is similar to Ref. [136]. As it can be seen in Fig. 3.4, an RI-QZVP basis already reaches convergence for a cc-5ZVP primary basis when computing the G_0W_0@PBE0-HOMO energy: The difference between the G_0W_0@PBE0-HOMO energy with the RI-QZVP and the RI-5ZVP basis is less than 0.001 eV. Since the overall execution time of our G_0W_0 scheme scales quadratically with the number of RI basis functions for large systems, the computational cost for a cc-5ZVP basis set may be reduced by a factor of two for large systems when using the RI-QZVP basis instead of the RI-5ZVP basis without significant

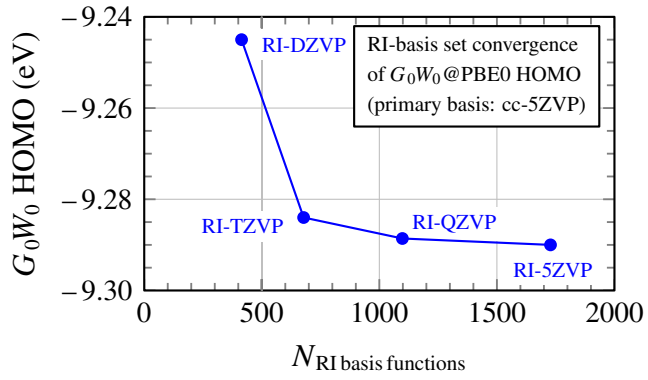

Figure 3.4: G_0W_0@PBE0 HOMO of benzene for the cc-5ZVP basis and various RI-basis sets. The RI-basis sets contain Gaussians of angular momenta up to $l_{\text{RI-DZVP}} = 3$, $l_{\text{RI-TZVP}} = 4$, $l_{\text{RI-QZVP}} = 5$ and $l_{\text{RI-5ZVP}} = 6$, respectively. We observe that an RI-QZVP basis already reaches convergence for a cc-5ZVP primary basis with a precision of 0.001 eV.

loss of accuracy. We conclude that the computational cost can be reduce by employing a smaller RI basis but the angular momentum components have to be chosen carefully in order to properly fit the primary basis. Clever RI basis sets are minimum in size and tuned properly with angular momentum.

Auxiliary density matrix method (ADMM)

In ADMM [138, 139], an approximate auxiliary density matrix is employed to compute the exact Hartree-Fock exchange at the SCF level. For the auxiliary density matrix, a smaller Gaussian basis is used compared to the Gaussian basis in the SCF. When employing the ADMM methodology, the cost and memory for computing the exact exchange in the SCF can be reduced significantly.

The auxiliary density matrix can be derived from several schemes named ADMM1 [138], ADMM2 [138], ADMMQ [139], ADMMP [139] and ADMMS [139]. In ADMM1, the MOs in the auxiliary basis remain orthogonal, while in ADMM2 this is not the case in order to allow a higher flexibility for the auxiliary fitting basis. As a consequence, the ADMM2 auxiliary density matrix is purified to restore the idempotency of density matrices. In ADMMQ, the particle number in the auxiliary density matrix is constrained to the particle number of the full density matrix. In ADMMS and ADMMP, the particle number in the auxiliary basis is also constrained and scaling laws of exchange are respected in two ways which are different for ADMMS and ADMMP.

Here, the influence of ADMM on the G_0W_0 quasiparticle energies is tested when using the ADMM approximation in computing the reference PBE0 wavefunctions. The reason for testing ADMM is that for a high-quality basis as needed for G_0W_0, the computation of the exact exchange at the SCF level can by far dominate in the total execution time.[1]

Figure 3.5 displays the G_0W_0@PBE0-HOMO energy in case ADMM has been employed in the SCF while exact exchange with the full primary basis has been used for the exchange self-energy in Eq. (3.22). We observe that regardless of the ADMM scheme, the G_0W_0@PBE0-HOMO energy of benzene differs by 0.03 eV between exact Fock exchange in the SCF and an ADMM-treated Fock exchange in the SCF. Since the systems considered in this work are not prohibitively large for exact exchange calculations, we treat the Fock exchange exactly [115, 116] throughout this work.

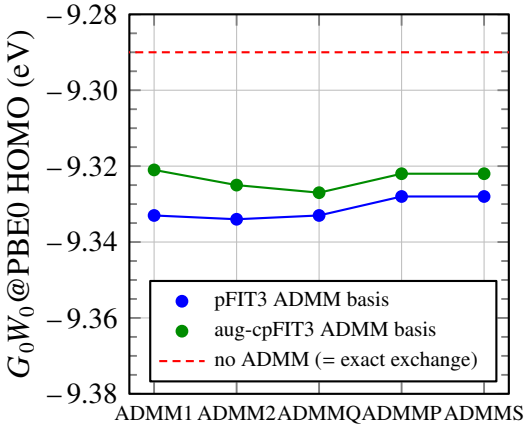

Figure 3.5: G_0W_0@PBE0 HOMO of benzene for an approximative treatment of the exact exchange in the SCF for five auxiliary density matrix methods (ADMM) [138, 139]. The exchange self-energy in Eq. (3.22) is treated exactly without ADMM. Both auxiliary ADMM basis functions contain basis functions up to $l = 3$, where aug-cpFIT3 contains more basis functions than pFIT3. We observe tha regardless of the ADMM scheme, the G_0W_0@PBE0-HOMO energy of benzene differs by 0.03 eV between exact Fock exchange in the SCF and an ADMM-treated Fock exchange in the SCF.

[1] The reason for the high computational cost for computing the exact exchange in the SCF is, that during the SCF procedure, the ERIs are needed in each cycle while at the G_0W_0 level, the computation of the ERIs for the exact-exchange Fock matrix elements has to be performed only once. For a high quality basis, the screening in the computations of the ERIs is not efficient and the available memory can thus not be enough for their complete storage, meaning that part of them have to be recomputed at each SCF cycle making the SCF computationally more demanding than the G_0W_0 quasiparticle energy evaluation.

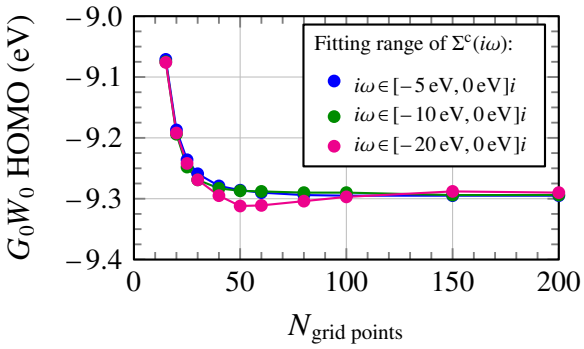

Figure 3.6: G_0W_0@PBE0 HOMO of benzene for different numbers of Clenshaw-Curtis integration grid points of Eq. (4.22) and for three intervals on the imaginary axis for the fitting procedure in Eq. (3.21). For a fitting range of $[-10\,\text{eV}, 0\,\text{eV}]i$ and 50 grid points, we obtain a result being converged with a precision of 0.01 eV.

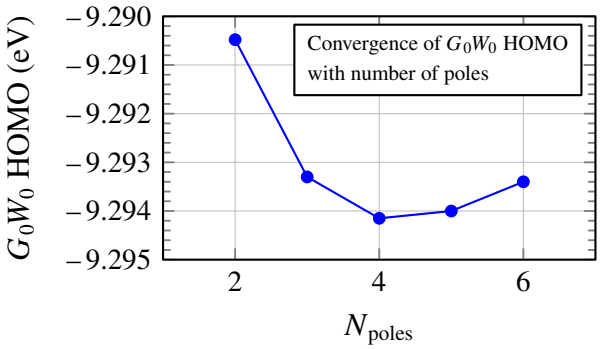

Figure 3.7: G_0W_0@PBE0 HOMO of benzene as function of the number of fitting poles N_{poles} in Eq. (3.21). We observe that two poles are already sufficient for the fitting procedure: The result changes by less than 0.005 eV for three or more poles compared to two poles.

Grid for frequency integration, fitting range and number of poles

The correlation self-energy $\Sigma^c(i\omega)$ on the imaginary-frequency axis, with a fixed value of ω, is obtained by numerical integration of Eq. (4.22). Consistently to the way the RPA correlation energy is computed [75], a Clenshaw-Curtis grid [122, 123] $\{\omega_k\}$ is employed with a fixed scaling parameter [123] $a = 0.2$ Hartree. The same grid $\{\omega_k\}$ is employed for ω' and ω in Eq. (4.22), meaning that the self-energy $\Sigma^c(i\omega)$ is evaluated at the same frequencies ω as those employed for the numerical integration over ω'. Subsequently, $\Sigma^c(i\omega_k)$ is fitted with the two-pole model of Eq. (3.21). According to the target accuracy, an ω-interval is defined and only the ω_k points that are contained in this range are employed for the fitting procedure.

Figure 3.6 displays the convergence of the G_0W_0@PBE0 HOMO energy of benzene with respect to the number of grid points for different fitting intervals of $\Sigma^c(i\omega)$. The drawback of using a large fitting interval is that for an ω_j with large absolute value, $\Sigma^c(i\omega_j)$ is calculated with lower accuracy compared to $\Sigma^c(i\omega_j)$ with smaller absolute value $|\omega_j|$. The reason is that the integrand in Eq. (4.22) is large for $\omega_j = \omega'_j$ but the resolution of the $\{\omega'_k\}$ grid around ω_j with large $|\omega_j|$ is coarse, see e. g. Fig. 3.1. The consequence of this issue is seen in Fig. 3.6 for the large fitting interval $[-20\,\text{eV}, 0\,\text{eV}]i$: The HOMO energy converges more slowly and non-monotonously compared to the smaller fitting intervals. On the other hand, a too small fitting interval may miss the structure of Σ^c on the imaginary-frequency axis. Consequently, we take a medium fitting interval of $[-10\,\text{eV}, 0\,\text{eV}]i$ for all calculations presented in this work. Moreover, we observe in Fig. 3.6 that with 50 grid points and a fitting interval of $[-10\,\text{eV}, 0\,\text{eV}]i$, the HOMO energy is converged with an accuracy of 0.01 eV. To ensure high-quality results, we use 100 grid points for all following calculations.

The fit of the correlation self-energy on the imaginary-frequency axis is performed by using a multi-pole model employing a given number of poles N_{poles}, see Eq. (3.21). Figure 3.7 displays the G_0W_0@PBE0 HOMO energy of benzene for various numbers of poles used. In agreement with previous works [13, 39], we find that two poles for the fitting procedure are already sufficient: the result changes by less than 0.005 eV for three or more poles compared to two poles. As a consequence, we take two poles for all following calculations.

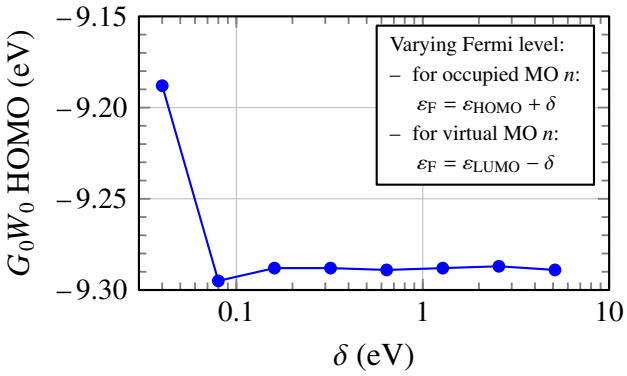

Figure 3.8: G_0W_0@PBE0 HOMO of benzene as function of a varying Fermi level ε_F in the Green's function in Eq. (4.22). We observe in Fig. 3.8 that as long as the Fermi level is located more than 0.1 eV above the HOMO or 0.1 eV below the LUMO energy, we get identical results for the benzene G_0W_0@PBE0 HOMO energy.

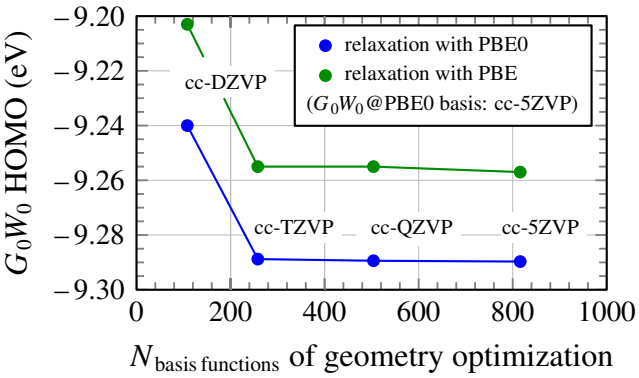

Figure 3.9: G_0W_0@PBE0 HOMO of benzene for various geometries. The geometries have been obtained by a geometry optimization with PBE0 (blue dots) and PBE (green dots). The basis for G_0W_0 is cc-5ZVP. We observe that a relaxation with a cc-TZVP basis is sufficiently close to the complete-basis limit. Moreover, we find that the G_0W_0@PBE0 HOMO level differs by 0.04 eV for the structures obtained with PBE and PBE0.

Fermi level

The Fermi level ε_F is needed in order to compute the Green's function for imaginary frequencies, see Eq. (4.22). As sketched in Fig. 3.1, we set the Fermi level ε_F in Eq. (4.22) for occupied orbitals n as $\varepsilon_F = \varepsilon_{HOMO} + 0.3\,\text{eV}$ and for virtual orbitals n as $\varepsilon_F = \varepsilon_{LUMO} - 0.3\,\text{eV}$. In principle, the Fermi level may be chosen arbitrarily between the HOMO and the LUMO energy of the underlying GKS calculation. Indeed, we observe in Fig. 3.8, that as long as the Fermi level is located more than 0.1 eV above the HOMO energy of the SCF, we get identical results for the benzene G_0W_0@PBE0 HOMO energy. Due to the numerical issues seen for $\delta < 0.1$ eV in Fig. 3.8, G_0W_0 calculations for a system with a GKS gap smaller than 0.2 eV need a careful treatment within our methodology.

Geometry optimization

Prior to a G_0W_0 calculation, it is a common practice to relax the ground state geometry employing the same KS method as used to generate the input orbitals for the G_0W_0 calculation. For hybrid functionals, the computation of the exact HF exchange can be significantly more expensive such that the geometry optimization would be more costly than the subsequent G_0W_0 calculation. Here, we examine the influence of the input geometry on the G_0W_0@PBE0 HOMO energy, see Fig. 3.9. The geometries have been obtained by a structure optimization with the PBE and the PBE0 functional, respectively and various basis sets, while the G_0W_0@PBE0 HOMO is obtained using the cc-5ZVP basis. As shown in Fig. 3.9 (a), the structure relaxation with a cc-TZVP is sufficiently close to the complete-basis limit. Moreover, we find that the G_0W_0@PBE0 HOMO level differs by 0.04 eV between structures relaxed at the PBE and PBE0 level (or other hybrids). We conclude that using a non-hybrid functional for the geometry optimization may introduce a non-negligible error in G_0W_0@PBE0 quasiparticle energies. To reduce the cost to generate the initial geometry, a small primary basis at the triple-zeta level can be used to obtain converged quasiparticle energies.

Execution time, system size scaling and parallel speedup

For an exemplary benchmark of the computational cost, we show the execution time for computing 20 G_0W_0 quasiparticle energies (HOMO–9, HOMO–8, ..., LUMO+9) for various water clusters in Fig. 3.10 (a) (without the time spent for the GKS calculation) employing $N_\omega = 60$ grid points for the frequency integration in a cc-TZVP basis.

According to Eq. (4.26), computing $\Pi_{PQ}(i\omega)$ for all grid points ω_k requires $N_{\text{aux}}^2 N_{\text{occ}} N_{\text{virt}} N_\omega$ operations, where N_{aux} is the number of auxiliary RI-basis functions, N_{occ} (N_{virt}) the number of occupied (virtual) molecular orbitals and N_ω the number of Clenshaw-Curtis grid points. Assuming N_ω to be independent on the system size N, this step scales as $\mathcal{O}(N^4)$. The measured exponent is 3.93, see Fig. 3.10 (a) and therefore matching the expected value. Note that once $\Pi_{PQ}(i\omega)$ is made available for all ω_k, the computation of $\Sigma_n^c(i\omega)$ in Eq. (4.22) requires only $\mathcal{O}(N^3)$ operations, more specifically $N_{\text{aux}}^2 N_{G_0W_0}(N_{\text{occ}}+N_{\text{virt}})N_\omega$, where $N_{G_0W_0}$ is the number of computed G_0W_0 quasiparticle energies. We observe an exponent of 3.34 in Fig. 3.10 (a) which is slightly exceeding the expected exponent of 3. According to this analysis, we expect a numerical effort for the overall computation of the G_0W_0 quasiparticle energies which asymptotically scales as $\mathcal{O}(N^4)$. This is what we observe as total execution time for our G_0W_0 algorithm, see Fig. 3.10 (a): The computational effort for the integral evaluation part has an asymptotic scaling that grows quadratically with system size: For each auxiliary RI density, only matrix elements between overlapping Gaussian functions need to be calculated. For this reason, the effort for the integral evaluation strongly depends on the structure of the system, since this affects the overlap between the atom-centered Gaussian basis

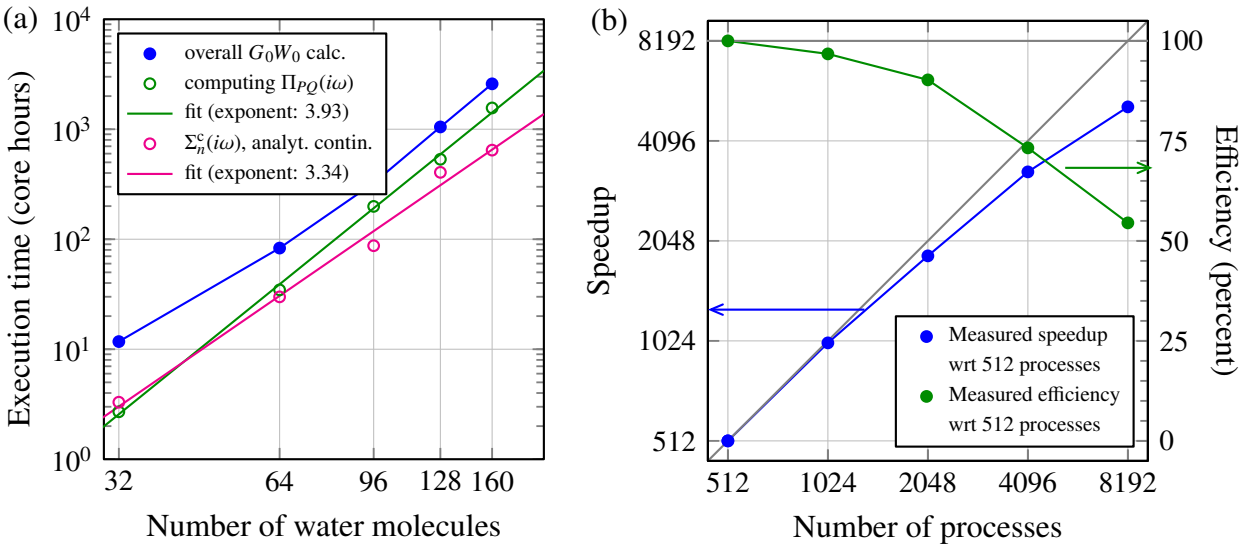

Figure 3.10: (a) Execution time for the calculation of 20 G_0W_0 quasiparticle levels of water clusters containing up to 480 atoms in a cc-TZVP basis with 60 grid points for the numerical integration of Eq. (4.22) on a Cray XC30 machine. The blue dots belong to the time spent for the whole G_0W_0 calculation (without the time spent for the SCF), the green circles belong to the time for computing the matrix $\Pi_{PQ}(i\omega)$ [Eq. (4.26)] and the magenta circles belong to the computation time of the self-energy [Eq. (4.22)] and the analytic continuation. The magenta and green lines represent a linear two-parameter fit of the form $y = ax^b$ with an exponent b as reported in the legend. (b) Measured speedup (blue dots, left ordinate) and efficiency (green dots, right ordinate) with respect to 512 processes for the calculation of 20 G_0W_0 quasiparticle energies of a 64 water-molecule cluster. We used a cc-TZVP basis and 60 grid points for the numerical integration of Eq. (4.22). The gray lines represent the ideal speedup and the ideal efficiency, respectively.

functions and thus is directly related to the effectiveness of the screening on the matrix elements. For small and compact systems, the integral evaluation is in general dominating the overall time of a G_0W_0 calculation [75]. On the other hand, in the evaluation of $\Pi_{PQ}(i\omega)$, that scales $O(N^4)$ with system size, no screening is considered and thus this part is independent on the actual structure of the system. This part is by far the most time consuming in a large G_0W_0 calculation [76].

We assess the parallel speedup of the implementation with a cluster containing 64 water molecules (256 occupied orbitals, 3392 virtual orbitals and 8704 auxiliary basis functions), see Fig. 3.10 (b). The algorithm shows a good parallel scalability with an efficiency around 70 % for 4096 processes compared to 512 processes. The total execution time of the G_0W_0 calculation with 512 processes is 606 seconds, while the G_0W_0 calculation is completed in 70 seconds employing 8192 processes.

Comparison to experiments and other G_0W_0 implementations

In this section, we compare G_0W_0-HOMO energies of small molecules to experimental values and other GW implementations, see Table 3.1. Additionally, we apply G_0W_0 to study the influence of different ligands on the gap of CdSe nanoclusters.

HOMO levels of molecules

As generalized Kohn-Sham (GKS) starting points for the G_0W_0 calculation of molecules, we consider PBE [96], PBE0 [85], which contains 25 % exact exchange, and tuned CAM-B3LYP [86, 141], a range-separeted hybrid functional as implemented in the exchange-correlation library

Table 3.1: G_0W_0 HOMO energy $\varepsilon_{\text{HOMO}}^{G_0W_0}$ of small molecules containing atoms from the first period. We present results for the PBE [96], PBE0 [85] and the tuned CAM-B3LYP [81, 86, 141] (tCB) starting point. The experimental vertical ionization potentials (VIPs) are taken from Ref. [87] besides the one of methane [142]. The mean absolute deviation (MAD) measures the deviation with respect to the experimental VIPs and the G_0W_0 HOMO energies reported by Ren *et al.* [13], Bruneval and Marques [31], Govoni and Galli [14], Turbomole without RI and full-frequency (ff) BerkeleyGW from the $GW100$ benchmark by van Setten *et al.* [71] The unit of all numbers is eV.

Molecule	G_0W_0@PBE		G_0W_0@PBE0		G_0W_0@tCB		Exp. VIP
	cc-QZVP	cc-5ZVP	cc-QZVP	cc-5ZVP	cc-TZVP	cc-QZVP	
C_6H_6	−9.00	−9.07	−9.21	−9.29	−9.33	−9.51	−9.24
CH_4	−14.00	−14.05	−14.28	−14.33	−14.47	−14.59	−14.40
C_2H_2	−11.01	−11.11	−11.25	−11.33	−11.35	−11.52	−11.49
C_2H_5OH	−10.26	−10.35	−10.63	−10.73	−10.77	−10.99	−10.64
CO_2	−13.20	−13.33	−13.58	−13.72	−13.64	−13.85	−13.78
N_2	−14.87	−15.03	−15.37	−15.52	−15.44	−15.66	−15.58
NH_3	−10.29	−10.42	−10.64	−10.75	−10.80	−11.00	−10.82
H_2O	−11.97	−12.13	−12.33	−12.46	−12.46	−12.72	−12.62
O_2	−11.65	−11.83	−12.24	−12.40	−12.43	−12.70	−12.30
MAD to exp. VIPs	0.51	0.39	0.15	0.09	0.12	0.21	
MAD to FHI-aims [13] (tier+a5Z-d basis)	0.02	0.10	0.05	0.07	–	–	
MAD to molgw [31] (QZVP basis)	0.06	0.04	0.04	0.04	0.18	0.08	
MAD to WEST [14] (PW basis)	0.09	0.11	0.11	0.03	–	–	
MAD to Turbomole [71] (QZVP basis)	0.03	0.11	–	–	–	–	
MAD to ff BerkeleyGW [71] (PW basis)	0.14	0.26	–	–	–	–	

LIBXC, version 2.2.2 [81] with 100 % exact long-range exchange. It has been reported in the literature that G_0W_0 HOMO energies are in excellent agreement with experimental vertical ionization potentials (VIPs) and CCSD(T) values if the GKS calculation was performed with the tuned CAM-B3LYP functional [31,46,143] or the PBE0 hybrid functional [13,14,31,40,47,82–85,96] while local functionals as PBE or pure Hartree-Fock perform worse [13,31].

For PBE, PBE0 and tuned CAM-B3LYP, the G_0W_0 HOMO energies of small molecules are listed in Table 3.1. The results indicate that for the G_0W_0@PBE0 HOMO energies, the large basis cc-5ZVP provides the best agreement with experimental values: The observed mean absolute error is below 0.1 eV compared to the experimental vertical ionization potential (VIP). In contrast, the best agreement with experimental VIPs for G_0W_0@tuned CAM-B3LYP HOMO energies are obtained within the cc-TZVP basis. The larger cc-QZVP basis deteriorates the mean absolute error compared to experimental VIPs. The accuracy of inner orbitals (higher IPs) in G_0W_0 is of similar accuracy as reported here for the HOMO [82].

Overall, our results agree well with the results reported by Ren *et al.* [13], Bruneval and Marques [31], Govoni and Galli [14] and from *GW*100 [71,144], see Table 3.1. Possible differences are due to the use of pseudopotentials and the differing basis.

G_0W_0 HOMO-LUMO gaps of $Cd_{33}Se_{33}$ nanoclusters in the presence of ligands

In this section, we apply G_0W_0@LDA and G_0W_0@PBE to compute the HOMO-LUMO gap of the $Cd_{33}Se_{33}$ nanocluster with different surrounding ligands, see Fig. 3.11 for the molecular geometry of the bare $Cd_{33}Se_{33}$ cluster. At best of our knowledge, no *GW* calculations have been reported in the literature on the $Cd_{33}Se_{33}$ nanocluster.

We are motivated by the fact that CdSe has been one of the most studied II-VI quantum dots due to the ease of synthesis and, according to the dimension of the QDs, its optical gap can cover the visible spectrum. [146,147] We chose the $Cd_{33}Se_{33}$ quantum dot since it is one of the "magic-size" clusters that have been characterized by high stability and large optical gaps. For quantum dots, surface ligands are fundamental for enhancing the solubility and for stabilizing the core structure. The ligands can strongly affect the electronic properties of the quantum dots, in particular the optical gap. [148–153] We investigate the influence of these surface ligands on the HOMO-LUMO gap of $Cd_{33}Se_{33}$ quantum dots on the level of G_0W_0@LDA and G_0W_0@PBE. As model ligands, we employ formic and acetic acid, ammonia and methyl amine. [145]

As molecular geometries of the bare $Cd_{33}Se_{33}$ cluster and $Cd_{33}Se_{33}$ with ligands, we employ the structures from Ref. [145]: The bare cluster has been obtained by carving out an almost spherical portion of the wurtzite lattice with bulk CdSe bond lengths and subsequent relaxation on the level of LDA [132]. Similar constructions of CdSe clusters from the bulk semiconductor have been used in previous theoretical studies. [148,149,154,155] The cages in presence of the ligands have been fully relaxed on the LDA level. We employ GTH [130,131] pseudopotentials. In the SCF, we optimize twelve electrons for Cd and six electrons for Se.

We employ G_0W_0@LDA and G_0W_0@PBE to compute the HOMO-LUMO gap of the $Cd_{33}Se_{33}$

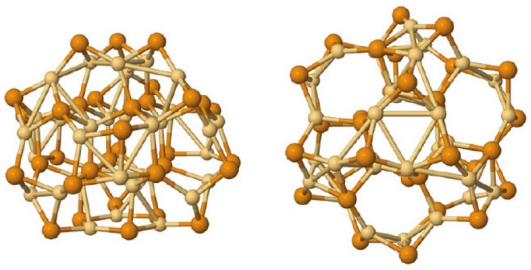

Figure 3.11: Molecular structure of the bare $Cd_{33}Se_{33}$ nanocluster: side view (left) and top view (right). [145] The Cd is light yellow and the Se is bronze in the ball-and-stick models.

Table 3.2: LDA, G_0W_0@LDA, PBE and G_0W_0@PBE HOMO-LUMO gaps in eV of $Cd_{33}Se_{33}$ nanoclusters with surrounding ligands in an aug-DZVP basis set. For the $Cd_{33}Se_{33}$ nanocluster, 594 non-core electrons (12 electrons per Cd atom, 6 electrons per Se atom), 2574 primary basis functions and 8316 RI basis functions have been employed. This calculation took 15 minutes on 1536 Cray XC40 cores.

System	LDA	G_0W_0@LDA	PBE	G_0W_0@PBE	Exp. optical gap
bare $Cd_{33}Se_{33}$	1.51	3.64	1.60	3.62	3.0 [156]
$Cd_{33}Se_{33}$ + 9 NH_3	1.57	3.59	1.70	3.56	
$Cd_{33}Se_{33}$ + 12 NH_3	1.61	3.60	1.73	3.60	
$Cd_{33}Se_{33}$ + 21 NH_3	1.75	3.69	1.87	3.69	
$Cd_{33}Se_{33}$ + 9 H_3CNH_2	1.56	3.56	1.68	3.56	
$Cd_{33}Se_{33}$ + 9 HCOOH	2.03	4.10	2.19	4.14	
$Cd_{33}Se_{33}$ + 9 HCOOH + 12 NH_3	2.03	4.06	2.20	4.10	
$Cd_{33}Se_{33}$ + 9 H_3CCOOH	2.00	4.05	2.16	4.09	

nanocluster. We follow the authors of Refs. [21] and [14] who employed G_0W_0@LDA and G_0W_0@PBE for computing the HOMO-LUMO gap of silicon nanoclusters. We employ an aug-DZVP basis set and we expect G_0W_0 HOMO-LUMO gaps which are close to the complete-basis-set limit [11, 35, 40, 45, 46].

We have computed the HOMO-LUMO gap of the $Cd_{33}Se_{33}$ nanocluster in the bare form and with ligands on different levels of theory, see results in Table 3.2. For the bare cluster, we find an LDA and a PBE HOMO-LUMO gap of 1.51 eV and 1.60 eV, respectively. Both values strongly underestimate experiments with a measured optical gap of 3.0 eV of $Cd_{33}Se_{33}$ [156] probably due to the spurious self-interaction of the HOMO. In contrast, after one-shot G_0W_0@LDA and G_0W_0@PBE, the HOMO-LUMO gap opens up to 3.64 eV and 3.62 eV, respectively. The G_0W_0 HOMO-LUMO gaps are compatible with the experimental optical gap in the sense that the experimental optical gap ist smaller than the G_0W_0 HOMO-LUMO gap due to the exciton binding energy. For a computation of the optical gap, the Bethe-Salpeter equation on top of G_0W_0 would be necessary.

For the $Cd_{33}Se_{33}$ cluster with ligands, electron-donating ligands as amines hardly affect the HOMO-LUMO gap of the $Cd_{33}Se_{33}$ nanocluster. This effect is seen on both levels of theory, LDA/PBE and G_0W_0. In contrast, the HOMO-LUMO gap of $Cd_{33}Se_{33}$ is strongly affected by electron-attracting ligands as formic acid. Again, this effect is seen on both levels of theory, LDA/PBE and G_0W_0. The influence of the ligands on the HOMO-LUMO gap of $Cd_{33}Se_{33}$ was already found in Ref. [145] by LDA and PBE calculations and we validated this finding by G_0W_0.

3.4 Application of eigenvalue-selfconsistent *GW* to linear acenes

In this section, we apply eigenvalue-selfconsistent *GW* (ev*GW*) to compute the HOMO-LUMO gap of linear acenes, see Fig. 3.12 for the molecular geometry. This application is motivated by a recent DFT-based study by Korytár *et al.* [88] indicating that the HOMO-LUMO gaps of acenes may not decay monotonously with increasing number of benzene rings, but can oscillate. The key ingredient to obtain a reasonable ev*GW* HOMO-LUMO gap is to employ a proper electronic ground state. Concerning the ground state of acenes, contradictory findings have been reported, see Sec. 3.4. The main point of debate is whether the ground state of acenes is a radical or not. For our ev*GW* HOMO-LUMO-gap calculations, we employ closed-shell and open-shell broken-

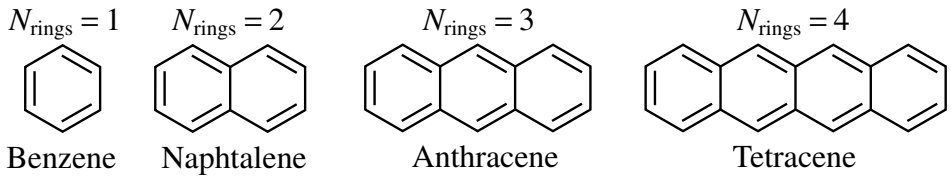

Figure 3.12: Molecular structure of the first four acenes.

symmetry DFT ground states as described in the computational details in Sec. 3.4. Then, we compare ev*GW* HOMO-LUMO gaps of anthracene, tetracene and pentacene to experimental values (Sec. 3.4). In Sec. 3.4, we predict the HOMO-LUMO gap of long acenes employing ev*GW* based on closed-shell and open-shell broken-symmetry DFT ground states. We find distinct differences between the closed- and the open-shell ev*GW* HOMO-LUMO gaps for long acenes. In future experiments, a comparison of measured HOMO-LUMO gaps and our calculated ev*GW* values may be helpful to identify whether the ground state of the acene exhibits a closed-shell or polyradical configuration.

Electronic ground state of acenes

In DFT studies employing hybrid functionals, singlet broken-symmetry, spin-polarized ground states have been reported for acenes with $N_{\text{rings}} \geq 6$. [99] This finding can be rationalized by Clar's theory. For details, we refer to Ref. [157]. Since a polyradical singlet ground state is not described by a single Slater determinant, it is difficult to interpret whether DFT or Hartree-Fock based studies predict the correct spin configuration of the ground state.

Two findings from density matrix renormalization group (DMRG) calculations, which incorporate multiple Slater determinants, have been reported: In the recent study by Korytár *et al.* [88], the DMRG with on-site and nearest-neighbor interactions indicates that the ground state of acenes does not exhibit a (simple) broken-symmetry phase. Hachmann *et al.* [98] concluded in their DMRG study based on the full Coulomb interaction that longer acenes exhibit singlet polyradical character in their ground state. The latter finding was supported by multiconfiguration SCF calculations by Plasser *et al.* [97] Experimental evidence for the ground state of longer acenes is missing since the synthesis of gas-phase acenes with more than six rings (hexacene) remains a challenge [158, 159].

Computational details

We perform closed-shell and open-shell DFT calculations on the acenes as basis for geometry optimizations and the ev*GW* calculations. For open-shell calculations, we initialize the wavefunctions with a singlet broken-symmetry guess and keep zero total spin during the SCF cycle. We obtain the oligoacene structures by a geometry optimization employing the PBE0 [85] functional in a cc-TZVP basis.[2]

Eigenvalue-selfconsistent *GW* (ev*GW*) calculations are performed as suggest by X. Blase *et al.* [11] In this methodology, the eigenvalues $\varepsilon_n^{G_0W_0}$ from Eq. (3.22) are employed to recompute the correlation self-energy and finally every eigenvalue. This procedure is repeated up to convergence and has been shown to give HOMO-LUMO gaps which are in good agreement with experimental values, especially for organic semiconductors with extended π-systems. [34] As starting points for the ev*GW* calculations, we employ wavefunctions and eigenvalues from DFT calculations

[2]Geometry optimizations are performed with a closed-shell restriction for closed-shell ev*GW* HOMO-LUMO gap calculations and with a singlet broken symmetry for open-shell ev*GW* HOMO-LUMO gap calculations.

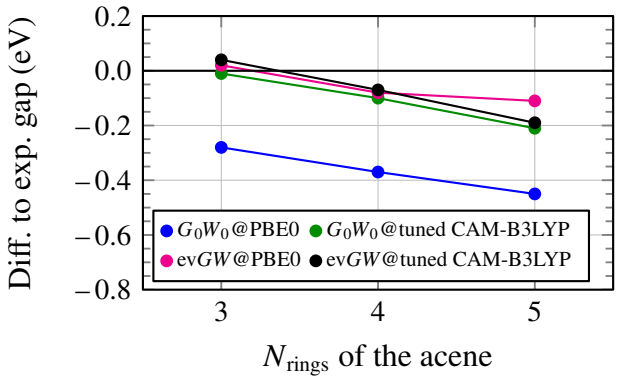

Figure 3.13: Deviation of the open-shell (broken-symmetry) G_0W_0 and eigenvalue-self-consistent *GW* [11] (ev*GW*) HOMO-LUMO gap of acenes (aug-TZVP basis) from experimental HOMO-LUMO gaps.

with the PBE0 and the tuned CAM-B3LYP functional. It has been pointed out by Bruneval and Marques [31] that both functionals are two of the most reliable starting points for *GW* calculations for molecules.

For the ev*GW* HOMO-LUMO gap calculations, augmented basis sets are used. In augmented basis sets as the aug-DZVP and aug-TZVP, ev*GW* HOMO-LUMO gaps are close to the complete-basis-set limit, see Fig. 3.3 for benzene and the literature [11, 35, 40, 45, 46]. All other parameters are chosen as specified in Sec. 3.3 to ensure excellent convergence of the ev*GW* results.

G_0W_0 and ev*GW* HOMO-LUMO gaps of acenes compared to experiments

In Fig. 3.13, we compare open-shell G_0W_0 and ev*GW* HOMO-LUMO gaps of anthracene, tetracene and pentacene to experimental data [87]. It is important to note that the experimental assignment of the vertical IP in acenes is controversial and displays large error bars, see Ref. [160] and references therein. As an example, for the molecular crystal of tetracene, the error of the HOMO-LUMO gap is estimated to be 0.5 eV. We find that the G_0W_0@tuned CAM-B3LYP HOMO-LUMO gaps are close to experiment with a maximum deviation of 0.21 eV, while the G_0W_0@PBE0 HOMO-LUMO gaps exhibit an average error of 0.4 eV compared to experiments. After applying the self-consistency scheme on the eigenvalues as suggested by Blase *et al.* [11, 34, 45, 161] (ev*GW*), we find that HOMO-LUMO gaps of both starting points are on average in agreement by 0.03 eV to each other which has already been reported by previous authors [11, 160, 162]. The mean absolute deviation of the ev*GW* HOMO-LUMO gaps to the experimental HOMO-LUMO gaps remains below 0.1 eV for anthracene, tetracene and pentacene.

The difference of our values to previously reported ev*GW* calculations on acenes in Refs. [11] and [143] can be attributed to their use of LDA wavefunctions [11] and PBE wavefunctions [143] as DFT input of ev*GW*.

ev*GW* HOMO-LUMO gaps of long acenes

We present HOMO-LUMO gaps of linear acenes computed with ev*GW* for the PBE0 and the tuned CAM-B3LYP starting point, see Fig. 3.14. First, we observe, that for all acenes, the ev*GW* HOMO-LUMO gaps based on PBE0 and tuned CAM-B3LYP starting points deviate by less than 0.10 eV (besides 10-acene and 11-acene in the closed-shell case). Second, we observe that the gaps of anthracene and tetracene ($N_{\text{rings}} = 3, 4$) are identical for closed-shell and open-shell calculations. The deviation between the closed-shell and open-shell ev*GW* HOMO-LUMO gap of pentacene is below 0.1 eV. This finding can be rationalized by Clar's theory [157]: For small acenes, Clar's theory predicts a closed shell configuration, while for longer acenes, an open-shell configuration is expected to be favoured. In agreement with this expectation, our (singlet) open-shell calculations

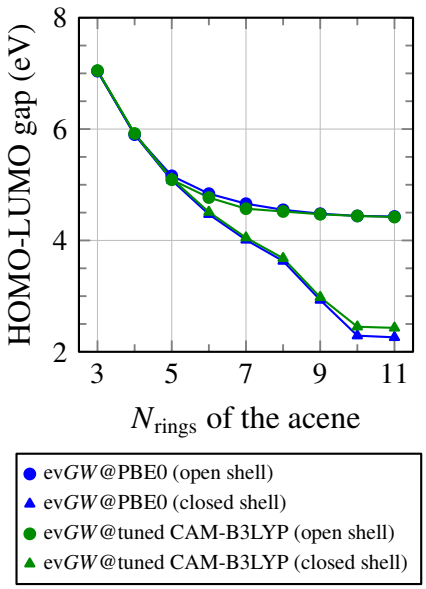

Figure 3.14: ev*GW* HOMO-LUMO gap of acenes within an aug-DZVP basis for the PBE0 (blue) and the tuned CAM-B3LYP starting point (green) with broken-symmetry open-shell (circles) and closed-shell configuration (triangulars). We find that the ev*GW* gaps are only weakly dependent on the starting DFT functional, but strongly dependent on restricting the DFT calculation to closed shell or not: The deviation of the ev*GW* HOMO-LUMO gaps between open-shell and closed-shell can be as large as 2.0 eV (for 10-acene and 11-acene). The distinct jump of the ev*GW* closed-shell gaps between 8-acene and 10-acene is in agreement with the DFT-based study by Korytár *et al.* [88] The reason is that close to 9-acene, the symmetry of the HOMO and LUMO interchanges due to a level crossing in the bandstructure of polyacene [89] as elaborated in Ref. [88].

on anthracene to pentacene converge to a closed-shell-like ground state. As a consequence, the ev*GW* HOMO-LUMO gaps for anthracene to pentacene are (nearly) identical for the closed-shell and the open-shell calculation.

For longer acenes, the difference between the closed-shell and the open-shell ev*GW* gaps is strongly increasing with a maximum of 2.0 eV for 10- and 11-acene: While the open-shell ev*GW* gaps are quickly saturating between 4.4 and 4.6 eV for 7-acene to 11-acene, the closed-shell ev*GW* gaps are rapidly decreasing from 4.0 eV (7-acene) to 2.3 eV or 2.4 eV (11-acene, ev*GW*@PBE0 and ev*GW*@tuned CAM-B3LYP). We conclude that a measurement of the HOMO-LUMO gap of longer acenes ($N_{\text{rings}} \geq 6$) may be able to identify whether the ground state of the acene exhibits a closed-shell or polyradical configuration.

3.5 Conclusions

We have presented a G_0W_0 and eigenvalue-selfconsistent *GW* (ev*GW*) implementation within the Gaussian and plane waves scheme. Technically, we calculate the correlation self-energy for imaginary frequencies employing a resolution-of-the-identity approach based on the Coulomb metric. The correlation self-energy for real frequencies is evaluated by analytic continuation. Our implementation is highly efficient and displays good parallel scalability enabling large-scale G_0W_0 and ev*GW* calculations for systems containing hundreds of atoms.

We benchmarked the implementation for molecules and clusters. For molecules, we found an average error of 0.1 eV between the G_0W_0@PBE0-HOMO energy in a 5ZVP basis and the vertical ionization potential which is in agreement with previously published G_0W_0 data.

We applied ev*GW* to compute the HOMO-LUMO gaps of closed-shell and open-shell broken-symmetry linear acenes as function of the oligoacene length up to 11-acene. We find that the closed-shell and broken-symmetry open-shell ev*GW* HOMO-LUMO gaps of acenes differ by up to 2.0 eV (for 11-acene). In future experiments, a comparison of measured HOMO-LUMO gaps and our calculated ev*GW* values may be helpful to determine whether the electronic ground state exhibits a closed-shell or polyradical configuration.

Chapter 4

Periodic *GW* calculations in the Gaussian and plane waves scheme

The following chapter is a reprint of Ref. [163]. We present a correction scheme for periodic Γ-point-only *GW* calculations in a Gaussian basis. For four benchmark systems, the dependence of the corrected *GW* quasiparticle levels on the cell size is reduced by a factor of three to ten compared to *GW* calculations without correction. The correction scheme comes along with negligible computational cost and enables *GW* calculations for supercells containing hundreds of atoms with Gaussian basis functions.

4.1 Introduction

The accurate prediction of photoelectron spectroscopy is still a major computational challenge in many fields of physics, chemistry, and materials science. [68] For medium and large systems, the most used method is Kohn-Sham (KS) density functional theory. [5] As it is well-known, using KS-DFT eigenvalues for computational spectroscopy has a serious fundamental and practical limitation: Depending on the parametrization of the exchange-correlation functional, the KS-DFT eigenvalues can shift substantially.

The *GW* approximation [9] promises better accuracy for the calculation of quasiparticle energy levels. Besides the search for more accurate *GW* flavours [33, 164–166], the main challenges of *GW* is related to the high computational cost and numerical issues. Therefore, it is not surprising that it took more than twenty years between proposing the *GW* method by Hedin [9] and the first application to real materials by Hybertsen and Louie [10].

Significant progress has been made in reducing the computational cost of *GW* in recent years: Plane-wave *GW* implementations commonly suffer from requiring many virtual states and the inversion of large dielectric matrices. Here, the comination of without-virtual-states techniques [14, 70, 167] with a low-rank approximation of the dielectric matrix [14, 168–171] can improve the computational efficiency enabling large-scale applications [172–174]. Another approach is to reformulate *GW* in a Gaussian basis which can significantly reduce the dimensionality of the involved matrices [11–13, 20, 30, 37, 42, 161, 175–177]. *GW* in a Gaussian basis can be applied to molecules without difficulty [31, 34, 43, 47, 48, 71, 178–182] in contrast to plane-waves implementations where several technical issues have to be addressed [14, 52, 183]. Large-scale *GW* calculations also have been reported using stochastic orbitals [21, 23].

Another issue of periodic *GW* is the necessity for a correction due to the spurious self-interaction between periodic images of quasiparticle wavefunctions. This self-interaction results in a slow $1/L$ convergence of the *GW* quasiparticle levels with the cell length L. In case of Brillouin zone sam-

pling, the $1/L$ convergence translates to a $N_{\mathbf{k}}^{-1/3}$ convergence with the number of k-points. [184] A similar slow convergence as in *GW* has been found for coupled cluster [185,186] and Hartree-Fock exchange in the condensed phase. For the latter, various corrections exist that aim to accelerate the Brillouin zone convergence, including auxiliary function techniques [187] and real-space truncation of the Coulomb interaction [116, 188, 189].

For plane-waves implementations of *GW*, several correction schemes have been proposed to correct for this slow convergence: Analytic integration of the divergence at the Γ-point [10,28,59] which is suitable in case of dense k-point sampling, the Γ-offset method [63,190,191], or Brillouin zone integration using analytical limits at the Γ-point [14, 52, 54, 184, 192]. In the pioneering implementation of periodic *GW* with Gaussians by Rohlfing *et al.* [176, 177], which is so far the only implementation of periodic *GW* in a Gaussian basis to the best of our knowledge, dense k-point sampling is used while the periodic correction has been computed in a plane-waves basis.

In this work, we propose a correction scheme for periodic Γ-point-only *GW* calculations in a Gaussian basis. In Sec. 4.2, we derive our correction scheme in detail. We show benchmark calculations on four materials in Sec. 4.3.

4.2 Derivation of the correction to the periodic *GW* self-energy in a Gaussian basis

In this section, we derive a correction for periodic *GW* calculations that accelerates the slow $1/L$ convergence of *GW* quasiparticle energies with the cell length L. In Sec. 4.2, we start with a brief review of periodic *GW* calculations in a plane-waves basis. Then, the derivation is tailored to the use of Gaussian basis functions and the resolution of the identity with the overlap metric (Sec. 4.2). To apply the correction schemes from plane-waves *GW*, we express the screened Coulomb interaction, the dielectric matrix and the polarizability as square matrices in the resolution-of-the-identity (RI) basis, which corresponds to a plane-waves basis in plane-waves *GW* (Sec. 4.2). For the correction scheme, we add the $\mathbf{G} = 0$ function to the RI basis, see Sec. 4.2. The k-dependence of the polarizability, the dielectric function and the screened Coulomb interaction is needed for the correction and given in Sec. 4.2. Using the k-dependence of the screened Coulomb interaction and Brillouin zone sampling, we integrate the singularity in the self-energy, see Sec. 4.2. Finally, we give the algorithm for periodic *GW* calculations in a Gaussian basis in Sec. 4.2.

Periodic *GW* calculations in a plane-waves basis

In this section, we summarize periodic *GW* calculations in a plane-waves basis with a focus on the divergence of the screened Coulomb interaction at the Γ-point. The equations are taken from Refs. [28], [54] and [193].

The equation for computing the G_0W_0 bandstructure $\varepsilon_{n\mathbf{k}}^{G_0W_0}$ reads [28, 54]

$$\varepsilon_{n\mathbf{k}}^{G_0W_0} = \varepsilon_{n\mathbf{k}}^{\mathrm{DFT}} + Z_{n\mathbf{k}} \mathrm{Re}\, \langle n\mathbf{k}|\Sigma^{\mathrm{c}}(\varepsilon_{n\mathbf{k}}^{\mathrm{DFT}}) + \Sigma^{\mathrm{x}} - V_{\mathrm{DFT}}^{\mathrm{xc}}|n\mathbf{k}\rangle \tag{4.1}$$

where we focus on the correlation part $\Sigma_{n\mathbf{k}}^{\mathrm{c}}$ of the self-energy in this work. On the imaginary frequency axis and using a plane-waves basis, it can be computed as

$$\Sigma_{n\mathbf{k}}^{\mathrm{c}}(i\omega) = -\frac{1}{2\pi}\frac{1}{\Omega}\sum_{\mathbf{q}}^{1.\,\mathrm{BZ}}\sum_{m}^{\mathrm{all}}\int_{-\infty}^{\infty} d\omega' \frac{1}{i(\omega-\omega') + \varepsilon_{\mathrm{F}} - \varepsilon_{m\mathbf{k}-\mathbf{q}}} \sum_{\mathbf{G}\mathbf{G}'} A_{\mathbf{G},\mathbf{q}}^{n\mathbf{k},m\mathbf{k}-\mathbf{q}} W_{\mathbf{G}\mathbf{G}'}^{\mathrm{c}}(i\omega', \mathbf{q}) \left(A_{\mathbf{G}',\mathbf{q}}^{n\mathbf{k},m\mathbf{k}-\mathbf{q}}\right)^* \tag{4.2}$$

where $\Omega = \Omega_{\text{cell}}/N_{\mathbf{k}}$ and $A^{n\mathbf{k},m\mathbf{k}-\mathbf{q}}_{\mathbf{G},\mathbf{q}}$ is given by

$$A^{n\mathbf{k},m\mathbf{k}-\mathbf{q}}_{\mathbf{G},\mathbf{q}} = \langle n\mathbf{k}|e^{i(\mathbf{q}+\mathbf{G})\mathbf{r}}|m\mathbf{k}-\mathbf{q}\rangle \ . \tag{4.3}$$

The correlation part of the screened Coulomb interaction reads

$$W^{\text{c}}_{\mathbf{G}\mathbf{G}'}(i\omega,\mathbf{q}) = \frac{\sqrt{4\pi}}{|\mathbf{q}+\mathbf{G}|}\left(\epsilon^{-1}_{\mathbf{G}\mathbf{G}'}(i\omega,\mathbf{q}) - \delta_{\mathbf{G}\mathbf{G}'}\right)\frac{\sqrt{4\pi}}{|\mathbf{q}+\mathbf{G}'|}\,, \tag{4.4}$$

and the symmetric dielectric function is given by

$$\epsilon_{\mathbf{G}\mathbf{G}'}(i\omega,\mathbf{q}) = \delta_{\mathbf{G}\mathbf{G}'} - \frac{\sqrt{4\pi}}{|\mathbf{q}+\mathbf{G}|}\chi^0_{\mathbf{G}\mathbf{G}'}(i\omega,\mathbf{q})\frac{\sqrt{4\pi}}{|\mathbf{q}+\mathbf{G}'|}\,, \tag{4.5}$$

where $\chi^0_{\mathbf{G}\mathbf{G}'}(i\omega,\mathbf{q})$ is the independent particle polarizability,

$$\chi^0_{\mathbf{G}\mathbf{G}'}(i\omega,\mathbf{q}) = \frac{1}{\Omega}\sum_{\mathbf{k}ia}^{\text{occ,virt}} A^{i\mathbf{k},a\mathbf{k}-\mathbf{q}}_{\mathbf{G},\mathbf{q}}\frac{2(\varepsilon_{i\mathbf{k}}-\varepsilon_{a\mathbf{k}-\mathbf{q}})}{\omega^2+(\varepsilon_{i\mathbf{k}}-\varepsilon_{a\mathbf{k}-\mathbf{q}})^2}\left(A^{i\mathbf{k},a\mathbf{k}-\mathbf{q}}_{\mathbf{G}',\mathbf{q}}\right)^* \ . \tag{4.6}$$

Now, we focus on the divergent terms for $\mathbf{G}=\mathbf{0}$ at the Γ-point of the Brillouin zone, $\mathbf{k}\to 0$. We start by analyzing the head of the polarizability, $\chi^0_{\mathbf{0}\mathbf{0}}(\mathbf{q},i\omega)$. Note that $A^{i\mathbf{k},a\mathbf{k}-\mathbf{q}}_{\mathbf{0},\mathbf{q}} \xrightarrow{\mathbf{q}\to 0} i\mathbf{q}\,\langle i\mathbf{k}|\mathbf{r}|a\mathbf{k}\rangle$ for $\mathbf{q}\to 0$ which can be seen by Taylor expansion of $e^{i\mathbf{q}\mathbf{r}}$ for small $\mathbf{q}$ and the orthogonality of molecular orbitals, $\langle i\mathbf{k}|a\mathbf{k}\rangle = 0$. [184, 194] Therefore, $\chi^0_{\mathbf{0}\mathbf{0}}(\mathbf{q},i\omega) = O(|\mathbf{q}|^2)$ holds for small $\mathbf{q}$ and $\epsilon_{\mathbf{0}\mathbf{0}}(\mathbf{q},i\omega)$ remains finite for $\mathbf{q}\to 0$. For $\mathbf{q}\to 0$, the head, $W^{\text{c}}_{\mathbf{0}\mathbf{0}}(\mathbf{q})$ and the wings, $W^{\text{c}}_{\mathbf{G}\mathbf{0}}(\mathbf{q})$, $W^{\text{c}}_{\mathbf{0}\mathbf{G}'}(\mathbf{q})$ diverge as $1/q^2$ and $1/q$, respectively, see Eq. (4.4). At the same time $A^{n\mathbf{k},n\mathbf{k}-\mathbf{q}}_{\mathbf{0},\mathbf{q}} \xrightarrow{\mathbf{q}\to 0} 1$ and therefore, the entire expression for the Brillouin zone sampling in Eq. (4.2) diverges as $1/q^2$ for small q.

In the limit of very fine k-point sampling, we have $\sum_{\mathbf{q}} f(q) \to \Omega/(2\pi)^3 \int dq\, 4\pi q^2 f(q)$ such that the divergent terms $f(q) = 1/q^2$ and $f(q) = 1/q$ can be integrated. Thus, the Brilluoin zone sampling of the head and wings of W^{c} in Eq. (4.2) converge to a finite value when increasing the k-point mesh. The Γ-point has to be excluded from the k-point sampling of the head and the wings of W^{c} due to the division by 0 in Eq. (4.4). In the case of a finite k-point mesh with a distance $1/L = \sqrt[3]{1/\Omega}$ of the Γ-point to other k-points, the integration of the head $W^{\text{c}}_{\mathbf{0}\mathbf{0}}(\mathbf{q})$ in Eq. (4.2) for the Γ-point, scales as

$$\int_{B_{1/L}(\mathbf{0})} d^3\mathbf{q}\,\frac{1}{q^2} = 4\pi\int_0^{1/L} dq = \frac{4\pi}{L}\,, \tag{4.7}$$

where we used the notation $B_r(\mathbf{0})$ for the sphere in the Brillouin zone with radius r around the Γ-point. We miss the $1/L$-scaling $\mathbf{G}=0$ terms of W^{c} in our Γ-point implementation with Gaussian basis functions. This results in a slow convergence of $1/L$ for *GW* quasiparticles with the cell length L. To achieve a fast convergence of *GW* quasiparticle levels with the cell size, we derive a correction term for our Gaussian Γ-point *GW* implementation in this work.

Resolution of the identity with overlap metric

As in the *GW* implementation [30] in the CP2K package [72, 73], canonical *GW* implementations in a localized basis [11, 13, 175] employ the resolution of the identity (RI) to reduce the computational scaling of *GW* from $O(N^6)$ to $O(N^4)$. In this section, we give the equations that are used for the RI. The following index notation has been adopted: i, j (a, b) refer to occupied (virtual)

molecular orbitals (MOs) ψ; n, m to either occupied or virtual ones; $\mu, \nu, \lambda, \sigma$ to primary Gaussian basis functions ϕ and P, Q to auxiliary Gaussian RI basis functions φ. The primary basis functions ϕ_μ are employed to expand the KS orbitals while the RI basis $\{\varphi_P\}$ is used to expand *GW* quantities as the polarizability, dielectric function and the screened Coulomb interaction, as we show in Sec. 4.2.

In Γ-point-only *GW*, four-center Coulomb integrals

$$(ia|jb) = \int_{\Omega_{\text{cell}}} d\mathbf{r} \int_{\mathbb{R}^3} d\mathbf{r}' \psi_i(\mathbf{r})\psi_a(\mathbf{r})\psi_j(\mathbf{r}')\psi_b(\mathbf{r}')v(\mathbf{r},\mathbf{r}') \tag{4.8}$$

are appearing where $v(\mathbf{r},\mathbf{r}') = 1/|\mathbf{r}-\mathbf{r}'|$ denotes the Coulomb potential. All KS orbitals $\psi_n(\mathbf{r})$ in Eq. (4.8) are periodically repeated Bloch states at the Γ-point where we drop the $\mathbf{k}=\mathbf{0}$ index. Within the RI approximation based on the overlap metric, these integrals are factorized to [120]

$$(ia|jb)_{\text{RI}} = \sum_{PQRS} (iaP) S^{-1}_{PQ} V_{QR} S^{-1}_{RS} (S\, jb)\,. \tag{4.9}$$

The resolution of the identity can be seen as inserting $\text{Id} = \sum_{PQ} |P\rangle\, S^{-1}_{PQ}\, \langle Q|$ twice into Eq. (4.8) which is exact in the limit of a complete RI basis $\{P\}$. Here, the overlap matrix $\mathbf{S}$ in the RI basis, [195]

$$S_{PQ} = \int_{\mathbb{R}^3} d\mathbf{r}\; \varphi^{\text{P}}_P(\mathbf{r})\varphi_Q(\mathbf{r}) \tag{4.10}$$

is appearing since the Gaussian RI basis is non-orthogonal. The superscript P indicates that the functions are periodically repeated for condensed phase systems,

$$\varphi^{\text{P}}_Q(\mathbf{r}) = \sum_i \varphi_Q(\mathbf{r}-\mathbf{R}_i)\,, \tag{4.11}$$

where $\mathbf{R}_i$ are the lattice vectors and φ_Q is a Gaussian basis function being localized on a single atom. Further, $\mathbf{V}$ denotes the Coulomb matrix in the RI basis,

$$V_{PQ} = \int_{\Omega_{\text{cell}}} d\mathbf{r} \int_{\mathbb{R}^3} d\mathbf{r}'\, \varphi^{\text{P}}_P(\mathbf{r})\varphi^{\text{P}}_Q(\mathbf{r}')v(\mathbf{r},\mathbf{r}')\,. \tag{4.12}$$

In practice, we compute the RI-Coulomb matrix by Ewald summation [75, 196]

$$V_{PQ} = \sum_{\mathbf{G}>0} \frac{\varphi_P(\mathbf{G})\varphi_Q(\mathbf{G})}{|\mathbf{G}|^2}\,. \tag{4.13}$$

We refer to the computation of Coulomb matrix elements in Eq. (4.13) as Gaussian and Plane Waves method which is commonly used for the Hartree energy [127] and for wavefunction correlation methods [76, 77, 80, 197–200]. The $\mathbf{G}=0$ component is excluded from Eq. (4.13) due to a divergence for *s*-type basis functions P, Q with $\varphi_{P,Q}(\mathbf{G}{=}0) \neq 0$. The three-center overlap integrals $(\mu\nu P)$ are given by [195]

$$(\mu\nu P) = \int_{\mathbb{R}^3} d\mathbf{r}\, \phi^{\text{P}}_\mu(\mathbf{r})\phi^{\text{P}}_\nu(\mathbf{r})\varphi_P(\mathbf{r})\,. \tag{4.14}$$

The three-center overlap integrals (iaP) in Eq. (5.4) can be computed from Eq. (5.8) by

$$(iaP) = \sum_{\mu\nu} C_{\mu i} C_{\nu a} (\mu\nu P) \tag{4.15}$$

where the MO coefficients $C_{\mu n}$ are obtained from the expansion of MOs in the primary Gaussian basis from KS DFT

$$\psi_n(\mathbf{r}) = \sum_{\mu} C_{\mu n} \phi^{\mathrm{P}}_{\mu}(\mathbf{r}) \,. \tag{4.16}$$

The RI factorization from Eq. (5.4) can be expressed in a compact form as

$$(ia|jb)_{\mathrm{RI}} = \sum_{P} B^{ia}_{P} B^{jb}_{P} \,, \tag{4.17}$$

where the vector $\mathbf{b}^{ia}$ is given by

$$B^{ia}_{P} = \sum_{QR} (iaQ) S^{-1}_{QR} L_{RP} \,, \tag{4.18}$$

where $\mathbf{L}$ is the Cholesky decomposition of $\mathbf{V}$ from Eq. (4.13),

$$\mathbf{V} = \mathbf{L}\mathbf{L}^{\dagger} \,. \tag{4.19}$$

For later use, we define $\mathbf{a}^{ia}$ by

$$A^{ia}_{P} = \sum_{Q} (iaQ) S^{-1}_{QP} \,. \tag{4.20}$$

Screened Coulomb interaction, dielectric matrix and polarizability within RI

In this section, we rewrite the self-energy in a Gaussian basis to match the formulas in a plane-waves basis. For expanding *GW* quantities as the polarizability, the dielectric function and the screened Coulomb interaction, we employ the Gaussian RI basis from Sec. 4.2. This is the key to adopt the periodic correction from plane-waves *GW* to *GW* in a Gaussian basis.

As in Eq. (4.1), we compute the G_0W_0 quasiparticle energies in a Gaussian basis by

$$\varepsilon^{G_0W_0}_n = \varepsilon^{\mathrm{DFT}}_n + Z_n \mathrm{Re} \, \langle n | \Sigma^{\mathrm{c}}_n(\varepsilon^{\mathrm{DFT}}_n) + \Sigma^{\mathrm{x}} - V^{\mathrm{xc}}_{\mathrm{DFT}} | n \rangle \tag{4.21}$$

where we have dropped the k-point index for a Γ-point-only implementation. The correlation part of the self-energyis is calculated for imaginary frequencies and analytically continued to real energies. [13, 24, 38, 39, 59, 71, 124–126] In a Gaussian basis, the correlation self-energy can be computed as [13, 30, 39]

$$\Sigma^{\mathrm{c}}_n(i\omega) = -\frac{1}{2\pi} \sum_{m} \int_{-\infty}^{\infty} d\omega' \frac{1}{i(\omega - \omega') + \varepsilon_{\mathrm{F}} - \varepsilon_m} \sum_{PQ} B^{nm}_{P} \left[[1 - \Pi(i\omega')]^{-1}_{PQ} - \delta_{PQ} \right] B^{mn}_{Q} \,, \tag{4.22}$$

where

$$\Pi_{PQ}(i\omega) = 2 \sum_{ia} B^{ia}_{P} \frac{\varepsilon_i - \varepsilon_a}{\omega^2 + (\varepsilon_i - \varepsilon_a)^2} B^{ia}_{Q} \,. \tag{4.23}$$

Inserting Eq. (5.11) into Eq. (4.22) and using the definition in Eq. (4.20) yields

$$\Sigma^{\mathrm{c}}_n(i\omega) = -\frac{1}{2\pi} \sum_{m} \int_{-\infty}^{\infty} d\omega' \frac{1}{i(\omega - \omega') + \varepsilon_{\mathrm{F}} - \varepsilon_m} \sum_{PQ} A^{nm}_{P} W^{\mathrm{c}}_{PQ}(i\omega') A^{mn}_{Q} \,, \tag{4.24}$$

where the correlation part of the screened Coulomb potential $\mathbf{W}^{\mathrm{c}}(i\omega)$ is expanded in the Gaussian RI basis,

$$W^{\mathrm{c}}_{PQ}(i\omega) = \sum_{RT} L_{PR} \left[\epsilon^{-1}_{RT}(i\omega) - \delta_{RT} \right] L^{\dagger}_{TQ} \,, \tag{4.25}$$

and the symmetric dielectric matrix $\boldsymbol{\epsilon}(i\omega)$ in the RI basis is given by $\boldsymbol{\epsilon}(i\omega) = \mathbf{1} - \boldsymbol{\Pi}(i\omega)$ with elements

$$\epsilon_{PQ}(i\omega) = \delta_{PQ} - \sum_{ia} \sum_{RT} L^{\dagger}_{PR} A^{ia}_{R} \frac{2(\varepsilon_i - \varepsilon_a)}{\omega^2 + (\varepsilon_i - \varepsilon_a)^2} A^{ia}_{T} L_{TQ} \,, \tag{4.26}$$

where we have used Eq. (5.11), (4.20) and (4.23). In matrix notation, we have

$$\boldsymbol{\epsilon}(i\omega) = \mathbf{1} - \mathbf{L}^{\dagger} \boldsymbol{\chi}^{0}(i\omega) \mathbf{L} \tag{4.27}$$

and the polarizability $\boldsymbol{\chi}^{0}(i\omega)$ in the RI basis with elements $\chi^{0}_{PQ}(i\omega)$ reads

$$\chi^{0}_{PQ}(i\omega) = \sum_{ia} A^{ia}_{P} \frac{2(\varepsilon_i - \varepsilon_a)}{\omega^2 + (\varepsilon_i - \varepsilon_a)^2} A^{ia}_{Q} \,. \tag{4.28}$$

As it can be seen by comparing Eq. (4.24) and (4.2), as well as Eq. (4.28) and (4.6), the RI basis $\{\varphi_P\}$ corresponds to a plane-waves basis in plane-waves *GW*. We neglect the $\mathbf{G} = 0$ component when computing the bare Coulomb interaction in the RI basis in Eq. (4.13) and thus our RI basis only spans the subspace of plane waves with $|\mathbf{G}| > 0$. For a correction that removes the slow $1/L$ convergence of *GW* with the cell size L from Sec. 4.2, we add the $\mathbf{G} = 0$ function as additional function to the RI basis, as we show in the following section.

Setting the G = 0 component of Gaussian RI basis functions to zero and adding a single G = 0 function to the RI basis

Following the discussion at the end of the last section, we describe in this section how to add the $\mathbf{G} = 0$ function to the Gaussian RI basis.

Consider N_{aux} Gaussian RI basis functions $\varphi_1, \ldots, \varphi_{N_{\mathrm{aux}}}$ where all Gaussian RI functions exhibit a vanishing $\mathbf{G} = \mathbf{0}$ component. This redefinition does not affect the *GW* results since the $\mathbf{G} = \mathbf{0}$ component is not used, see Eq. (4.13). Now, we add the $\mathbf{G} = \mathbf{0}$ function to the RI basis and the new RI basis consists of $N_{\mathrm{aux}}+1$ functions $\varphi_0, \varphi_1, \ldots, \varphi_{N_{\mathrm{aux}}}$, where φ_0 is the $\mathbf{G} = \mathbf{0}$ function which is a normalized constant in real space,

$$\varphi_0(\mathbf{r}) = \Omega^{-1/2}_{\mathrm{cell}} \, \delta_{\mathbf{r} \in \Omega_{\mathrm{cell}}} \,. \tag{4.29}$$

Then, the Γ-point-only overlap matrix $\mathbf{S}$ reads

$$\mathbf{S} \equiv \begin{pmatrix} S_{\mathrm{head}} & \mathbf{S}_{\mathrm{wings}} \\ \mathbf{S}^{\dagger}_{\mathrm{wings}} & \mathbf{S}_{\mathrm{body}} \end{pmatrix} = \begin{pmatrix} 1 & \mathbf{0} \\ \mathbf{0} & \mathbf{S}_{\mathrm{body}} \end{pmatrix} \tag{4.30}$$

where $\mathbf{S}_{\mathrm{body}}$ is the overlap matrix of the Gaussian RI basis. The wings of $\mathbf{S}$ are zero since, according to the redefinition from above, all RI Gaussian basis functions $P \in [1, N_{\mathrm{aux}}]$ do not exhibit a $\mathbf{G} = \mathbf{0}$ component:

$$S_{0P} = S_{P0} = \sum_{\mathbf{G}} \varphi_0(\mathbf{G}) \varphi_P(\mathbf{G}) = 0 \,. \tag{4.31}$$

k-dependent polarizability, dielectric function and screened interaction

In this section, we expand the polarizability, the dielectric function and the screened Coulomb interaction in the Gaussian RI basis with additional $\mathbf{G} = \mathbf{0}$ function from Sec. 4.2. Moreover, we adopt *k*-points for head and wing elements from plane-waves *GW*, see Sec. 4.2.

We start with the polarizability using Γ-point-only for the body [59]

$$\chi^0(i\omega, \mathbf{k}) = \begin{pmatrix} \chi^0_{\text{head}}(i\omega, \mathbf{k}) & \chi^0_{\text{wings}}(i\omega, \mathbf{k}) \\ \left(\chi^0_{\text{wings}}(i\omega, \mathbf{k})\right)^\dagger & \chi^0_{\text{body}}(i\omega) \end{pmatrix} . \tag{4.32}$$

Omitting the integration over the first Brillouin zone for the polarizability, its head is given by Eq. (4.6)

$$\chi^0_{00}(i\omega, \mathbf{k}) = \frac{1}{\Omega_{\text{cell}}} \sum_{ia} \frac{2(\varepsilon_i - \varepsilon_a)}{\omega^2 + (\varepsilon_i - \varepsilon_a)^2} \left| \langle \psi_{i\mathbf{0}} | e^{i\mathbf{kr}} | \psi_{a-\mathbf{k}} \rangle \right|^2 . \tag{4.33}$$

The prefactor $1/\Omega_{\text{cell}}$ results from the normalization of $\varphi_0(\mathbf{r})$ from Eq. (4.29). The wings are given by

$$\chi^0_{0Q}(i\omega, \mathbf{k}) = \frac{1}{\Omega^{1/2}_{\text{cell}}} \sum_{ia} A^{ia}_Q \frac{2(\varepsilon_i - \varepsilon_a)}{\omega^2 + (\varepsilon_i - \varepsilon_a)^2} \langle \psi_{i\mathbf{0}} | e^{i\mathbf{kr}} | \psi_{a-\mathbf{k}} \rangle \tag{4.34}$$

using the Γ-point for the RI basis function Q, cf. Eq. (4.6) and (4.28).

The dielectric matrix from Eq. (4.27) for *k*-points is given by

$$\boldsymbol{\epsilon}(i\omega, \mathbf{k}) \overset{(4.5)}{=} \mathbf{1} - \mathbf{L}^\dagger(\mathbf{k}) \boldsymbol{\chi}^0(i\omega, \mathbf{k}) \mathbf{L}(\mathbf{k}) , \tag{4.35}$$

where $\mathbf{L}(\mathbf{k})$ is the Cholesky decomposition of the Coulomb matrix

$$\mathbf{V}(\mathbf{k}) \equiv \begin{pmatrix} V_{\text{head}}(\mathbf{k}) & \mathbf{0} \\ \mathbf{0} & \mathbf{V}_{\text{body}} \end{pmatrix} = \mathbf{L}(\mathbf{k}) \mathbf{L}^\dagger(\mathbf{k}) . \tag{4.36}$$

The elements of $\mathbf{V}(\mathbf{k})$ are given by [184, 195]

$$V_{00}(\mathbf{k}) = \frac{4\pi}{|\mathbf{k}|^2} , \quad V_{PQ} = \sum_{\mathbf{G}>0} \frac{\varphi_P(\mathbf{G}) \varphi_Q(\mathbf{G})}{|\mathbf{G}|^2} , \tag{4.37}$$

which are well-defined for $\mathbf{k} \neq 0$. The wings of $\mathbf{V}(\mathbf{k})$ vanish since $\varphi_0(\mathbf{G}) = \delta_{\mathbf{G},\mathbf{0}}$ and $\varphi_P(\mathbf{G} = 0) = 0$ for the remaining Gaussian RI functions. For $\mathbf{V}_{\text{body}}$, only the Γ point is used. Then, the Cholesky decomposition $\mathbf{L}(\mathbf{k})$ of $\mathbf{V}(\mathbf{k})$ reads

$$\mathbf{L}(\mathbf{k}) = \begin{pmatrix} \sqrt{4\pi}/|\mathbf{k}| & \mathbf{0} \\ \mathbf{0} & \mathbf{L}_{\text{body}} \end{pmatrix} , \tag{4.38}$$

where $\mathbf{L}_{\text{body}}$ is the Cholesky decomposition of the body Coulomb matrix $\mathbf{V}_{\text{body}}$.

The head, wings and the body of the dielectric matrix from Eq. (4.35) are defined as

$$\boldsymbol{\epsilon}(i\omega, \mathbf{k}) \equiv \begin{pmatrix} \epsilon_{\text{head}}(i\omega, \mathbf{k}) & \boldsymbol{\epsilon}_{\text{wings}}(i\omega, \mathbf{k}) \\ \boldsymbol{\epsilon}^\dagger_{\text{wings}}(i\omega, \mathbf{k}) & \boldsymbol{\epsilon}_{\text{body}}(i\omega) \end{pmatrix} \tag{4.39}$$

and read when using Eq. (5.29) and (4.38)

$$\epsilon_{\text{head}}(i\omega, \mathbf{k}) = 1 - 4\pi\chi^0_{\text{head}}(i\omega, \mathbf{k})/|\mathbf{k}|^2\,, \tag{4.40}$$

$$\boldsymbol{\epsilon}_{\text{wings}}(i\omega, \mathbf{k}) = -\sqrt{4\pi}\,\boldsymbol{\chi}^0_{\text{wings}}(i\omega, \mathbf{k})\mathbf{L}_{\text{body}}/|\mathbf{k}|\,, \tag{4.41}$$

$$\boldsymbol{\epsilon}_{\text{body}}(i\omega) = \mathbf{1} - \mathbf{L}^\dagger_{\text{body}}\boldsymbol{\chi}^0_{\text{body}}(i\omega)\mathbf{L}_{\text{body}}\,. \tag{4.42}$$

Its inverse $\boldsymbol{\epsilon}^{\text{inv}}(i\omega, \mathbf{k})$ is given by (for $\mathbf{k} \neq \mathbf{0}$)

$$\boldsymbol{\epsilon}^{\text{inv}}(i\omega, \mathbf{k}) \equiv \begin{pmatrix} \epsilon^{\text{inv}}_{\text{head}}(i\omega, \mathbf{k}) & \boldsymbol{\epsilon}^{\text{inv}}_{\text{wings}}(i\omega, \mathbf{k}) \\ \boldsymbol{\epsilon}^{\text{inv},\dagger}_{\text{wings}}(i\omega, \mathbf{k}) & \boldsymbol{\epsilon}^{\text{inv}}_{\text{body}}(i\omega, \mathbf{k}) \end{pmatrix} := \boldsymbol{\epsilon}^{-1}(i\omega, \mathbf{k})\,, \tag{4.43}$$

where its elements are given by inverting Eq. (4.39)

$$\epsilon^{\text{inv}}_{\text{head}}(i\omega, \mathbf{k}) = 1/[\epsilon_{\text{head}}(i\omega, \mathbf{k}) - \boldsymbol{\epsilon}_{\text{wings}}(i\omega, \mathbf{k})\boldsymbol{\epsilon}^{-1}_{\text{body}}(i\omega)\boldsymbol{\epsilon}^\dagger_{\text{wings}}(i\omega, \mathbf{k})]\,. \tag{4.44}$$

$$\boldsymbol{\epsilon}^{\text{inv}}_{\text{wings}}(i\omega, \mathbf{k}) = -\epsilon^{\text{inv}}_{\text{head}}(i\omega, \mathbf{k})\boldsymbol{\epsilon}_{\text{wings}}(i\omega, \mathbf{k})\boldsymbol{\epsilon}^{-1}_{\text{body}}(i\omega) \tag{4.45}$$

$$\boldsymbol{\epsilon}^{\text{inv}}_{\text{body}}(i\omega, \mathbf{k}) = \boldsymbol{\epsilon}^{-1}_{\text{body}}(i\omega) + \epsilon^{\text{inv}}_{\text{head}}(i\omega, \mathbf{k})\boldsymbol{\epsilon}^{-1}_{\text{body}}(i\omega)\boldsymbol{\epsilon}^\dagger_{\text{wings}}(i\omega, \mathbf{k})\boldsymbol{\epsilon}_{\text{wings}}(i\omega, \mathbf{k})\boldsymbol{\epsilon}^{-1}_{\text{body}}(i\omega)\,. \tag{4.46}$$

Analogously to Eq. (4.4) and Eq. (4.25), we obtain $\mathbf{W}^{\text{c}}(i\omega, \mathbf{k})$ for $\mathbf{k} \neq \mathbf{0}$ as

$$\mathbf{W}^{\text{c}}(i\omega, \mathbf{k}) = \mathbf{L}(\mathbf{k})(\boldsymbol{\epsilon}^{\text{inv}}(i\omega, \mathbf{k}) - \mathbf{1})\mathbf{L}^\dagger(\mathbf{k}) \tag{4.47}$$

$$= \begin{pmatrix} 4\pi(\epsilon^{\text{inv}}_{\text{head}}(i\omega, \mathbf{k}) - 1)/|\mathbf{k}|^2 & \sqrt{4\pi}\,\boldsymbol{\epsilon}^{\text{inv}}_{\text{wings}}(i\omega, \mathbf{k})\mathbf{L}_{\text{body}}/|\mathbf{k}| \\ \sqrt{4\pi}\,\mathbf{L}^\dagger_{\text{body}}\boldsymbol{\epsilon}^{\text{inv},\dagger}_{\text{wings}}(i\omega, \mathbf{k})/|\mathbf{k}| & \mathbf{L}^\dagger_{\text{body}}(\boldsymbol{\epsilon}^{\text{inv}}_{\text{body}}(i\omega, \mathbf{k}) - \mathbf{1})\mathbf{L}_{\text{body}} \end{pmatrix}. \tag{4.48}$$

k-point sampling for the self-energy in the limit of $k \to 0$

In order to identify, which contributions have to be taken into account for the correction in periodic *GW* in a Gaussian basis, we examine the behaviour of the *k*-point sum in the self-energy at the Γ-point, $\mathbf{k} \to 0$.

Comparing Eq. (4.2) and Eq. (4.24) and assuming flat bands ($\varepsilon_{m\mathbf{q}} = \varepsilon_m$), we obtain:

$$\Sigma^{\text{c}}_n(i\omega) = -\frac{1}{2\pi}\sum_m \int_{-\infty}^{\infty} d\omega' \frac{1}{i(\omega - \omega') + \varepsilon_{\text{F}} - \varepsilon_m} \frac{1}{N_{\mathbf{k}}} \sum_{\mathbf{k}\neq 0} \sum_{PQ} A^{n\mathbf{0},m-\mathbf{k}}_{P\mathbf{k}} W^{\text{c}}_{PQ}(i\omega, \mathbf{k}) \left(A^{n\mathbf{0},m-\mathbf{k}}_{Q\mathbf{k}}\right)^*\,. \tag{4.49}$$

The summation over the RI indices P, Q include the summation over the $\mathbf{G} = 0$ RI function. Due to the divergence of the head $W^{\text{c}}_{00}(i\omega, \mathbf{k})$ and the wings, $W^{\text{c}}_{P0}(i\omega, \mathbf{k})$ and $W^{\text{c}}_{0Q}(i\omega, \mathbf{k})$, for $\mathbf{k} \to 0$, the Γ point is excluded from the summation. The three-center overlap integrals in the limit of small $\mathbf{k}$ for the $\mathbf{G} = \mathbf{0}$ RI function are given by [184, 194]

$$A^{n\mathbf{0},n-\mathbf{k}}_{0\mathbf{k}} = \langle\psi_{n\mathbf{0}}|e^{i\mathbf{k}\mathbf{r}}|\psi_{n-\mathbf{k}}\rangle \overset{\mathbf{k}\to 0}{=} 1 + i\mathbf{k}\,\langle\psi_{n\mathbf{0}}|\mathbf{r}|\psi_{n\mathbf{0}}\rangle\,, \tag{4.50}$$

$$A^{n\mathbf{0},m-\mathbf{k}}_{0\mathbf{k}} = \langle\psi_{n\mathbf{0}}|e^{i\mathbf{k}\mathbf{r}}|\psi_{m-\mathbf{k}}\rangle \underset{n\neq m}{\overset{\mathbf{k}\to 0}{=}} i\mathbf{k}\,\langle\psi_{n\mathbf{0}}|\mathbf{r}|\psi_{m\mathbf{0}}\rangle\,, \tag{4.51}$$

Then, the sum over RI basis functions in Eq. (4.49) for $n = m$ using the matrix-vector notation with the row vector $(\mathbf{a}^{nn}(\mathbf{k}))_P = A_{P\mathbf{k}}^{n\mathbf{0},m-\mathbf{k}}$ in the limit $\mathbf{k} \to 0$ turns into

$$\begin{aligned}
&\mathbf{a}^{nn}(\mathbf{k})\mathbf{W}^{\mathrm{c}}(i\omega,\mathbf{k})\,(\mathbf{a}^{nn}(\mathbf{k}))^{\dagger} \overset{\mathbf{k}\to 0}{=} \\
&\overset{(4.50)}{=} \begin{pmatrix} 1 + i\mathbf{k}\,\langle\psi_{n\mathbf{0}}|\mathbf{r}|\psi_{n\mathbf{0}}\rangle & \mathbf{a}^{nn}_{\mathrm{body}} \end{pmatrix} \begin{pmatrix} 4\pi(\epsilon^{\mathrm{inv}}_{\mathrm{head}}(i\omega,\mathbf{k}) - 1)/|\mathbf{k}|^2 & \sqrt{4\pi}\,\boldsymbol{\epsilon}^{\mathrm{inv}}_{\mathrm{wings}}(i\omega,\mathbf{k})\mathbf{L}_{\mathrm{body}}/|\mathbf{k}| \\ \sqrt{4\pi}\,\mathbf{L}^{\dagger}_{\mathrm{body}}\boldsymbol{\epsilon}^{\mathrm{inv},\dagger}_{\mathrm{wings}}(i\omega,\mathbf{k})/|\mathbf{k}| & \mathbf{L}^{\dagger}_{\mathrm{body}}(\boldsymbol{\epsilon}^{\mathrm{inv}}_{\mathrm{body}}(i\omega,\mathbf{k}) - \mathbf{1})\mathbf{L}_{\mathrm{body}} \end{pmatrix} \\
&\qquad \times \begin{pmatrix} 1 - i\mathbf{k}\,\langle\psi_{n\mathbf{0}}|\mathbf{r}|\psi_{n\mathbf{0}}\rangle \\ (\mathbf{a}^{nn}_{\mathrm{body}})^{\mathrm{T}} \end{pmatrix}
\end{aligned} \tag{4.52}$$

$$= \frac{4\pi}{|\mathbf{k}|^2}\,(\epsilon^{\mathrm{inv}}_{\mathrm{head}}(i\omega,\mathbf{k}) - 1) - \frac{\sqrt{4\pi}}{|\mathbf{k}|^1}\,\mathrm{Re}\left(2\boldsymbol{\epsilon}^{\mathrm{inv}}_{\mathrm{wings}}(i\omega,\mathbf{k})\mathbf{L}_{\mathrm{body}}(\mathbf{a}^{nn}_{\mathrm{body}})^{\mathrm{T}}\right) + O\left(\frac{1}{|\mathbf{k}|^0}\right) \tag{4.53}$$

$$= \frac{4\pi}{|\mathbf{k}|^2}\,(\epsilon^{\mathrm{inv}}_{\mathrm{head}}(i\omega,\mathbf{k}) - 1) + O\left(\frac{1}{|\mathbf{k}|^0}\right). \tag{4.54}$$

The $1/|\mathbf{k}|^1$ term in Eq. (4.54) vanishes due to $\mathrm{Re}(\boldsymbol{\epsilon}^{\mathrm{inv}}_{\mathrm{wings}}(i\omega,\mathbf{k})) = 0$ for $\mathbf{k} \to \mathbf{0}$ [see Eqs. (4.45), (4.42), and (4.34)] and $\mathrm{Im}(\mathbf{L}_{\mathrm{body}}(\mathbf{a}^{nn}_{\mathrm{body}})^{\mathrm{T}}) = 0$. Therefore, a correction due to wing contributions of W^{c} seems to be of minor importance compared to the head when using a Gaussian basis.

For the contraction with $n \neq m$ in Eq. (4.49), we have

$$\mathbf{a}^{nm}(\mathbf{k})\mathbf{W}^{\mathrm{c}}(i\omega,\mathbf{k})\,(\mathbf{a}^{mn}(\mathbf{k}))^{\dagger} \overset{(4.51)}{=} O(1/|\mathbf{k}|^0)\,. \tag{4.55}$$

Therefore, we do not include $A_{0\mathbf{k}}^{n\mathbf{0},m-\mathbf{k}}$ matrix elements with $n \neq m$ from Eq. (4.49) in the periodic correction scheme.

Then, the k-point sum for the periodic correction from Eq. (4.49) only includes the head of $\mathbf{W}^{\mathrm{c}}$ and matrix elements $A_{0\mathbf{k}}^{n\mathbf{0},n-\mathbf{k}}$ with $n = m$:

$$\sum_{mPQ}\sum_{\mathbf{k}\neq 0} A_{P\mathbf{k}}^{n\mathbf{0},m-\mathbf{k}} W^{\mathrm{c}}_{PQ}(i\omega,\mathbf{k})\left(A_{Q\mathbf{k}}^{n\mathbf{0},m-\mathbf{k}}\right)^{*} = \sum_{\mathbf{k}\neq 0}\frac{4\pi}{|\mathbf{k}|^2}\left(\epsilon^{\mathrm{inv}}_{\mathrm{head}}(i\omega,\mathbf{k}) - 1\right)\left|\langle\psi_{n\mathbf{0}}|e^{i\mathbf{k}\mathbf{r}}|\psi_{n-\mathbf{k}}\rangle\right|^2 + O\left(\frac{1}{|\mathbf{k}|^0}\right). \tag{4.56}$$

The divergence $1/|\mathbf{k}|^2$ in Eq. (4.56) is integrable, as discussed in Sec. 4.2.

Algorithm of the correction scheme for periodic *GW* with Gaussians

1. Setup a $\mathbf{k}$-point mesh excluding the Γ-point.
2. Compute $\chi^0_{\mathrm{head}}(i\omega,\mathbf{k})$ according to Eq. (4.33):

$$\chi^0_{\mathrm{head}}(i\omega,\mathbf{k}) = \frac{1}{\Omega_{\mathrm{cell}}}\sum_{ia}\frac{2(\varepsilon_i - \varepsilon_a)}{\omega^2 + (\varepsilon_i - \varepsilon_a)^2}\left|\langle\psi_{i\mathbf{0}}|e^{i\mathbf{k}\mathbf{r}}|\psi_{a-\mathbf{k}}\rangle\right|^2, \tag{4.57}$$

   According to what has been discussed in the previous section, we assume the wings to have a small contribution and we exclude their computation.
3. Compute the head of the dielectric matrix from Eq. (4.42):

$$\epsilon_{\mathrm{head}}(i\omega,\mathbf{k}) = 1 - 4\pi\chi^0_{\mathrm{head}}(i\omega,\mathbf{k})/|\mathbf{k}|^2\,. \tag{4.58}$$

4. Compute the head of the inverse dielectric matrix $\boldsymbol{\epsilon}^{\text{inv}}$ according to Eq. (4.44) with neglecting wing contributions:

$$\epsilon^{\text{inv}}_{\text{head}}(i\omega, \mathbf{k}) = 1/\epsilon_{\text{head}}(i\omega, \mathbf{k})\,. \tag{4.59}$$

5. Compute the correction term $\Delta_{nn}(i\omega)$ for the head of W^{c} in $1/\Omega \sum_{\mathbf{k}} \mathbf{a}^{nm}(\mathbf{k})\mathbf{W}^{\text{c}}(i\omega, \mathbf{k})\,(\mathbf{a}^{nm}(\mathbf{k}))^{\dagger}$ in Eq. (4.49) according to Eq. (4.56) as:

$$\Delta_{nn}(i\omega) = \frac{4\pi}{\Omega} \sum_{\mathbf{k}\neq 0} \frac{\epsilon^{\text{inv}}_{\text{head}}(i\omega, \mathbf{k}) - 1}{|\mathbf{k}|^2} \left|\langle \psi_{n\mathbf{0}} | e^{i\mathbf{kr}} | \psi_{n-\mathbf{k}} \rangle\right|^2 . \tag{4.60}$$

Then, the Γ-point-only correlation self-energy from Eq. (4.22) including the correction term $\Delta_{nn}(i\omega)$ reads

$$\begin{aligned} \Sigma^{\text{c}}_n(i\omega) = &- \frac{1}{2\pi} \sum_m \int_{-\infty}^{\infty} d\omega' \frac{1}{i(\omega - \omega') + \varepsilon_{\text{F}} - \varepsilon_m} \\ &\times \Big[\sum_{PQ} B^{nm}_P \Big[[1 - \Pi(i\omega')]^{-1}_{PQ} - \delta_{PQ} \Big] B^{mn}_Q + \Delta_{nn}(i\omega')\delta_{nm} \Big]. \end{aligned} \tag{4.61}$$

4.3 Benchmark calculations

Computational details

For all calculations reported here, we employ the Gaussian and plane waves scheme (GPW) [27] together with Goedecker-Teter-Hutter (GTH) type pseudopotentials [130, 131] for the underlying generalized Kohn-Sham (KS) equations with the PBE functional [96] as implemented in CP2K [72, 73, 127–129]. For the exchange self-energy from Eq. (4.21), we employ a real-space truncation of the Coulomb interaction [116, 188, 189] with a truncation radius equal to half of the cell size.

For expanding the KS orbitals, we use correlation-consistent (cc) Gaussian basis sets [133, 134] which are specifically designed for the use with GTH pseudopotentials. The basis set extrapolated *GW* results are obtained from the cc double-, triple- and quadrupole zeta split-valence quality basis sets by a linear regression against the inverse of the total number of basis functions. [12, 30, 71] The extrapolation in the basis set for KS orbitals typically results in statistical errors below 0.1 eV for *GW* quasiparticle levels. [71]

The Gaussian RI basis set is used for expanding the screened Coulomb interaction and is designed for the use with a specific basis set for the KS orbitals, as described in Ref. [136]. Typically, the convergence of *GW* quasiparticle energies with respect to the RI basis is fast such that an extrapolation is not necessary for the RI basis.

The Berry phase $\langle \phi_\mu | e^{i\mathbf{kr}} | \phi_\nu \rangle$ in the Gaussian basis is available in standard quantum chemistry codes for calculating dipole moments in periodic systems [201–206]. To ensure numerical stability when computing the Berry phase in the Gaussian basis, we employ a non-diffuse auxiliary basis and project the MO coefficients into this subspace. [138, 139] We employ $6\times6\times6$ and $12\times12\times12$ *k*-point meshes and extrapolate the results to the infinitely dense *k*-point mesh.

As benchmark systems, we employ solid Lithium hydride, diamond, and the molecular crystals build of ammonia and carbon dioxide molecules. For LiH and diamond, we employ the experimental lattice constants of 4.084 Å and 3.567 Å, respectively. For both molecular crystals, we employ the geometry from Ref. [207].

Reference	Diamond	Lithium hydride
This work	5.48 ± 0.06 eV	4.66 ± 0.04 eV
Ref. [208]	5.54 eV	–
Ref. [209]	5.55 eV	–
Ref. [22]	5.50 eV	–
Ref. [210]	–	4.75 eV
Experiment [22, 211]	5.48 eV	4.99 eV

Table 4.1: G_0W_0@PBE HOMO-LUMO gap of diamond and solid Lithium hydride and measured fundamental gaps from the literature.

Results

The basis-set extrapolated G_0W_0@PBE fundamental gaps as function of the cell size are shown in Fig. 4.1. We compare the results without correction [Eq. (4.21) together with Eq. (4.22), blue] with the results employing the correction [Eq. (4.21) together with Eq. (4.61), green].

For the uncorrected G_0W_0@PBE fundamental gaps (blue), we observe a slow $1/L$ convergence with the cell length L. The extrapolation with the inverse cell length yields the G_0W_0@PBE gaps of 4.66 ± 0.04 eV for LiH, 5.48 ± 0.06 eV for diamond, 7.49 ± 0.11 eV for the NH_3 crystal and 10.51 ± 0.07 eV for the CO_2 crystal. The statistical error includes both errors from basis set and the supercell extrapolation. These values are in good agreement with (indirect) fundamental gaps from the literature, see Table 4.1. For both molecular crystals, we are not aware of fundamental gaps from the literature. We conclude that using basis set and supercell extrapolation, a Γ-point-only G_0W_0 implementation can give accurate fundamental gaps.

In practice, the extrapolation of the supercell can be impossible since the unit cell is already large if disordered systems are considered, e.g. in molecular dynamics simulations [14, 172, 173]. For GW calculations of these systems, a periodic correction is necessary. In Fig. 4.1, we show the fundamental G_0W_0@PBE gaps when using our correction from Sec. 4.2. We observe that the gaps computed with the correction are a factor three to ten closer to the extrapolated gap than the non-correct ones. For the largest supercells which correspond to typical cells in molecular dynamics simulations, the corrected G_0W_0@PBE gaps are all within 0.5 eV compared to the extrapolated values. This improves substantially compared to the uncorrected gaps and turns the Γ-point-only GW method in a Gaussian basis into a useful tool for computing quasiparticle levels in periodic, disordered systems where large unit cells are necessary.

4.4 Conclusions

We have presented a correction scheme for periodic Γ-point-only GW calculations in a Gaussian basis. The correction is derived by adding the $\mathbf{G} = \mathbf{0}$ function to the resolution-of-the-identity (RI) basis. As a second step, we apply k-point sampling for the correction mimicking an infinitely large cell for the head matrix elements, i.e. the diagonal elements corresponding to the $\mathbf{G} = \mathbf{0}$ function in the RI basis. For the benchmark systems solid Lithium hydride, diamond and two molecular crystals, the dependence of the corrected GW quasiparticle levels on the cell size is reduced by a factor of three to ten compared to GW calculations without correction. The correction scheme comes along with negligible computational cost and enables GW calculations for supercells containing hundreds of atoms with Gaussian basis functions.

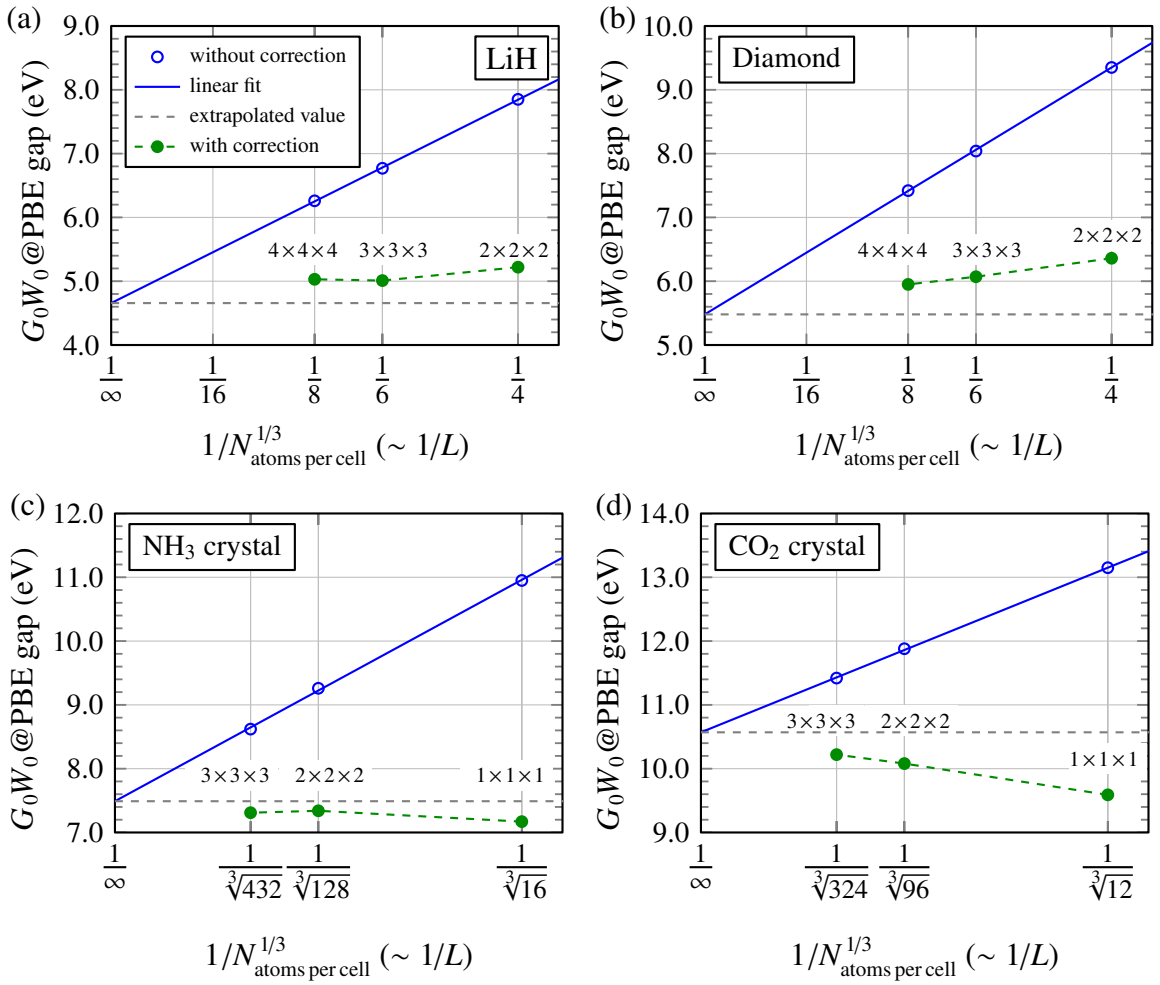

Figure 4.1: Basis-set extrapolated G_0W_0@PBE fundamental gaps of solid Lithium hydride, diamond and the molecular crystals NH_3 and CO_2 as function of the supercell size. The blue circles are the gaps computed without correction, see Eq. (4.21) together with Eq. (4.22), where the blue line represents the linear regression. The intersept of the regression line with the ordinate determines the supercell extrapolated gap which is indicated by the dashed gray line. By the green dots, we show the gaps being computed with the periodic correction from Eq. (4.21) together with Eq. (4.61) where the dashed green lines are simple connections of the data points to guide the eye. It is observed that the corrected gaps are much closer to the supercell extrapolated gap compared to the non-corrected gaps.

Chapter 5

Cubic-scaling RPA correlation energy calculations using a Gaussian basis

The following chapter is a reprint of Ref. [195]. We present an algorithm for computing the correlation energy in the random phase approximation (RPA) in a Gaussian basis requiring $O(N^3)$ operations and $O(N^2)$ memory. The method is based on the resolution of the identity (RI) with the overlap metric, a reformulation of RI-RPA in the Gaussian basis, imaginary time and imaginary frequency integration techniques and the use of sparse linear algebra. Additional memory reduction without extra computations can be achieved by an iterative scheme which overcomes the memory bottleneck of canonical RPA implementations. We report a massively parallel implementation which is the key for the application to large systems. Finally, cubic-scaling RPA is applied to two thousand water molecules using a correlation-consistent triple-zeta quality basis.

5.1 Introduction

The random phase approximation (RPA) for computing electron correlation energies [212, 213] has emerged as an accurate tool for predicting properties of isolated molecules [214–222] and condensed phase systems [80, 198–200, 223–238]. In its simplest form, the RPA total energy is the sum of the Hartree-Fock (HF) energy E^{HF} and the RPA correlation energy $E_{\mathrm{c}}^{\mathrm{RPA}}$, [123]

$$E = E^{\mathrm{HF}}[\{\psi_n\}] + E_{\mathrm{c}}^{\mathrm{RPA}}[\{\psi_n, \varepsilon_n\}]\,. \tag{5.1}$$

The RPA total energy is typically evaluated after a self-consistent field (SCF) procedure, i.e., the converged molecular orbitals ψ_n from the SCF and their corresponding eigenvalues ε_n are employed to evaluate the HF energy and the RPA correlation energy. RPA combines a number of attractive features, most importantly that long-range dispersion is included – in contrast to semilocal density functionals. [78, 123, 219, 239–243]

The drawback connected with RPA is the computational cost: For canonical implementations of RPA in a plane-waves basis [244–246] or in a localized basis within the resolution of the identity (RI) [13, 75, 76, 123], the computational cost of RPA scales as $O(N^4)$ with respect to the system size N. Recently, low-scaling RPA algorithms have been explored: Moussa [247] employed the connection of RPA to coupled-cluster theory for constructing an $O(N^3)$ scaling RPA+SOSEX algorithm. In this case, the cubic scaling has been demonstrated employing chains of hydrogen atoms. Kaltak *et al.* [248] use a plane-wave basis, minimax grids in imaginary frequency and imaginary time to arrive at a cubic-scaling algorithm. They applied their implementation for studying supercells of silicon [249] containing up to 256 atoms. Linear-scaling RPA algorithms have also been reported [250–253] which either rely on localization techniques [250], stochastic

sampling [251, 252] or sparsity of density matrices [253]. Large-scale applications of linear-scaling RPA have only been reported so far in Ref. [251] and [252] using stochastic sampling.

In this work, we employ localized Gaussian basis functions. We combine the $O(N^4)$ RI-RPA method by Eshuis *et al.* [123] and the minimax grids in imaginary frequency and imaginary time from Kaltak *et al.* [248] To achieve the cubic scaling algorithm, we rely on the sparsity introduced by the RI approximation with the overlap metric [120, 254, 255] combined with the back transformation from occupied and virtual orbitals to Gaussian atomic orbitals [253]. Practically, the sparsity is efficiently handled by the DBCSR (Distributed Block Compressed Sparse Row) library [129, 256]. Stochastic sampling, sparsity of density matrices and localization techniques are not necessary for the $O(N^3)$ scaling behavior in our algorithm.

This chapter is organized as follows: In Sec. 5.2, we review the resolution of the identity with the overlap metric. As we explain in Sec. 5.3, cubic-scaling RPA is well-known in a formulation in imaginary time and in real space. We use this formulation of cubic-scaling RPA to construct a cubic-scaling algorithm using Gaussian basis functions (Sec. 5.4), while we focus on the parallel implementation in Sec. 5.5. Benchmark calculations on the accuracy and the scaling of the $O(N^3)$ RPA method are reported in Secs. 6.3 and 5.7.

5.2 Resolution-of-the-identity approximation (RI)

The following index notation has been adopted: i, j (a, b) refer to occupied (virtual) molecular orbitals (MOs) ψ; $\mu, \nu, \lambda, \sigma$ to primary Gaussian basis functions ϕ and P, Q to auxiliary Gaussian RI basis functions φ. The number of primary Gaussian basis functions is referenced as N_{prim}, the number of RI basis functions as N_{RI} and the system size as abstract symbol N, where N_{prim} and N_{RI} are both proportional to N. The spin index has been dropped for convenience.

Four-center electron repulsion integrals (4c-ERIs) are of central importance for computing the RPA correlation energy. These integrals, in Mulliken notation, are defined as

$$(\mu\nu|\lambda\sigma) := \int_{\Omega} d\mathbf{r} \int_{\mathbb{R}^3} d\mathbf{r}' \phi^{\text{P}}_{\mu}(\mathbf{r}')\phi^{\text{P}}_{\nu}(\mathbf{r}')\phi^{\text{P}}_{\lambda}(\mathbf{r})\phi^{\text{P}}_{\sigma}(\mathbf{r})v(\mathbf{r},\mathbf{r}') \tag{5.2}$$

where $v(\mathbf{r},\mathbf{r}') = 1/|\mathbf{r}-\mathbf{r}'|$ is the bare Coulomb interaction, Ω the simulation cell and the superscript P indicates that the basis functions are periodically repeated for condensed phase systems,

$$\phi^{\text{P}}_{\mu}(\mathbf{r}) = \sum_i \phi_{\mu}(\mathbf{r} - \mathbf{R}_i)\,, \tag{5.3}$$

where $\mathbf{R}_i$ are the lattice vectors and ϕ_μ is a Gaussian basis function being localized on a single atom. Within the RI approximation based on the overlap metric, the 4c-ERIs are factorized to [120]

$$(\mu\nu|\lambda\sigma)_{\text{RI}} = \sum_{PQRS} (\mu\nu P) S^{-1}_{PQ} V_{QR} S^{-1}_{RS} (S\lambda\sigma)\,. \tag{5.4}$$

Here, $\mathbf{S}$ denotes the overlap matrix in the RI basis,

$$S_{PQ} = \int_{\mathbb{R}^3} d\mathbf{r}\; \varphi^{\text{P}}_P(\mathbf{r})\varphi_Q(\mathbf{r})\,, \tag{5.5}$$

and $\mathbf{V}$ the Coulomb matrix in the RI basis,

$$V_{PQ} = \int_{\Omega} d\mathbf{r} \int_{\mathbb{R}^3} d\mathbf{r}'\, \varphi^{\text{P}}_P(\mathbf{r})\varphi^{\text{P}}_Q(\mathbf{r}')v(\mathbf{r},\mathbf{r}')\,. \tag{5.6}$$

In practice, the Coulomb integrals V_{PQ} are calculated by Ewald summation [196],

$$V_{PQ} = \frac{4\pi}{V} \sum_{\mathbf{G}\neq\mathbf{0}} \frac{\varphi_P(\mathbf{G})\,\varphi_Q(-\mathbf{G})}{|\mathbf{G}|^2} \,. \tag{5.7}$$

The three-center overlap integrals $(\mu\nu P)$ are given by

$$(\mu\nu P) = \int_{\mathbb{R}^3} d\mathbf{r}\, \phi^{\mathrm{P}}_{\mu}(\mathbf{r})\phi^{\mathrm{P}}_{\nu}(\mathbf{r})\varphi_P(\mathbf{r}) \,. \tag{5.8}$$

We compute the two- and three-center overlap integrals from Eqs. (5.5) and (5.8) employing the Obara-Saika recurrence scheme [257]. In the periodic case, neighboring cells have to be considered for the Obara-Saika scheme as long as the overlap of Gaussians from the unit cell and the replica are non-vanishing.

Since the Coulomb matrix $\mathbf{V}$ is positive definite, its Cholesky decomposition can be computed as

$$V_{PQ} = \sum_R L_{PR} L^{\mathrm{T}}_{RQ} \,. \tag{5.9}$$

In this way, the RI factorization from Eq. (5.4) can be expressed in a compact form as

$$(\mu\nu|\lambda\sigma)_{\mathrm{RI}} = \sum_P B^{\mu\nu}_P B^{\lambda\sigma}_P \,, \tag{5.10}$$

where $\mathbf{B}$ is given by

$$B^{\mu\nu}_P = \sum_{QR} (\mu\nu Q) S^{-1}_{QR} L_{RP} \,. \tag{5.11}$$

We define the $N_{\mathrm{RI}} \times N_{\mathrm{RI}}$ matrix $\mathbf{K}$,

$$\mathbf{K} = \mathbf{S}^{-1}\mathbf{L} \,, \tag{5.12}$$

and Eq. (5.11) simplifies to

$$B^{\mu\nu}_P = \sum_Q (\mu\nu Q) K_{QP} \,. \tag{5.13}$$

If required, we transform $B^{\mu\nu}_P$ from pairs $\mu\nu$ of Gaussian basis functions to occupied-virtual pairs ia employing the MO coefficients $C_{\mu n}$:

$$B^{ia}_P = \sum_{\mu\nu} C_{\mu i} C_{\nu a} B^{\mu\nu}_P \,. \tag{5.14}$$

5.3 Cubic-scaling RPA with real-space density response

The correlation energy in the random phase approximation can be computed as [123,213,248,258]

$$E^{\mathrm{RPA}}_{\mathrm{c}} = \frac{1}{2\pi} \int_0^\infty d\omega\, \mathrm{Tr}\left[\ln\left(1 - \chi(i\omega)v\right) + \chi(i\omega)v\right] \tag{5.15}$$

where $v(\mathbf{r},\mathbf{r}') = 1/|\mathbf{r}-\mathbf{r}'|$ is the bare Coulomb interaction and $\chi(\mathbf{r},\mathbf{r}',i\omega)$ the density response in imaginary frequency:

$$\chi(\mathbf{r},\mathbf{r}',i\omega) = 2\sum_{i}^{\text{occ}}\sum_{a}^{\text{virt}} \psi_a(\mathbf{r}')\psi_i(\mathbf{r}')\psi_i(\mathbf{r})\psi_a(\mathbf{r}) \frac{\varepsilon_i-\varepsilon_a}{\omega^2+(\varepsilon_i-\varepsilon_a)^2}\,. \tag{5.16}$$

The drawback of employing Eq. (5.16) to compute the density response function is the $O(N^4)$ computational cost (N: system size) since the number of occupied and virtual orbitals and the space coordinates $\mathbf{r}$ and $\mathbf{r}'$ are each growing linearly with N. In contrast, the computation of the density response in imaginary time, [24, 248]

$$\chi(\mathbf{r},\mathbf{r}',i\tau) = \sum_{i}^{\text{occ}} \psi_i(\mathbf{r}')\psi_i(\mathbf{r})e^{-|(\varepsilon_i-\varepsilon_\text{F})\tau|} \sum_{a}^{\text{virt}} \psi_a(\mathbf{r}')\psi_a(\mathbf{r})e^{-|(\varepsilon_a-\varepsilon_\text{F})\tau|}\,, \tag{5.17}$$

only requires $O(N^3)$ operations since the summation over occupied and virtual orbitals are decoupled and can be executed separately. ε_F in Eq. (5.17) refers to the Fermi energy.

The density response is symmetric in time and frequency, $\chi(\mathbf{r},\mathbf{r}',i\omega) = \chi(\mathbf{r},\mathbf{r}',-i\omega)$ and $\chi(\mathbf{r},\mathbf{r}',i\tau) = \chi(\mathbf{r},\mathbf{r}',-i\tau)$. As a consequence, the Fourier transforms from imaginary frequency to imaginary time and vice versa simplify to a cosine transformation [248]:

$$\chi(\mathbf{r},\mathbf{r}',i\omega) = 2\int_0^\infty d\tau\,\chi(\mathbf{r},\mathbf{r}',i\tau)\cos(\tau\omega)\,, \qquad \chi(\mathbf{r},\mathbf{r}',i\tau) = \frac{1}{\pi}\int_0^\infty d\omega\,\chi(\mathbf{r},\mathbf{r}',i\omega)\cos(\tau\omega)\,. \tag{5.18}$$

Despite the simplicity of this formulation, the size of the real space coordinate $\mathbf{r}$ is of the same order as the size of a plane-wave basis [248] and thus can easily exceed millions of elements even for a relatively small cell. One of the reasons of reformulating these equations in a Gaussian basis is to reduce the size of the density response matrix without significant loss of accuracy.

5.4 Cubic-scaling RPA in a Gaussian basis

Quartic-scaling RPA in a Gaussian basis

Eshuis *et al.* [123] applied the RI [Eq. (5.10)] to Eq. (5.15) and obtained

$$E_\text{c}^\text{RPA} = \frac{1}{2\pi}\int_0^\infty d\omega\ \text{Tr}\left[\ln(\mathbf{1}+\mathbf{Q}(\omega)) - \mathbf{Q}(\omega)\right] \tag{5.19}$$

where $\mathbf{Q}(\omega)$ is a matrix of size $N_\text{RI}\times N_\text{RI}$ and is given by

$$Q_{PQ}(\omega) = 2\sum_{i}^{\text{occ}}\sum_{a}^{\text{virt}} B_P^{ia}\frac{\varepsilon_a-\varepsilon_i}{\omega^2+(\varepsilon_a-\varepsilon_i)^2}B_Q^{ia}\,, \tag{5.20}$$

where B_P^{ia} is defined in Eq. (5.14). In the $O(N^3)$ implementation, we do not compute $\mathbf{Q}(\omega)$ by means of Eq. (5.20) due to the $O(N^4)$ computational cost. Instead, we compute $\mathbf{Q}(\tau)$ as presented in the following and we obtain $\mathbf{Q}(\omega)$ by the cosine transform adapted from Eq. (5.18):

$$Q_{PQ}(\omega) = 2\int_0^\infty d\tau\ Q_{PQ}(\tau)\cos(\tau\omega)\,. \tag{5.21}$$

We obtain a representation for $\mathbf{Q}(\tau)$ by comparing Eqs. (5.16), (5.17) and (5.20):

$$Q_{PQ}(\tau) = \sum_{i}^{\text{occ}}\sum_{a}^{\text{virt}} B_P^{ia}\,e^{-|(\varepsilon_i-\varepsilon_\text{F})\tau|}e^{-|(\varepsilon_a-\varepsilon_\text{F})\tau|}\,B_Q^{ia}\,. \tag{5.22}$$

The computation of $\mathbf{Q}(\tau)$ according to Eq. (5.22) still scales as $O(N^4)$.

Cubic-scaling reformulation of RPA in the Gaussian basis

To arrive at a $O(N^3)$ scaling algorithm, we transform B_P^{ia} in Eq. (5.22) from occupied-virtual pairs ia to pairs $\mu\nu$ of primary basis functions:

$$B_P^{ia} = \sum_{\mu\nu} B_P^{\mu\nu} C_{\mu i} C_{\nu a} \,, \tag{5.23}$$

where we used the MO coefficients $C_{\mu n}$ being defined as $\psi_n(\mathbf{r}) = \sum_\mu C_{\mu n}\phi_\mu(\mathbf{r})$. By inserting Eq. (5.23) into Eq. (5.22), we separate the summation over occupied and virtual states which is the key for the $O(N^3)$ implementation:

$$Q_{PQ}(\tau) = \sum_{\mu\nu\lambda\sigma} B_P^{\mu\nu} B_Q^{\lambda\sigma} \sum_i^{\text{occ}} C_{\mu i} C_{\lambda i} e^{-|(\varepsilon_i - \varepsilon_\text{F})\tau|} \sum_a^{\text{virt}} C_{\nu a} C_{\sigma a} e^{-|(\varepsilon_a - \varepsilon_\text{F})\tau|} \,. \tag{5.24}$$

We introduce the pseudo-density matrices [259–261] $D_{\mu\lambda}^{\text{occ}}(\tau)$ and $D_{\nu\sigma}^{\text{virt}}(\tau)$ which are computed in $O(N^3)$ operations as

$$D_{\mu\lambda}^{\text{occ}}(\tau) = \sum_i^{\text{occ}} C_{\mu i} C_{\lambda i} e^{-|(\varepsilon_i - \varepsilon_\text{F})\tau|} \,, \quad D_{\nu\sigma}^{\text{virt}}(\tau) = \sum_a^{\text{virt}} C_{\nu a} C_{\sigma a} e^{-|(\varepsilon_a - \varepsilon_\text{F})\tau|} \,. \tag{5.25}$$

Inserting the definitions of $D_{\mu\lambda}^{\text{occ}}$ and $D_{\nu\sigma}^{\text{virt}}$ [Eq. (5.25)] and the definition of $B_P^{\mu\nu}$ from Eq. (5.13) into Eq. (5.24), we obtain

$$Q_{PQ}(\tau) = \sum_R K_{RP} \sum_T K_{TQ} \sum_{\mu\sigma} \left[\sum_\lambda (\lambda\sigma R) D_{\mu\lambda}^{\text{occ}}(\tau) \right] \left[\sum_\nu (\mu\nu T) D_{\nu\sigma}^{\text{virt}}(\tau) \right] . \tag{5.26}$$

We introduce the three-index tensors $M_{\mu\sigma R}^{\text{occ}}(\tau)$ and $M_{\mu\sigma T}^{\text{virt}}(\tau)$:

$$M_{\mu\sigma R}^{\text{occ}}(\tau) = \sum_\lambda (\lambda\sigma R) D_{\mu\lambda}^{\text{occ}}(\tau) \,, \quad M_{\mu\sigma T}^{\text{virt}}(\tau) = \sum_\nu (\mu\nu T) D_{\nu\sigma}^{\text{virt}}(\tau) \,. \tag{5.27}$$

Both tensors $M_{\mu\sigma R}^{\text{occ}}$ and $M_{\mu\sigma T}^{\text{virt}}$ are computed from Eq. (5.27) in $O(N^2)$ operations and in $O(N)$ operations once the scaled density matrices from Eq. (5.25) are getting sparse [261] for non-metallic systems being very large in at least one dimension. The reason for the low-scaling behavior $O(N^2)/O(N)$ is that the three-center overlap $(\mu\nu T)$ of localized basis functions μ, ν and T is sparse in μ/ν, μ/T and ν/T. [254, 255] Inserting the definitions of $M_{\mu\sigma R}^{\text{occ}}$ and $M_{\mu\sigma T}^{\text{virt}}$ in Eq. (5.26) yields

$$Q_{PQ}(\tau) = \sum_R K_{RP} \sum_T K_{TQ} \sum_{\mu\sigma} M_{\mu\sigma R}^{\text{occ}}(\tau) M_{\mu\sigma T}^{\text{virt}}(\tau) \,. \tag{5.28}$$

We introduce the $N_\text{RI} \times N_\text{RI}$ matrix $\mathbf{P}(\tau)$ with elements

$$P_{RT}(\tau) = \sum_{\mu\sigma} M_{\mu\sigma R}^{\text{occ}}(\tau) M_{\mu\sigma T}^{\text{virt}}(\tau) \,. \tag{5.29}$$

According to the definition of $M_{\mu\sigma R}^{\text{occ}}$ and $M_{\mu\sigma T}^{\text{virt}}$ in Eq. (5.27), $M_{\mu\sigma R}^{\text{occ}}$ is sparse in σ/R and $M_{\mu\sigma T}^{\text{virt}}$ is sparse in μ/T and we conclude that the computation of $\mathbf{P}(\tau)$ in Eq. (5.29) only requires $O(N^2)$ operations and, once the scaled density matrices from Eq. (5.25) are getting sparse, only $O(N)$ operations . By inserting Eq. (5.29) into Eq. (5.28), we finally obtain the working expression

$$\mathbf{Q}(\tau) = \mathbf{K}^\text{T} \mathbf{P}(\tau) \mathbf{K} \,. \tag{5.30}$$

The computational complexity of Eq. (5.30) is growing cubically, $O(N^3)$. Moreover, all previous steps, Eq. (5.25), (5.27) and (5.29), are at most of $O(N^3)$ computational cost or in case sparse matrix-matrix multiplication is employed [Eq. (5.27) and (5.29)], of $O(N^2)$ computational cost.

Minimax time and frequency grid

For the cosine transform of $\mathbf{Q}$ from τ to ω in Eq. (5.21) and for the subsequent frequency integration to obtain the RPA correlation energy according to Eq. (5.19), we rely on a time and a frequency grid: In a first step, we compute $Q_{PQ}(\tau_j)$ for a time grid $\{\tau_j\}_{j=1}^{M}$ according to Eq. (5.30), where M is the number of grid points which is independent of the system size. Then, $Q_{PQ}(\omega_k)$ is obtained for a frequency set $\{\omega_k\}_{k=1}^{M}$ by the cosine transform according to Eq. (5.21):

$$Q_{PQ}(\omega_k) = 2\sum_{j=1}^{M} \lambda_{kj} Q_{PQ}(\tau_j)\cos(\tau_j\omega_k)\,, \tag{5.31}$$

where λ_{kj} are the integration weights. The RPA correlation energy is computed by numerically integrating Eq. (5.19):

$$E_{\mathrm{c}}^{\mathrm{RPA}} = \frac{1}{2\pi}\sum_{k=1}^{M} \sigma_k \left[\ln[\det(\mathbf{1}+\mathbf{Q}(\omega_k))] - \mathrm{Tr}(\mathbf{Q}(\omega_k))\right]\,, \tag{5.32}$$

where the identity $\mathrm{Tr}[\ln(\mathbf{A})] = \ln[\det(\mathbf{A})]$ has been used which holds for any positive-definite matrix $\mathbf{A}$. [76] We follow the work of Kaltak *et al.* [248] and employ minimax quadratures [262,263] to reduce the number of integration nodes M to $10-20$. Practically, we employ the pretabulated minimax parameters $\{\omega_k\}$, $\{\sigma_k\}$ and $\{\tau_j\}$ from Ref. [76] which have been created for imaginary-frequency RPA calculations and for Laplace scaled-opposite-spin second-order Møller-Plesset perturbation theory. The integration weights λ_{kj} are computed by a least-square optimization using singular value decomposition [248].

The outline of the cubic-scaling RPA correlation energy algorithm is summarized in Fig. 5.1.

5.5 Parallel implementation

The pseudocode for the parallel implementation of the cubic-scaling RPA algorithm is presented in Fig. 5.2. In the following section, we discuss this figure in detail.

General strategy for the parallel implementation

For the parallelization, we are guided by three strategies: First, the three-index tensors $(\mu\nu P)$, $M^{\mathrm{occ}}_{\mu\sigma R}(\tau)$ and $M^{\mathrm{virt}}_{\mu\sigma T}(\tau)$ (as defined Fig. 5.1) are not replicated due to the huge amount of memory needed for these tensors. Second, all two-index matrices as $D^{\mathrm{occ}}_{\mu\lambda}(\tau)$, $D^{\mathrm{virt}}_{\nu\sigma}(\tau)$ and $P_{RT}(\tau)$ (as defined Fig. 5.1) are replicated into small subgroups. Third, all sparse matrix-matrix multiplications are carried out in these small subgroups in order to reduce the communication needed for the sparse matrix-matrix multiplications.

Parallel matrix-tensor operations

We define two different MPI subgroups p and q. Every p group hosts a range $[P^p_{\mathrm{start}}, P^p_{\mathrm{end}}]$ of RI basis functions. After computing the scaled density matrices $D^{\mathrm{occ}}_{\mu\lambda}(\tau)$ and $D^{\mathrm{virt}}_{\nu\sigma}(\tau)$ employing all processes and the dense linear algebra library ScaLAPACK, $D^{\mathrm{occ}}_{\mu\lambda}(\tau)$ and $D^{\mathrm{virt}}_{\nu\sigma}(\tau)$ are replicated to every p group. Then, the multiplication of $D^{\mathrm{occ}}_{\mu\lambda}(\tau)$ and $D^{\mathrm{virt}}_{\nu\sigma}(\tau)$ with the three-center overlap integrals $(\mu\nu P)$ [Eq. (5.27)] is carried out by DBCSR [129] locally in the p group for $P \in [P^p_{\mathrm{start}}, P^p_{\mathrm{end}}]$

Compute $S_{PQ} = \int d\mathbf{r}\, \varphi_P(\mathbf{r})\varphi_Q(\mathbf{r})$ $\quad \mathcal{O}(N^1)$

Compute $V_{PQ} = \int d\mathbf{r}\, d\mathbf{r}' \varphi_P(\mathbf{r})\varphi_Q(\mathbf{r}')|\mathbf{r} - \mathbf{r}'|^{-1}$ $\quad \mathcal{O}(N^2)$

Factorize V_{PQ} by Cholesky decomposition: $V_{PQ} = \sum_R L_{PR} L_{RQ}^{\mathrm{T}}$ $\quad \mathcal{O}(N^3)$

Invert S_{PQ} with use of Cholesky decomposition $\quad \mathcal{O}(N^3)$

Obtain K_{PQ} by matrix-matrix multiplication: $K_{PQ} = \sum_R S_{PR}^{-1} L_{QR}$ $\quad \mathcal{O}(N^3)$

Compute $(\mu\nu P) = \int d\mathbf{r}\, \phi_\mu(\mathbf{r})\phi_\nu(\mathbf{r})\varphi_P(\mathbf{r})$ $\quad \mathcal{O}(N^1)$

Set up the minimax grids $\{\omega_k\}_{k=1}^M$, $\{\tau_j\}_{j=1}^M$, $\{\lambda_{kj}\}_{k,j=1}^M$ and $\{\sigma_k\}_{k=1}^M$

Get input: MO coefficients $C_{\mu n}$ and eigenvalues ε_n of MOs from SCF

Set $Q_{PQ}(\omega_k) = 0$ for all $\omega_k = \omega_1, \omega_2, \ldots, \omega_M$

Do $\tau_j = \tau_1, \tau_2, \ldots, \tau_M$

$D_{\mu\lambda}^{\mathrm{occ}}(\tau_j) = \sum_i^{\mathrm{occ}} C_{\mu i} C_{\lambda i} e^{-|(\varepsilon_i - \varepsilon_\mathrm{F})\tau_j|}$ $\quad \mathcal{O}(MN^3)$

$D_{\nu\sigma}^{\mathrm{virt}}(\tau_j) = \sum_a^{\mathrm{virt}} C_{\nu a} C_{\sigma a} e^{-|(\varepsilon_a - \varepsilon_\mathrm{F})\tau_j|}$ $\quad \mathcal{O}(MN^3)$

$M_{\mu\sigma R}^{\mathrm{occ}}(\tau_j) = \sum_\lambda (\lambda\sigma R) D_{\mu\lambda}^{\mathrm{occ}}(\tau_j)$ $\quad \mathcal{O}(MN^2)$

$M_{\mu\sigma T}^{\mathrm{virt}}(\tau_j) = \sum_\nu (\mu\nu T) D_{\nu\sigma}^{\mathrm{virt}}(\tau_j)$ $\quad \mathcal{O}(MN^2)$

$P_{RT}(\tau_j) = \sum_{\mu\sigma} M_{\mu\sigma R}^{\mathrm{occ}}(\tau_j) M_{\mu\sigma T}^{\mathrm{virt}}(\tau_j)$ $\quad \mathcal{O}(MN^2)$

$Q_{PQ}(\tau_j) = \sum_R K_{RP} \sum_T K_{TQ} P_{RT}(\tau_j)$ $\quad \mathcal{O}(MN^3)$

Do $\omega_k = \omega_1, \omega_2, \ldots, \omega_M$

Fourier transform from τ to ω:

$Q_{PQ}(\omega_k) = Q_{PQ}(\omega_k) + 2\lambda_{kj} Q_{PQ}(\tau_j) \cos(\tau_j \omega_k)$ $\quad \mathcal{O}(M^2N^2)$

End do ω_k

End do τ_j

Set $E_\mathrm{c}^{\mathrm{RPA}} = 0$

Do $\omega_k = \omega_1, \omega_2, \ldots, \omega_M$

Update $E_\mathrm{c}^{\mathrm{RPA}} = E_\mathrm{c}^{\mathrm{RPA}} + \sigma_k \left[\ln[\det(\mathbf{1} + \mathbf{Q}(\omega_k))] - \mathrm{Tr}(\mathbf{Q}(\omega_k))\right]$ $\quad \mathcal{O}(MN^3)$

End do ω_k

Figure 5.1: Pseudocode and associated computational cost (N: system size, M: number of time and frequency points, respectively) of the algorithm to compute the RPA correlation energy in $\mathcal{O}(N^3)$ operations. $\mu, \nu, \lambda, \sigma$ refer to primary Gaussian basis functions, P, Q, R, T to auxiliary Gaussians, a to virtual molecular orbitals (MOs), i to occupied and n to general ones.

Compute $\mathbf{S}^{-1}$ and Cholesky decomposition $\mathbf{L}$ of $\mathbf{V}$ (ScaLAPACK)
Compute and store $\mathbf{K} = \mathbf{S}^{-1}\mathbf{L}$ (ScaLAPACK)

Assign each process a group p
Create ranges $[P^p_{\text{start}}, P^p_{\text{end}}]$ for RI basis functions
Allocate single DBCSR matrix $\mathbf{S}^p$ in the p group (elements $S^p_{\mu(\sigma P)}$, row index μ, combined column index σP for $P \in [P^p_{\text{start}}, P^p_{\text{end}}]$ and all μ, σ; blocks as overlap matrix $\mathbf{S}$, column block sizes scaled by $P^p_{\text{end}} - P^p_{\text{start}} + 1$)
Compute and store $S^p_{\mu(\sigma P)} = (\mu\sigma P)$ for all μ, σ and $P \in [P^p_{\text{start}}, P^p_{\text{end}}]$
Allocate $\mathbf{M}^{\text{occ},p}$ and $\mathbf{M}^{\text{virt},p}$ as copy of $\mathbf{S}^p$

Assign each process a second group q
Create ranges $[\mu^q_{\text{start}}, \mu^q_{\text{end}}]$ and $[\sigma^q_{\text{start}}, \sigma^q_{\text{end}}]$ for primary basis functions
Allocate DBCSR matrices $\mathbf{M}^{\text{occ/virt},q}$ in the q group (elements $M^{\text{occ/virt},q}_{(\mu\sigma)Q}$, combined row index $(\mu\sigma)$, column index Q for all Q and $\mu \in [\mu^q_{\text{start}}, \mu^q_{\text{end}}]$, $\sigma \in [\sigma^q_{\text{start}}, \sigma^q_{\text{end}}]$; single block for $(\mu\sigma)$ index, atom blocks for Q)

Do $\tau_j = \tau_1, \tau_2, \ldots, \tau_M$

$\tilde{C}^{\text{occ}}_{\mu i}(\tau_j) = C_{\mu i} e^{-|(\varepsilon_i - \varepsilon_{\text{F}})\tau_j|/2}$, i: occupied orbital

$\tilde{C}^{\text{virt}}_{\mu a}(\tau_j) = C_{\mu a} e^{-|(\varepsilon_a - \varepsilon_{\text{F}})\tau_j|/2}$, a: virtual orbital

$\mathbf{D}^{\text{occ}}(\tau_j) = [\tilde{\mathbf{C}}^{\text{occ}})(\tau_j)]^{\text{T}} \tilde{\mathbf{C}}^{\text{occ}}(\tau_j)$ (ScaLAPACK)

$\mathbf{D}^{\text{virt}}(\tau_j) = [\tilde{\mathbf{C}}^{\text{virt}})(\tau_j)]^{\text{T}} \tilde{\mathbf{C}}^{\text{virt}}(\tau_j)$ (ScaLAPACK)

Replicate $\mathbf{D}^{\text{occ}}(\tau_j)$ and $\mathbf{D}^{\text{virt}}(\tau_j)$ to every group p and store them in a DBCSR matrix (atom blocks for rows and columns, respectively)

$\mathbf{M}^{\text{occ},p}(\tau_j) = \mathbf{D}^{\text{occ}}(\tau_j)\mathbf{S}^p$ (DBCSR, locally in p group)

$\mathbf{M}^{\text{virt},p}(\tau_j) = \mathbf{D}^{\text{virt}}(\tau_j)\mathbf{S}^p$ (DBCSR, locally in p group)

Reorder data from p groups to q groups: $\mathbf{M}^{\text{occ/virt},p}(\tau_j)$ to $\mathbf{M}^{\text{occ/virt},q}(\tau_j)$

$\mathbf{P}^q(\tau_j) = [\mathbf{M}^{\text{occ},q}(\tau_j)]^{\text{T}} \mathbf{M}^{\text{virt},q}(\tau_j)$ (DBCSR, locally in q group)

Sum up $\mathbf{P}^q(\tau_j)$ from every q group, fill it into $\mathbf{P}(\tau_j) = \sum_q \mathbf{P}^q(\tau_j)$ and spread $\mathbf{P}(\tau_j)$ to all processes

$\mathbf{Q}(\tau_j) = \mathbf{K}^{\text{T}} \mathbf{P}(\tau_j) \mathbf{K}$ (ScaLAPACK)

Do $\omega_k = \omega_1, \omega_2, \ldots, \omega_M$: Fourier $\tau \rightarrow \omega$: $\mathbf{Q}(\omega_k) = \mathbf{Q}(\omega_k) + 2\lambda_{kj}\mathbf{Q}(\tau_j)\cos(\tau_j\omega_k)$

End do τ_j

Set $E^{\text{PPA}}_{\text{c}} = 0$

Do $\omega_k = \omega_1, \omega_2, \ldots, \omega_M$: $E^{\text{PPA}}_{\text{c}} = E^{\text{PPA}}_{\text{c}} + \sigma_k[\ln[\det(\mathbf{1} + \mathbf{Q}(\omega_k))] - \text{Tr}(\mathbf{Q}(\omega_k))]$ (ScaLAPACK)

Figure 5.2: Parallel implementation of the algorithm to compute the RPA correlation energy in $O(N^3)$ operations. Some matrices and their indices have already been defined in Fig. 5.1. As dense linear algebra library, we employ ScaLAPACK. All calls to ScaLAPACK are executed employing all processes.

and $\mu, \sigma \in [1, N_{\text{prim}}]$:

$$M^{\text{occ},p}_{\mu\sigma P}(\tau) = \sum_{\lambda=1}^{N_{\text{prim}}} (\lambda\sigma P) D^{\text{occ}}_{\mu\lambda}(\tau)\,, \qquad M^{\text{virt},p}_{\mu\sigma P}(\tau) = \sum_{\lambda=1}^{N_{\text{prim}}} (\sigma\lambda P) D^{\text{virt}}_{\mu\lambda}(\tau)\,, \tag{5.33}$$

where N_{prim} is the number of primary basis functions.

After completing the computation from Eq. (5.33), we redistribute $M^{\text{occ}}_{\mu\sigma R}(\tau)$ and $M^{\text{virt}}_{\mu\sigma T}(\tau)$ from p groups to q groups: The subgroup q is defined by cutting the index pair $\mu\sigma$ of $M^{\text{occ}}_{\mu\sigma R}(\tau)$ and $M^{\text{virt}}_{\mu\sigma T}(\tau)$ into ranges $[\mu^q_{\text{start}}, \mu^q_{\text{end}}]$ and $[\sigma^q_{\text{start}}, \sigma^q_{\text{end}}]$ covering all primary basis functions:

$$\bigcup_{q=1}^{N_q} [\mu^q_{\text{start}}, \mu^q_{\text{end}}] \times [\sigma^q_{\text{start}}, \sigma^q_{\text{end}}] = [1, N_{\text{prim}}] \times [1, N_{\text{prim}}]\,, \tag{5.34}$$

where N_q is the number of q groups. A q group hosts $M^{\text{occ}}_{\mu\sigma R}(\tau)$ and $M^{\text{virt}}_{\mu\sigma T}(\tau)$ for $\mu \in [\mu^q_{\text{start}}, \mu^q_{\text{end}}]$, $\sigma \in [\sigma^q_{\text{start}}, \sigma^q_{\text{end}}]$ and all RI basis functions R, T. Each of $M^{\text{occ}}_{\mu\sigma R}(\tau)$ and $M^{\text{virt}}_{\mu\sigma T}(\tau)$ is stored in the q group in a single DBCSR matrix with a single row block consisting of a combined $(\mu\sigma)$ index and atom blocks for the RI index R and T, respectively. The ranges $[\mu^q_{\text{start}}, \mu^q_{\text{end}}]$ and $[\sigma^q_{\text{start}}, \sigma^q_{\text{end}}]$ are chosen such that all $\mu \in [\mu^q_{\text{start}}, \mu^q_{\text{end}}]$ and all $\sigma \in [\sigma^q_{\text{start}}, \sigma^q_{\text{end}}]$ belong to neighboring atoms, respectively. Then, $M^{\text{occ}}_{\mu\sigma R}(\tau)$ and $M^{\text{virt}}_{\mu\sigma T}(\tau)$ in the q group are sparse in the combined row index $(\mu\sigma)$ and the column index R/T. The DBCSR matrix $P_{RT}(\tau)$ is replicated in the q group and the operation from Eq. (5.29) is carried out locally in the q group for the given ranges $[\mu^q_{\text{start}}, \mu^q_{\text{end}}]$ and $[\sigma^q_{\text{start}}, \sigma^q_{\text{end}}]$ and all R, T:

$$P^q_{RT}(\tau) = \sum_{\mu=\mu^q_{\text{start}}}^{\mu^q_{\text{end}}} \sum_{\sigma=\sigma^q_{\text{start}}}^{\sigma^q_{\text{end}}} M^{\text{occ},q}_{\mu\sigma R}(\tau) M^{\text{virt},q}_{\mu\sigma T}(\tau)\,. \tag{5.35}$$

Then, all q-local DBCSR matrices $P^q_{RT}(\tau)$ are summed up to obtain the full $P_{RT}(\tau)$ matrix:

$$P_{RT}(\tau) = \sum_{q=1}^{N_q} P^q_{RT}(\tau)\,. \tag{5.36}$$

The p and q groups are chosen such that they are as small as possible to minimize the communication for the sparse matrix-matrix multiplication. On the other hand, p and q groups have to be as large as necessary not to run out of memory since the replicated matrices $D^{\text{occ}}_{\mu\lambda}(\tau)$, $D^{\text{virt}}_{\nu\sigma}(\tau)$ and $P_{RT}(\tau)$ can require a large amount of memory.

The matrix operation $\mathbf{Q}(\tau) = \mathbf{K}^{\mathrm{T}}\mathbf{P}(\tau)\mathbf{K}$ is carried out using full matrices, all processes and ScaLAPACK. We compute the determinant and the trace of $\mathbf{Q}(\omega)$ to arrive at the RPA correlation energy as in Ref. [76], see Fig. 5.2.

Memory reduction by an iterative scheme

The memory needed for $M^{\text{occ}}_{\mu\sigma R}(\tau)$ and $M^{\text{virt}}_{\mu\sigma T}(\tau)$ can be reduced by an additional loop over $\mu\sigma$ blocks (not sketched in Fig. 5.2): We break the ranges $[\mu^q_{\text{start}}, \mu^q_{\text{end}}]$ and $[\sigma^q_{\text{start}}, \sigma^q_{\text{end}}]$ of every q group again in N_{cut} batches $[\mu^{q,s}_{\text{start}}, \mu^{q,s}_{\text{end}}]$ and $[\sigma^{q,s}_{\text{start}}, \sigma^{q,s}_{\text{end}}]$ with

$$\bigcup_{s=1}^{N_{\text{cut}}} [\mu^{q,s}_{\text{start}}, \mu^{q,s}_{\text{end}}] \times [\sigma^{q,s}_{\text{start}}, \sigma^{q,s}_{\text{end}}] = [\mu^q_{\text{start}}, \mu^q_{\text{end}}] \times [\sigma^q_{\text{start}}, \sigma^q_{\text{end}}]\,. \tag{5.37}$$

Then, $M^{\text{occ}}_{\mu\sigma R}(\tau)$ and $M^{\text{virt}}_{\mu\sigma T}(\tau)$ are computed from Eq. (5.33) for $\mu \in [\mu^{q,s}_{\text{start}}, \mu^{q,s}_{\text{end}}]$ and $\sigma \in [\sigma^{q,s}_{\text{start}}, \sigma^{q,s}_{\text{end}}]$ which reduces the memory of $M^{\text{occ}}_{\mu\sigma R}(\tau)$ and $M^{\text{virt}}_{\mu\sigma T}(\tau)$ by a factor N_{cut}. Subsequently, $M^{\text{occ}}_{\mu\sigma R}(\tau)$ and $M^{\text{virt}}_{\mu\sigma T}(\tau)$ are contracted [Eqs. (5.29) and (5.35)],

$$P^{q,s}_{RT}(\tau) = \sum_{\mu=\mu^{q,s}_{\text{start}}}^{\mu^{q,s}_{\text{end}}} \sum_{\sigma=\sigma^{q,s}_{\text{start}}}^{\sigma^{q,s}_{\text{end}}} M^{\text{occ},q,s}_{\mu\sigma R}(\tau) M^{\text{virt},q,s}_{\mu\sigma T}(\tau) \tag{5.38}$$

and the memory of $M^{\text{occ},q,s}_{\mu\sigma R}(\tau)$ and $M^{\text{virt},q,s}_{\mu\sigma T}(\tau)$ is freed. We obtain $P^{s}_{RT}(\tau)$ for a batch s by summing up from the q groups, and $P_{RT}(\tau)$ is computed by the loop over the s batches:

$$P^{s}_{RT}(\tau) = \sum_{q=1}^{N_q} P^{q,s}_{RT}(\tau)\,, \qquad P_{RT}(\tau) = \sum_{s=1}^{N_{\text{cut}}} P^{s}_{RT}(\tau)\,. \tag{5.39}$$

As already mentioned, we obtain a memory reduction for $M^{\text{occ}}_{\mu\sigma R}(\tau)$ and $M^{\text{virt}}_{\mu\sigma T}(\tau)$ by a factor of N_{cut} by this procedure where no additional computations are necessary.

5.6 Validation

In this section, we compare the RPA correlation energy computed by the $O(N^3)$ algorithm to the RPA correlation energy computed by the canonical $O(N^4)$ algorithm [75, 76, 123]. As starting point for the RPA correlation energy calculation, we employ DFT with the PBE functional [96].

Quartic-scaling RPA with the overlap metric vs. cubic-scaling RPA with the overlap metric

We begin with a comparison of cubic-scaling RPA and quartic-scaling RPA employing the overlap metric [120] in both cases, see Table 5.1. The only difference between both algorithms is the Fourier transform from τ to ω [Eqs. (5.21) and (5.31)] which is needed for the cubic-scaling RPA algorithm and absent in the quartic-scaling RPA algorithm. The minimax grid for the frequency integration [Eqs. (5.19) and (5.32), respectively] is identical for both cases. As it can be seen from Table 5.1, both algorithms converge quickly with the number of minimax points: An accuracy of

Table 5.1: Convergence of the RPA correlation energy of 32 water molecules in a periodic box with the number of grid points M. We use the same primary cc-TZVP basis and RI-cc-TZVP Ri-basis for two different RPA algorithms: The canonical RI-RPA algorithm by Eshuis *et al.* [123] with the overlap metric and the cubic-scaling RPA algorithm proposed in this work.

Number of grid points M	RPA correlation energy in Hartree computed with	
	$O(N^4)$ RPA (overl. metric)	$O(N^3)$ RPA (overl. metric)
8	– 13.028957756	– 13.028909098
12	– 13.028899938	– 13.028899877
16	– 13.028899834	– 13.028899834
20	– 13.028899834	– 13.028899834

Table 5.2: RPA correlation energy of 32 water molecules computed by three different algorithms. All algorithms share the same primary and RI basis (cc-TZVP and RI-cc-TZVP, respectively). The RI-cc-TZVP basis has been generated as described in Ref. [75] and [136]. For all RPA calculations, 20 quadrature points for the minimax grids have been used.

Method	E_c^{RPA} in Hartree
$O(N^4)$ RPA (im. freq., Coulomb metric)	– 13.0250
$O(N^4)$ RPA (im. freq., overlap metric)	– 13.0289
$O(N^3)$ RPA (im. time, overlap metric)	– 13.0289

ten digits is already reached for fourteen minimax points for both algorithms. This observation is in agreement with Ref. [248]. We conclude that the accuracy of the RPA correlation energy is not affected by the additional Fourier transform from time to frequency.

Quartic-scaling RPA with the Coulomb metric vs. cubic-scaling RPA with the overlap metric

As a second test, we compare the canonical RPA with the Coulomb metric to the cubic-scaling RPA with the overlap metric, see Table 5.2. These algorithms share the same primary and RI basis. As shown in Table 5.2, the cubic-scaling RPA correlation energy deviates by 71 µH from the quartic-scaling RPA correlation energy using the Coulomb metric. In contrast, the cubic-scaling RPA correlation energy agrees within an accuracy better than 10^{-3} µH with the quartic-scaling RPA correlation energy using the overlap metric, see Table 5.1. We conclude, that there is a deviation between the RPA results using the overlap metric and the RPA results using the Coulomb metric, but the deviation is small.

Effect of sparsity

Finally, we investigate the effect of filtering blocks of sparse matrices occuring in the cubic-scaling RPA algorithm, see Table 5.3: We choose the filter coefficients 10^{-8} and $3 \cdot 10^{-6}$ for the atom blocks (for details on these coefficients, see caption of the table) such that the relative accuracy of the RPA correlation energy is 0.01 % compared to the non-filtered result. We observe that the execution time is reduced by a factor three when this filter criterion is applied and we conclude, that already two third of the computations can be avoided for 32 water molecules in a cubic box. For all following scaling benchmarks, we employ the filter criteria 10^{-8} and $3 \cdot 10^{-6}$, respectively.

5.7 Benchmark calculations on the system size scaling

After validating our implementation, we turn over to investigate the scaling of the execution time with respect to the system size. As in Sec. 6.3, we use a cc-TZVP primary basis with corresponding RI basis [75, 76, 80, 136], the parameters $\varepsilon_{\text{filter prim}} = 3 \cdot 10^{-6}$, $\varepsilon_{\text{filter RI}} = 10^{-8}$ and a time and frequency grid of 15 points. For all calculations presented in this section, we employ this setting.

Table 5.3: RPA correlation energy of 32 water molecules computed by the cubic-scaling algorithm and two different filtering thresholds for removing blocks from sparse matrices. Every block belongs to basis functions of an atom pair. The filtering threshold for $N_{\mathrm{RI}}\times N_{\mathrm{RI}}$ matrices refers to filtering $\mathbf{P}(\tau)$ in Eq. (5.29). The filtering threshold for $N_{\mathrm{prim}}\times N_{\mathrm{prim}}$ matrices refers to filtering $\mathbf{D}^{\mathrm{occ}}(\tau)$, $\mathbf{D}^{\mathrm{virt}}(\tau)$ and all three-index tensors. The execution time was measured on 576 CRAY-XC40 cores. With the filtering thresholds of 10^{-8} and $3\cdot 10^{-6}$ as given in the table, the relative change of the RPA correlation energy due to the filtering is 0.01 % where the computation time is reduced by a factor of three.

Filtering threshold for blocks in a $N_{\mathrm{RI}}\times N_{\mathrm{RI}}$ matrix	Filtering threshold for blocks in a $N_{\mathrm{prim}}\times N_{\mathrm{prim}}$ matrix	$E_{\mathrm{c}}^{\mathrm{RPA}}$ in Hartree	Execution time in s
10^{-8}	$3\cdot 10^{-6}$	– 13.02970	260
no filtering	no filtering	– 13.02890	751

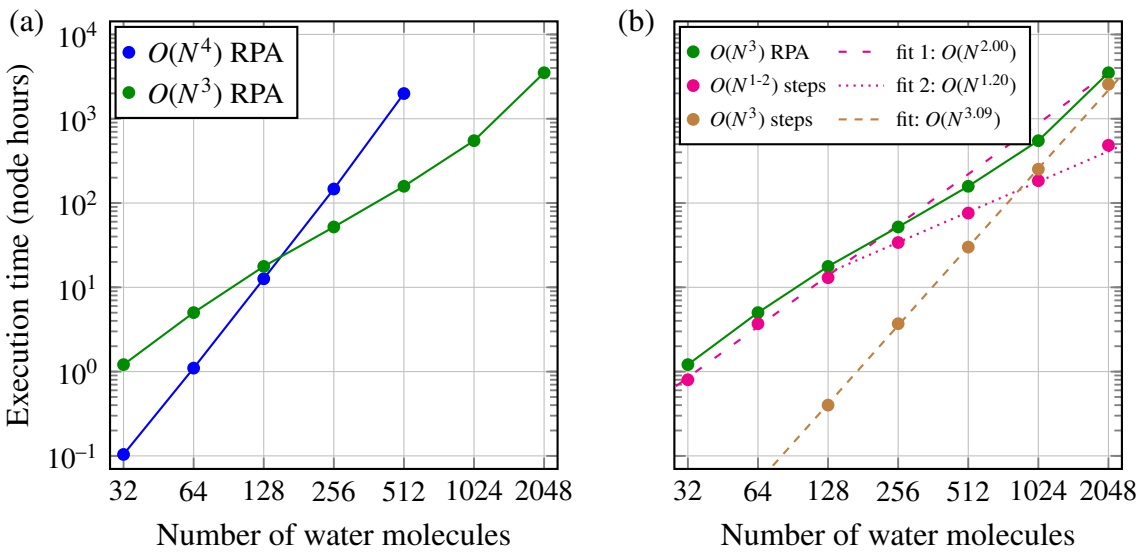

Figure 5.3: (a) Comparison of the execution time of quartic-scaling RPA (blue dots) and cubic-scaling RPA (green dots) on a CRAY XC40 machine with 36 cores per node. Both methods share the high-quality cc-TZVP basis. The basic cell contains 32 water molecules with a density of 1 g/ℓ. The larger systems consist of a $n\times 1\times 1$ supercell of the 32-water box with $n = 2, 4, 8, 16, 32$. For the largest system with 2048 water molecules (16384 electrons), 106732 primary basis functions and 278528 RI basis functions are used. For small systems, the canonical $O(N^4)$ RPA method is one order of magnitude faster than the cubic-scaling RPA. The break-even point of both methods lies between 128 and 256 water molecules. For large systems, the cubic-scaling RPA exceeds the canonical RPA in terms of the execution time. (b) Execution time and scaling of intermediate steps of the cubic-scaling RPA algorithm where the total execution time (green marks) is identical to (a). The cubic-scaling steps (brown color) and the linear- and quadratic-scaling steps (magenta) are categorized according to Fig. 5.1 and Eqs. (5.27) and (5.29). The quadratic-scaling steps dominate for small systems. Moreover, the quadratic-scaling steps turn into nearly-linear scaling steps for systems containing 256 water molecules or more since the density matrix is becoming sparse, see Fig. 5.4. The cubic-scaling steps (brown color) exhibit a small prefactor and are dominating for systems with more than 1000 water molecules.

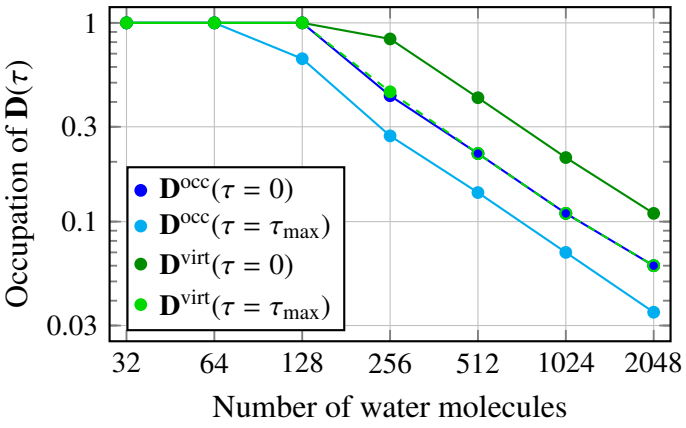

Figure 5.4: Occupation of the scaled density matrices from Eq. (5.25) with non-zero elements for the systems from Fig. 5.3. The matrix blocks correspond to atoms and are filtered with a threshold of 10^{-6} for the Frobenius norm of the block. [129] A similar occupation of scaled density matrices has been reported in Ref. [261].

Quartic- vs. cubic-scaling RPA

In Fig. 5.3 (a), we compare the execution time of $O(N^4)$- and $O(N^3)$-scaling RPA as function of the system size for water molecules in a periodic box. We observe that for 32 water molecules, the $O(N^3)$-scaling RPA algorithm [75, 76] requires ten times the execution time of the $O(N^4)$-scaling RPA algorithm. The reason is that the cubic-scaling RPA algorithm is operating in the $\mu\nu$ product basis, where μ and ν are Gaussian basis functions while the quartic-scaling RPA is implemented in the ia basis, where i is an occupied MO and a a virtual one: In a cc-TZVP basis, approximately fifteen Gaussian basis functions per occupied MO are employed which means one order of magnitude more floating point operations for cubic-scaling RPA compared to quartic-scaling RPA (without filtering). This explains that the cubic-scaling RPA algorithm is unfavorable for small systems compared to the quartic-scaling one. With increasing system size, the favorable scaling of the $O(N^3)$-RPA algorithm is appearing and the break-even point for the two algorithms is observed between 128 and 256 water molecules. Note that the break-even point is weakly dependent on the basis set size. For 512 water molecules, the cubic-scaling RPA outperforms the canonical RPA in terms of the execution time by one order of magnitude.

Analyzing the dominant steps in cubic-scaling RPA

In Fig. 5.3 (b), we break the total execution time of the cubic-scaling RPA algorithm down into cubic-scaling steps and sub-cubic-scaling steps. The cubic-scaling steps (brown color) and the linear- and quadratic-scaling steps (magenta) are categorized according to Fig. 5.1. We observe that the quadratic-scaling steps dominate for small systems which means that for small systems, the algorithm is effectively quadratic-scaling. Moreover, the quadratic-scaling steps turn into nearly-linear scaling steps for systems containing 256 water molecules or more since the density matrix is becoming sparse, see Fig. 5.4. The cubic-scaling steps exhibit a small prefactor and are dominating for systems with more than 1000 water molecules. We conclude that the bottleneck for large-scale RPA calculations is the matrix-matrix multiplication from Eq. (5.30) and the Cholesky decomposition of $\mathbf{1} + \mathbf{Q}(\omega)$ to compute the determinant in Eq. (5.32).

Truly three-dimensional calculations

In Fig. 5.3, the basic cell of 32 water molecules was repeated in one dimension, e. g. an $n\times1\times1$ supercell was employed. For low-scaling algorithms in a Gaussian basis, low-dimensional systems with large extend in one dimension are favorable since there are many pairs of Gaussian basis functions which are far away from each other and therefore have zero overlap. To test how the cubic-scaling RPA algorithm performs for truly three-dimensional systems, we show the execution

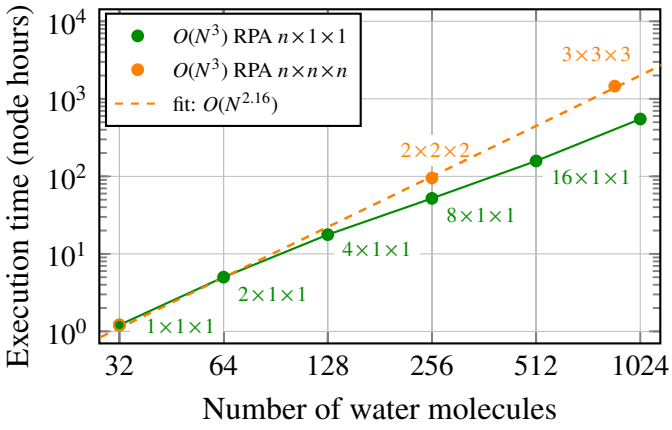

Figure 5.5: Execution time of cubic-scaling RPA for $n\times1\times1$ supercells (green, as Fig. 5.3) and $n\times n\times n$ supercells (orange) on CRAY XC40 with 36 cores per node. The execution time of cubic supercells is exceeding the one of linear supercells since the density matrix of linear cells is getting sparse, see Fig. 5.4, in contrast to the density matrix of cubic cells.

time for the cubic water supercells 2×2×2 and 3×3×3 in Fig. 5.5: We observe a scaling $O(N^{2.16})$ for the execution time from 1×1×1 to 3×3×3. As it can be seen from Fig. 5.5, the execution time of the cubic $n\times n\times n$ supercell slightly exceeds the execution time for the corresponding $n^3\times1\times1$ supercell. The reason is that the scaled density matrices are not yet sparse for the $n\times n\times n$ supercell ($n=2,3$) in contrast to the linear chain of supercells, see Fig. 5.4. We conclude that the cubic-scaling RPA algorithm from this work also scales well for systems which are extended in all three dimensions.

5.8 Conclusion and Outlook

We have presented an algorithm for computing the correlation energy in the random phase approximation (RPA) in a Gaussian basis requiring $O(N^3)$ operations and $O(N^2)$ memory. The method is a combination of several known techniques: As first technique, we employ the resolution of the identity (RI) with the overlap metric as suggested by various authors [120, 253–255]. The advantage of RI with the overlap metric compared to RI with the Coulomb metric is that the occurring three-center overlap integrals are sparse [254, 255]. To exploit the sparsity of the three-center overlap integrals, we reformulate RI-RPA in the Gaussian basis as suggested by Schurkus and Ochsenfeld [253]. Since the density response has a convenient analytic form in imaginary time, we follow Rojas *et al.* [24] to compute the density response in the RI basis in imaginary time. For the Fourier transform from imaginary time to imaginary frequency, we employ the minimax grids as proposed in the seminal work of Kaltak *et al.* [248] The final formula for computing the RPA correlation energy by an integral over imaginary frequencies was established by Eshuis *et al.* [123] No localization schemes [250] or stochastic approximations [251, 252] are needed in our algorithm.

Since the computation of the RPA correlation energy is still of high computational cost, an efficient parallelization is crucial, especially for the sparse matrix operations. For this purpose, we use the sparse linear algebra library DBCSR [129] which turns out to be highly efficient. Due to the low-scaling characteristics of the algorithm together with its efficient parallel implementation, we could apply cubic-scaling RPA up to two thousand water molecules using a cc-TZVP basis.

Our work can be seen as a prototype for a low-scaling wavefunction-based method using a global RI with the overlap metric. With the techniques presented in this work, efficient low-scaling algorithms can be designed for Hartree-Fock [264–271], Laplace-SOS-MP2 [272–278] and *GW* [20–22, 30, 248].

Chapter 6

Efficient low-scaling *GW* calculations using Gaussian basis functions

We present an algorithm [279] for computing quasiparticle levels in the *GW* approximation in a Gaussian basis requiring $O(N^3)$ operations and $O(N^2)$ memory. The method is based on the resolution of the identity with the overlap metric, a reformulation of *GW* in the Gaussian basis, imaginary time and imaginary frequency integration techniques and the use of sparse linear algebra. As application of the cubic-scaling *GW* algorithm, we present an alternative route to compute the fundamental gap of periodic, one-dimensional armchair graphene nanoribbons from *GW*: The length of non-periodic ribbons is increased until convergence of the quasiparticle levels is reached. This approach neither requires periodic boundary conditions nor Coulomb cutoff techniques and opens the way for the high-accuracy computation of fundamental gaps of periodic low-dimensional materials from *GW*. The largest graphene nanoribbon we could adress with the cubic-scaling *GW* algorithm contains 1734 atoms which demonstrates the possibility to apply *GW* to large systems.

6.1 Introduction

For computing the fundamental gap of a material with high accuracy, *GW* [9] is one of the most established methods at present involving $O(N^4)$ computational cost in a canonical implementation where N is the system size. *GW* is a method originating from many-body perturbation theory [9] and was first applied to real materials by Hybertsen and Louie [10].

Many interesting systems can only be modelled if more than thousand atoms are used in the *GW* calculation. One way to reduce the computational cost is to reformulate *GW* in a smaller, more efficient basis: Plane-wave *GW* implementations commonly suffer from requiring many virtual states and the inversion of large dielectric matrices. Here, the combination of without-virtual-states techniques [14, 70, 167] with a low-rank approximation of the dielectric matrix [14, 168–171] can improve the computational efficiency enabling large-scale applications [172–174]. Another approach is to reformulate *GW* in a Gaussian basis which can significantly reduce the dimensionality of the involved matrices [11–13, 30, 37, 42, 161, 175–177]. *GW* in a Gaussian basis can be applied to molecules without difficulty [31, 34, 43, 47, 48, 71, 178–182] in contrast to plane-waves implementations where several technical issues have to be addressed [14, 52, 183].

Another way to minimize the computational cost of *GW* is to reduce its scaling from $O(N^4)$ to lower order. Already three low-scaling *GW* algorithms have been reported in the literature [20–22]: The cubic-scaling algorithm by Foerster *et al.* [20] employs a Gaussian basis and locality of electronic interactions. The method has been applied to molecules with a few tens of atoms.

Larger applications seem to lie out of reach at presence since a parallel implementation has not been published yet. The second low-scaling *GW* algorithm has been reported by Neuhauser *et al.* [21] which even scales linearly with the system size and relies on stochastic evaluation of the involved quantities. This algorithm can be easily parallelized and has been applied to a silicon nanocluster with one thousand atoms. However, it remains to be explored whether stochastic *GW* can be a useful tool for more complex systems than silicon nanoclusters [23]. The recent cubic-scaling *GW* algorithm by Liu *et al.* [22] is a variant of the *GW* space-time method by Rojas *et al.* [24]. In this algorithm, a plane-wave basis, real-space grids and sophisticated minimax quadratures [22, 76, 195, 248, 262, 263] in time and frequency domain are employed. The linear-scaling behaviour in the number of k-points seems to be promising when applying the method to large and numerically challenging periodic systems.

In this work, we present a cubic-scaling *GW* algorithm which is a reformulation of the *GW* space-time method [24] in a Gaussian basis employing the minimax time and frequency grids from Ref. [22]. By using Gaussian basis sets instead of plane waves, the size of involved matrices can be reduced substantially which makes the algorithm suitable to be applied to large systems. The algorithm is suited for molecules and materials of arbitrary periodicity in a Γ-point-only approach. In Sec. 6.2, we give details on the cubic-scaling *GW* algorithm. The algorithm is validated for the *GW*100 benchmark suite [71], see Sec. 6.3. Finally, we apply cubic-scaling *GW* to study fundamental gaps of graphene nanoribbons in Sec. 6.4 including a validation of the low-scaling behaviour in Sec. 6.5.

6.2 Method

We employ two different atom-centered Gaussian basis sets: ϕ_μ denote primary Gaussian basis functions and φ_P auxiliary Gaussian basis functions [30]. The primary basis $\{\phi_\mu\}$ is employed to expand the Kohn-Sham orbitals ψ_n using the molecular orbital (MO) coefficients $C_{n\mu}$,

$$\psi_n(\mathbf{r}) = \sum_\mu C_{n\mu}\phi_\mu(\mathbf{r}) \tag{6.1}$$

while the auxiliary basis $\{\varphi_P\}$ is used to expand *GW* quantities as the polarizability, the dielectric function and the screened Coulomb interaction.

Similarly to the *GW* space-time method [24], we compute the correlation self-energy in imaginary time as

$$\Sigma_n^{\mathrm{c}}(i\tau) = -\sum_{\nu P}\sum_\mu G_{\mu\nu}(i\tau)(n\mu P)\sum_Q \tilde{W}_{PQ}^{\mathrm{c}}(i\tau)(Q\nu n)\,. \tag{6.2}$$

The three-center overlap tensors

$$(n\mu P) = \int d\mathbf{r}\ \psi_n(\mathbf{r})\phi_\mu(\mathbf{r})\varphi_P(\mathbf{r}) \tag{6.3}$$

are computed analytically [195, 257] and originate from the resolution of the identity (RI) with the overlap metric [120, 195, 253–255, 280]. $(n\mu P)$ is vanishing if ϕ_μ and φ_P are located at atoms being far apart from each other introducing sparsity in $(n\mu P)$. Therefore, the computational complexity of Eq. (6.2) scales as $O(N_{GW}N^2)$ with the system size N, where N_{GW} is the number of computed *GW* energies.

The Green's function in Eq. (6.2) is computed in $O(N^3)$ operations using the eigenvalues ε_n from a previous DFT calculation and the corresponding Fermi level ε_F as [24]

$$G_{\mu\nu}(i\tau) = \begin{cases} \sum_{i}^{\text{occ}} C_{i\mu} C_{i\nu} \exp(-|(\varepsilon_i - \varepsilon_F)\tau|)\,, & \text{if } \tau < 0\,, \\ -\sum_{a}^{\text{virt}} C_{a\mu} C_{a\nu} \exp(-|(\varepsilon_a - \varepsilon_F)\tau|)\,, & \text{if } \tau > 0\,, \end{cases} \tag{6.4}$$

and the scaled screened Coulomb interaction is defined as

$$\tilde{\mathbf{W}}^c(i\tau) = \mathbf{S}^{-1}\mathbf{W}^c(i\tau)\mathbf{S}^{-1} \tag{6.5}$$

where $W^c_{PQ}(i\tau)$ is the correlation part of the screened Coulomb potential [163]. The overlap matrix

$$S_{PQ} = \int d\mathbf{r}\, \varphi_P(\mathbf{r})\varphi_Q(\mathbf{r}) \tag{6.6}$$

accounts for the non-orthogonality of the Gaussian basis.

We obtain $\mathbf{W}^c(i\tau)$ in Eq. (6.5) by a cosine transform from $\mathbf{W}^c(i\omega)$ employing minimax grids [22]. $\mathbf{W}^c(i\omega)$ is computed by [163]

$$\mathbf{W}^c(i\omega) = \mathbf{L}\left[\boldsymbol{\varepsilon}^{-1}(i\omega) - \mathbf{1}\right]\mathbf{L}^T\,, \tag{6.7}$$

where $\mathbf{L}$ is the Cholesky decomposition of the Coulomb matrix $\mathbf{V}$,

$$\mathbf{V} = \mathbf{L}\mathbf{L}^T\,, \quad V_{PQ} = \int d\mathbf{r}d\mathbf{r}'\, \varphi_P(\mathbf{r}) \frac{1}{|\mathbf{r} - \mathbf{r}'|} \varphi_Q(\mathbf{r}')\,. \tag{6.8}$$

For molecules, the Coulomb matrix is computed analytically [281] and for periodic systems by Ewald summation [196] which is commonly used for wavefunction correlation methods [76, 77, 80, 197, 199].

The symmetric dielectric function $\boldsymbol{\varepsilon}(i\omega)$ is computed by [163]

$$\boldsymbol{\varepsilon}(i\omega) = \mathbf{1} - \mathbf{L}^T\boldsymbol{\chi}^0(i\omega)\mathbf{L} \tag{6.9}$$

where we obtain the polarizability $\boldsymbol{\chi}^0(i\omega)$ by a cosine transform from $\boldsymbol{\chi}^0(i\tau)$. [248] We write [163]

$$\boldsymbol{\chi}^0(i\tau) = \mathbf{S}^{-1}\tilde{\boldsymbol{\chi}}^0(i\tau)\mathbf{S}^{-1} \tag{6.10}$$

and compute $\tilde{\boldsymbol{\chi}}^0(i\tau)$ as in the cubic-scaling random phase approximation (RPA) [195]

$$\tilde{\chi}^0_{PQ}(i\tau) = \sum_{\mu\sigma}\sum_{\lambda}(\lambda\sigma P)G_{\mu\lambda}(i\tau)\sum_{\nu}(\mu\nu Q)G_{\nu\sigma}(-i\tau)\,. \tag{6.11}$$

The computational cost of Eq. (6.11) scales quadratically with the system size since the three-index tensors $(\mu\nu P)$ are only non-vanishing if the Gaussians ϕ_μ, ϕ_ν and φ_P are centered on neighboring atoms. In this way, the memory of $(\mu\nu P)$ grows only in linear order with the system size. The computation time of the matrix-matrix multiplications in Eqs. (6.4) - (6.10) scales cubically with the system size. Despite the $O(N^2)$ scaling of Eq. (6.11), it remains the computational bottleneck even for the largest systems we address in this work. Therefore, the computation of the polarizability from Eq. (6.11) has been optimized for massively parallel use [195] employing libDBCSR, a library for sparse matrix-matrix multiplications [129, 282].

We obtain $\Sigma_n^c(i\omega)$ by a sine and cosine transform from $\Sigma_n^c(i\tau)$ in Eq. (6.2) employing minimax grids [22]. $\Sigma_n^c(\varepsilon)$ is computed by analytic continuation from a 16-parameter Pade approximant to $\Sigma_n^c(i\omega)$ [22, 71]. The final G_0W_0 quasiparticle energies $\varepsilon_n^{G_0W_0}$ are computed using

$$\varepsilon_n^{G_0W_0} = \varepsilon_n + \Sigma_n^x + \mathrm{Re}\,\Sigma_n^c(\varepsilon_n^{G_0W_0}) - v_n^{xc} \tag{6.12}$$

which is iteratively solved by the Newton-Raphson method. The bare-exchange self-energy is computed in $O(N^3)$ operations employing the resolution of the identity with the overlap metric,

$$\Sigma_n^x = -\sum_{\mu\nu} D_{\mu\nu} \sum_{PQ} (n\mu P)\tilde{V}_{PQ}(Q\nu n) \tag{6.13}$$

where $D_{\mu\nu} = \sum_i^{occ} C_{i\mu}C_{i\nu}$ and $\tilde{\mathbf{V}} = \mathbf{S}^{-1}\mathbf{V}\mathbf{S}^{-1}$.

The present algorithm can be applied to molecules and condensed phase systems with arbitrary periodicity in a Γ-point-only approach. For periodicity in three dimensions, decoupling of periodic images is achieved by a correction scheme using Gaussian basis functions [163].

6.3 Validation

For the validation of the cubic-scaling G_0W_0 algorithm, we compute the G_0W_0@PBE HOMO and LUMO by Eq. (6.12) for all molecules in the *GW*100 benchmark by van Setten *et al.* [71, 165, 183] For solving the all-electron Kohn-Sham (KS) equations, we employ the Gaussian and augmented plane waves scheme (GAPW) [283] as implemented in CP2K [73, 127]. The molecular orbitals are expanded in a def2-QZVP Gaussian basis [71], see Eq. (6.1). As auxiliary basis to expand *GW* quantities, we employ sufficiently large Gaussian basis sets to ensure excellent convergence.

We compare HOMOs and LUMOs computed with the $O(N^3)$ G_0W_0 algorithm for the *GW*100 test [71] to FHI-aims [13, 71] reference values in Fig. 6.1. The reference values are obtained from the $O(N^4)$-scaling FHI-aims code where an analytic continuation with a 16-pole model or a Pade-approximant has been used. It has been shown [71] that these values are in excellent agreement with values obtained from Turbomole [12] which makes the *GW*100 benchmark set a reliable suite for benchmarking. For the HOMO, we find that $O(N^3)$ G_0W_0 and FHI-aims values match within 0.03 eV for 74 out of 100 molecules, while for the LUMO, both methods agree within 0.03 eV for 87 molecules. The largest deviation for the HOMO to FHI-aims is observed for the Neon atom (−22.58 eV from $O(N^3)$-G_0W_0 vs. −20.38 eV from FHI-aims). In this case, generating the minimax grid could be numerically unstable due to the large gap of Neon. For the LUMO, the largest deviation is observed for the beryllium monooxide molecule (BeO) (−2.27 eV from $O(N^3)$-G_0W_0 vs. −2.56 eV from FHI-aims). The frequency integration and analytic continuation of the

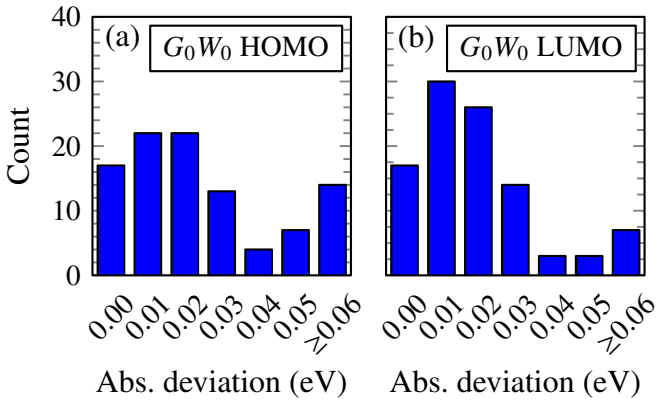

Figure 6.1: Benchmark of the G_0W_0@PBE (a) HOMO and (b) LUMO energies computed from the cubic-scaling *GW* algorithm from this work for the *GW*100 benchmark set [71]. Shown are the number of molecules with a given absolute derivation to 16-pole FHI-aims values [71]. We employ Gaussian basis sets which are identical as in Ref. [71] and minimax time and frequency grids with 12 points each.

BeO molecule is rather difficult to converge. This issue also appeared in Ref. [71] where the best FHI-aims and Turbomole values for the LUMO differed by 0.08 eV for BeO. This nevertheless overall good agreement of the $O(N^3)$-G_0W_0 algorithm to FHI-aims reference values enables high-quality GW studies of large systems, as we show in the next section.

6.4 Application: Graphene nanoribbons

As benchmark system, we employ anthenes, which are graphene nanoribbons (GNR) with seven carbon atoms width, see Fig. 6.2 (a) for the geometry. For solving the singlet open-shell Kohn-Sham (KS) equations, we employ the Gaussian and plane waves scheme (GPW) [27,284] together with Goedecker-Teter-Hutter pseudopotentials [130]. The molecular orbitals are expanded in an aug-DZVP Gaussian basis which gives rise to good convergence of the fundamental gap and already has been used in Ref. [30]. For the GW calculation, we employ 12 time and frequency points, respectively. As filter parameter for sparse tensor operations [Eqs. (6.2) and (6.11)], we use a threshold of 10^{-11} for atom blocks of basis functions [129]. All blocks with a Frobenius norm lower than this threshold are removed from the sparse tensor making the tensor multiplication more efficient. The filter threshold of 10^{-11} is much lower than the one used for water [195] which is due to the delocalized electronic structure of graphene nanoribbons compared to water.

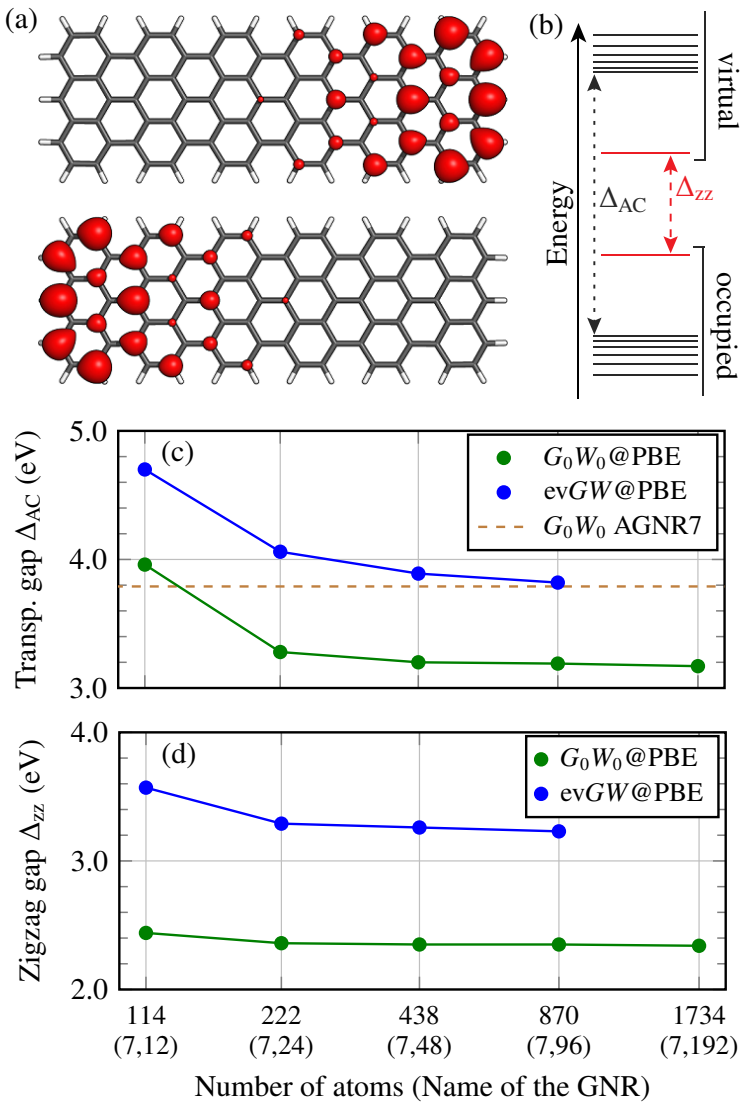

Figure 6.2: (a) Molecular geometry of the (7,12) GNR with seven carbon atoms in vertical direction and twelve horizontal atom rows together with an isosurface of the zigzag edge states obtained from PBE. (b) Sketch of the spectrum of the (7,12) AGNR with the HOMO-LUMO gap Δ_{zz} between zigzag (zz) states and the transport gap Δ_{AC} (HOMO-1-LUMO+1 gap) between bulk states. (c) Transport gap Δ_{AC} and (d) zigzag gap Δ_{zz} of anthenes for varying horizontal length of the anthene. We report G_0W_0@PBE results and eigenvalue-selfconsistent [11] (ev) GW@PBE results. Both gaps saturate when increasing the ribbon length.

Anthenes have been recently synthesized on a Au(111) surface and studied by scanning tunneling spectroscopy and many body perturbation theory [285]. It has been found that the highest occupied molecular orbital (HOMO) and the lowest unoccupied molecular orbital (LUMO) are localized at the zigzag edges of the ribbons what also is the result of a DFT calculation, see Fig. 6.2 (a). The energetic splitting between the HOMO and LUMO edge state is referred to as zigzag gap Δ_{zz}. The transport gap Δ_{AC} is defined as gap between the HOMO-1 and LUMO+1 state which are delocalized over the ribbon, see Fig. 6.2 (b).

We compute Δ_{zz} and Δ_{AC} for anthenes containing up to 1734 atoms, see Fig. 6.2 (c) and (d). We observe that the transport gap saturates from GNR (7,48) to GNR (7,192) at a value of 3.17 eV (G_0W_0@PBE), while the zigzag gap converges much faster as function of the ribbon length at a value of 2.34 eV (G_0W_0@PBE) what is in agreement with the experimental finding [285]. The transport gap of long anthenes directly relates to the fundamental gap of the periodic armchair GNR of seven atoms width (AGNR7) which e.g. have been computed in Ref. [286] by G_0W_0@PBE employing periodic boundary conditions, Coulomb cutoff techniques [287, 288] and a plasmon-pole model. The reported value [286] for the G_0W_0@PBE bandgap of periodic AGNR7 is 3.79 eV which is larger than the converged G_0W_0@PBE transport gap from GNR (7,192) of 3.17 eV. Here, agreement in this order of magnitude can be expected as plasmon-pole models can differ to full-frequency integration [71]. Eigenvalue-selfconsistency (evGW) has been shown to give improved fundamental gaps in organic semiconductors when compared to experimental data and high-level methods [11, 178]. We apply evGW to the anthenes and find that both gaps are enlarged, see Fig. 6.2 (b) and (c) where the evGW@PBE transport gap of GNR (7,96) is 3.82 eV. Interestingly, this value is in better agreement with the bandgap of periodic AGNR7 of 3.79 eV from Ref. [286]. Starting from 3.79 eV as gap of the AGNR7, it has been shown that applying an image-charge model [19] gives a bandgap of AGNR7 on a Au(111) surface which is in excellent agreement with the experimental finding [289].

6.5 Computational scaling

To demonstrate the low-scaling behaviour of the present *GW* algorithm, we show the execution time for the graphene nanoribbons from Sec. 6.4 in Fig. 6.3. The total execution time of cubic-scaling G_0W_0@PBE is given in green color and is scaling as $O(N^{2.1})$ with the number of atoms N. The high computational cost of Eq. (6.11) is scaling as $O(N^2)$ and therefore dominates the whole calculation what results in an overall scaling close to $O(N^2)$. The cubic-scaling steps are sketched

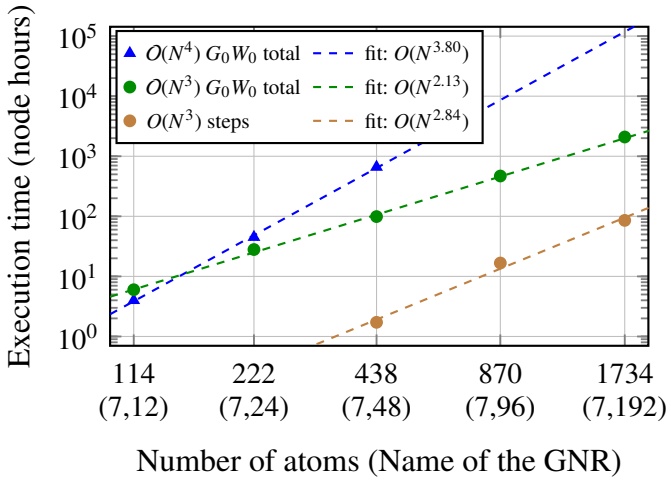

Figure 6.3: Execution time as function of the number of carbon atoms of anthenes from Sec. 6.4 on a CRAY XC40 machine. In blue, the execution time of the quartic-scaling algorithm [30] is sketched with a computational scaling of $O(N^{3.8})$ which has been determined by a two-parameter fit. In green, the execution time of the cubic-scaing *GW* algorithm from this work is shown with a computational scaling of $O(N^{2.1})$. The cubic-scaling steps in the cubic-scaling *GW* algorithm exhibit a scaling of $O(N^{2.8})$.

in brown color and are more than one order of magnitude less demanding than the quadratic-scaling steps. For the biggest system containing 1734 atoms, 2883 occupied molecular orbitals, 30195 virtual ones and 80940 auxiliary basis functions have been used. The quartic-scaling *GW* algorithm (blue color) is restricted to a nanoribbon with 438 atoms due to the rapid increase of computation time with the system size. For small systems below 150 atoms, quartic-scaling *GW* is more efficient since it is formulated in the occupied-virtual product basis $\{\psi_i\}\otimes\{\psi_a\}$ which is smaller than the Gaussian product basis $\{\phi_\mu\}\otimes\{\phi_\nu\}$ which is used in Eq. (6.11).

6.6 Conclusion

We have presented an algorithm for computing quasiparticle levels in the *GW* approximation in a Gaussian basis requiring $O(N^3)$ operations and $O(N^2)$ memory. The method is a combination of several known techniques: As first technique, we employ the resolution of the identity (RI) with the overlap metric as suggested by various authors [120, 253–255]. The advantage of RI with the overlap metric compared to RI with the Coulomb metric is that the occurring three-center overlap integrals are sparse [254, 255]. To exploit the sparsity of the three-center overlap integrals, we reformulate *GW* in the Gaussian basis. We follow the *GW* space-time method by Rojas *et al.* [24] and employ imaginary time and frequency integration using minimax grids [22]. We have applied cubic-scaling *GW* to compute the fundamental and the transport gap of graphene nanoribbons of seven atoms width and increasing length containing up to 1734 atoms. We find that the fundamental gap and the transport gap saturate when increasing the length. This saturation enables an alternative route to compute fundamental gaps of periodic one-dimensional materials from non-periodic calculations.

Chapter 7

Summary and Outlook

The whole work reported in this thesis has the goal to develop a cubic-scaling *GW* algorithm for computing quasiparticle energy levels in large molecular and periodic systems based on Gaussian basis functions. *GW* is a well-known method which has been used for many decades to accurately describe single-electron levels of materials, especially bandgaps. Recently, *GW* has been applied to molecules for studying the ionization potential, electron affinity and the fundamental gap where good agreement to experimental values has been obtained. An overview of the theoretical framework for *GW* is given in Chapter 2.

The early stage of this work has been focused on adapting the *GW* methodology to the Gaussian and plane waves (GPW) method (Chapter 3). This *GW* implementation can be applied to systems with several hundreds of atoms where the computational cost scales as $O(N^4)$ with the system size N as it is expected for a canonical *GW* implementation. *GW* has been applied to compute the bandgaps of closed-shell and broken-symmetry open-shell linear acenes, linear chains formed of connected benzene rings, as function of the acene length up to 11-acene. It has been found that the closed-shell and broken-symmetry open-shell bandgaps of acenes differ by up to 2.0 eV (for 11-acene). In experiments, a comparison of measured bandgaps and the calculated *GW* values of acenes may be helpful to determine whether their electronic ground state exhibits a closed-shell or polyradical configuration. This finding inspired experimentalists at the Swiss Federal Laboratories for Materials Science (EMPA) to measure reference data for acenes on noble-metal surfaces for a comparison. Since the synthesis of long acenes is very challenging, this is ongoing work.

If periodic boundary conditions are applied, the Γ-point-only *GW* algorithm featured an extremely slow convergence of the fundamental gap with the supercell size. A detailed analysis of this problem is given in Chapter 4 and a correction scheme for periodic Γ-point-only *GW* calculations based on GPW is presented. For four benchmark systems, the convergence of the corrected *GW* quasiparticle levels on the cell size is accelerated by a factor of three to ten compared to *GW* calculations without correction. The correction scheme comes along with negligible computational cost and can also be employed in the cubic-scaling *GW* algorithm.

The computationally most demanding step in *GW* is to calculate the inverse density response in the random phase approximation (RPA) which scales as $O(N^4)$. The scaling of this step can be reduced to $O(N^3)$ if RPA is reformulated in the Gaussian basis together with the resolution of the identity (RI) with the overlap metric. Moreover, imaginary time and imaginary frequency integration techniques as well as sparse linear algebra are necessary to compute the RPA density response in linear-scaling time (Chapter 5). Additional memory reduction without extra computations can be achieved by an iterative scheme which overcomes the memory bottleneck of canonical RPA. We report a massively parallel implementation which is the key for the application to large systems where more than ten thousand cores have been used. Since low-scaling algorithms are in

general by far more complex than canonical implementations, the parallelization has been a very challenging task. Most other low-scaling algorithms are only implemented serially. Based on the linear-scaling computation of the RPA density response, a cubic-scaling algorithm for the RPA correlation energy can be derived. This algorithm has been applied to two thousand water molecules using a correlation-consistent triple-zeta quality basis which is the largest RPA calculation that has been reported in the literature so far.

The cubic-scaling RPA algorithm has been employed to implement a cubic-scaling *GW* algorithm for computing highly accurate single-electron levels in molecules and solids (Chapter 6). As application of the cubic-scaling *GW* algorithm, an alternative route to compute the fundamental gap of periodic, one-dimensional armchair graphene nanoribbons from *GW* has been presented: The length of non-periodic ribbons is increased until convergence of the quasiparticle levels is reached. This approach neither requires periodic boundary conditions nor Coulomb cutoff techniques which can be problematic in *GW* calculations. Therefore, the cubic-scaling *GW* algorithm from this work opens the way for the high-accuracy computation of fundamental gaps of periodic low-dimensional materials from *GW*. The largest graphene nanoribbon that could be adressed with the cubic-scaling *GW* algorithm contains 1734 atoms which is the largest *GW* calculation that has been reported in the literature so far.

The work presented in this thesis gives rise to many possible follow-up projects in the direction of method development and applications.

Concerning method development, the massively parallel implementation of the RI with the overlap metric can be employed to construct low-scaling algorithms for exact exchange (EXX) or for scaled-opposite-spin MP2 (SOS-MP2). Also, low-scaling algorithms for forces based on RPA, EXX, and SOS-MP2 can be designed with the techniques presented in this work. A cubic-scaling version of *GW* in combination with the Bethe-Salpeter equation can be employed to study electronic excitation with high accuracy. The introduction of *k*-points in RPA and *GW* in the canonical and the low-scaling variant would open the way for highly accurate condensed phase simulations. Here, the low-scaling variants of RPA and *GW* from this work offer a possibility for linear scaling of the execution time when increasing the number of *k*-points.

Concerning applications, low-scaling *GW* enables calculations on large molecules which could not be treated before. Large molecular sizes are essential for graphene nanoribbons that can be synthesized on a noble-metal surface from molecular precursors. This new synthesis route has enabled the synthesis of atomically precise nanoribbons of unprecedented size. For probing the electronic structure of ribbons on the surface, scanning tunneling spectroscopy (STS) is employed which measures the local density of states at a given energy. In this way, the bandgap of ribbons can be determined. Together with image charge models, cubic-scaling *GW* can predict bandgaps of large ribbons on the noble metal surface. Comparing the bandgaps from *GW* and experimental values from STS measurements has shed light on the spin configuration of the ribbons. This is ongoing work in close collaboration with collegues from EMPA in Dübendorf.

Bibliography

[1] F. Studt, F. Abild-Pedersen, T. Bligaard, R. Z. Sørensen, C. H. Christensen, and J. K. Nørskov, *Identification of Non-Precious Metal Alloy Catalysts for Selective Hydrogenation of Acetylene*, Science **320**, 1320–1322 (2008).

[2] M. R. Filip, G. E. Eperon, H. J. Snaith, and F. Giustino, *Steric engineering of metal-halide perovskites with tunable optical band gaps*, Nat. Commun. **5**, 5757 (2014).

[3] Y. W. Son, M. L. Cohen, and S. G. Louie, *Energy Gaps in Graphene Nanoribbons*, Phys. Rev. Lett. **97**, 216803 (2006).

[4] J. Cai, C. A. Pignedoli, L. Talirz, P. Ruffieux, H. Söde, L. Liang, V. Meunier, R. Berger, R. Li, X. Feng, *et al.*, *Graphene nanoribbon heterojunctions*, Nat. Nanotechnol. **9**, 896–900 (2014).

[5] W. Kohn and L. J. Sham, *Self-Consistent Equations Including Exchange and Correlation Effects*, Phys. Rev. **140**, A1133 (1965).

[6] R. Koitz, A. P. Seitsonen, M. Iannuzzi, and J. Hutter, *Structural and electronic properties of a large-scale Moire pattern of hexagonal boron nitride on Cu(111) studied with density functional theory*, Nanoscale **5**, 5589–5595 (2013).

[7] S. Goedecker, *Linear scaling electronic structure methods*, Rev. Mod. Phys. **71**, 1085–1123 (1999).

[8] J. VandeVondele, U. Borštnik, and J. Hutter, *Linear Scaling Self-Consistent Field Calculations with Millions of Atoms in the Condensed Phase*, J. Chem. Theory Comput **8**, 3565–3573 (2012).

[9] L. Hedin, *New Method for Calculating the One-Particle Green's Function with Application to the Electron-Gas Problem*, Phys. Rev. **139**, A796–A823 (1965).

[10] M. S. Hybertsen and S. G. Louie, *Electron correlation in semiconductors and insulators: Band gaps and quasiparticle energies*, Phys. Rev. B **34**, 5390 (1986).

[11] X. Blase, C. Attaccalite, and V. Olevano, *First-principles GW calculations for fullerenes, porphyrins, phtalocyanine, and other molecules of interest for organic photovoltaic applications*, Phys. Rev. B **83**, 115103 (2011).

[12] M. J. van Setten, F. Weigend, and F. Evers, *The GW-Method for Quantum Chemistry Applications: Theory and Implementation*, J. Chem. Theory Comput. **9**, 232–246 (2013).

[13] X. Ren, P. Rinke, V. Blum, J. Wieferink, A. Tkatchenko, A. Sanfilippo, K. Reuter, and M. Scheffler, *Resolution-of-identity approach to Hartree–Fock, hybrid density functionals,*

RPA, MP2 and GW with numeric atom-centered orbital basis functions, New J. Phys. **14**, 053020 (2012).

[14] M. Govoni and G. Galli, *Large Scale GW calculations*, J. Chem. Theory Comput. **11**, 2680–2696 (2015).

[15] C. Friedrich, M. C. Müller, and S. Blügel, *Band convergence and linearization error correction of all-electron GW calculations: The extreme case of zinc oxide*, Phys. Rev. B **83**, 081101 (2011).

[16] R. R. Cloke, T. Marangoni, G. D. Nguyen, T. Joshi, D. J. Rizzo, C. Bronner, T. Cao, S. G. Louie, M. F. Crommie, and F. R. Fischer, *Site-Specific Substitutional Boron Doping of Semiconducting Armchair Graphene Nanoribbons*, J. Am. Chem. Soc. **137**, 8872–8875 (2015).

[17] J. B. Neaton, M. S. Hybertsen, and S. G. Louie, *Renormalization of Molecular Electronic Levels at Metal-Molecule Interfaces*, Phys. Rev. Lett. **97**, 216405 (2006).

[18] C. D. Spataru, *Electronic and optical gap renormalization in carbon nanotubes near a metallic surface*, Phys. Rev. B **88**, 125412 (2013).

[19] N. Kharche and V. Meunier, *Width and Crystal Orientation Dependent Band Gap Renormalization in Substrate-Supported Graphene Nanoribbons*, J. Phys. Chem. Lett. **7**, 1526–1533 (2016).

[20] D. Foerster, P. Koval, and D. Sánchez-Portal, *An $O(N^3)$ implementation of Hedin's GW approximation for molecules*, J. Chem. Phys. **135**, 074105 (2011).

[21] D. Neuhauser, Y. Gao, C. Arntsen, C. Karshenas, E. Rabani, and R. Baer, *Breaking the Theoretical Scaling Limit for Predicting Quasiparticle Energies: The Stochastic GW Approach*, Phys. Rev. Lett. **113**, 076402 (2014).

[22] P. Liu, M. Kaltak, J. Klimeš, and G. Kresse, *Cubic scaling GW: Towards fast quasiparticle calculations*, Phys. Rev. B **94**, 165109 (2016).

[23] V. Vlček, E. Rabani, D. Neuhauser, and R. Baer, *Stochastic GW calculations for molecules*, arXiv preprint arXiv:1612.08999 (2016).

[24] H. N. Rojas, R. W. Godby, and R. J. Needs, *Space-Time Method for Ab Initio Calculations of Self-Energies and Dielectric Response Functions of Solids*, Phys. Rev. Lett. **74**, 1827 (1995).

[25] G. Kresse and J. Furthmüller, *Efficient iterative schemes for ab initio total-energy calculations using a plane-wave basis set*, Phys. Rev. B **54**, 11169–11186 (1996).

[26] P. Ruffieux, S. Wang, B. Yang, C. Sánchez-Sánchez, J. Liu, T. Dienel, L. Talirz, P. Shinde, C. A. Pignedoli, D. Passerone, T. Dumslaff, F. Xinliang, K. Müllen, and R. Fasel, *On-surface synthesis of graphene nanoribbons with zigzag edge topology*, Nature **531**, 489–492 (2016).

[27] G. Lippert, J. Hutter, and M. Parrinello, *A hybrid Gaussian and plane wave density functional scheme*, Mol. Phys. **92**, 477–487 (1997).

[28] F. Hüser, T. Olsen, and K. S. Thygesen, *Quasiparticle GW calculations for solids, molecules, and two-dimensional materials*, Phys. Rev. B **87**, 235132 (2013).

[29] F. Hüser, *Quasiparticle GW calculations within the GPAW electronic structure code*, Ph.D. thesis, Technical University of Denmark (2013).

[30] J. Wilhelm, M. Del Ben, and J. Hutter, *GW in the Gaussian and Plane Waves Scheme with Application to Linear Acenes*, J. Chem. Theory Comput. **12**, 3623–3635 (2016).

[31] F. Bruneval and M. A. L. Marques, *Benchmarking the Starting Points of the GW Approximation for Molecules*, J. Chem. Theory Comput. **9**, 324–329 (2013).

[32] M. Kühn and F. Weigend, *One-Electron Energies from the Two-Component GW Method*, J. Chem. Theory Comput. **11**, 969–979 (2015).

[33] X. Ren, N. Marom, F. Caruso, M. Scheffler, and P. Rinke, *Beyond the GW approximation: A second-order screened exchange correction*, Phys. Rev. B **92**, 081104 (2015).

[34] C. Faber, P. Boulanger, C. Attaccalite, I. Duchemin, and X. Blase, *Excited states properties of organic molecules: from density functional theory to the GW and Bethe–Salpeter Green's function formalisms*, Phil. Trans. R. Soc. A **372**, 20130271 (2014).

[35] C. Faber, P. Boulanger, C. Attaccalite, E. Cannuccia, I. Duchemin, T. Deutsch, and X. Blase, *Exploring approximations to the GW self-energy ionic gradients*, Phys. Rev. B **91**, 155109 (2015).

[36] F. Bruneval, *Ionization energy of atoms obtained from GW self-energy or from random phase approximation total energies*, J. Chem. Phys. **136**, 194107 (2012).

[37] P. Koval, D. Foerster, and D. Sánchez-Portal, *Fully self-consistent GW and quasiparticle self-consistent GW for molecules*, Phys. Rev. B **89**, 155417 (2014).

[38] S.-H. Ke, *All-electron GW methods implemented in molecular orbital space: Ionization energy and electron affinity of conjugated molecules*, Phys. Rev. B **84**, 205415 (2011).

[39] F. Caruso, P. Rinke, X. Ren, A. Rubio, and M. Scheffler, *Self-consistent GW: All-electron implementation with localized basis functions*, Phys. Rev. B **88**, 075105 (2013).

[40] D. Jacquemin, I. Duchemin, and X. Blase, *Benchmarking the Bethe–Salpeter Formalism on a Standard Organic Molecular Set*, J. Chem. Theory Comput. **11**, 3290–3304 (2015).

[41] C. Faber, I. Duchemin, T. Deutsch, C. Attaccalite, V. Olevano, and X. Blase, *Electron-phonon coupling and charge-transfer excitations in organic systems from many-body perturbation theory*, J. Mater. Sci. **47**, 7472–7481 (2012).

[42] F. Kaplan, F. Weigend, F. Evers, and M. J. van Setten, *Off-Diagonal Self-Energy Terms and Partially Self-Consistency in GW Calculations for Single Molecules: Efficient Implementation and Quantitative Effects on Ionization Potentials*, J. Chem. Theory Comput. **11**, 5152–5160 (2015).

[43] J. W. Knight, X. Wang, L. Gallandi, O. Dolgounitcheva, X. Ren, J. V. Ortiz, P. Rinke, T. Körzdörfer, and N. Marom, *Accurate Ionization Potentials and Electron Affinities of Acceptor Molecules III: A Benchmark of GW Methods*, J. Chem. Theory Comput. **12**, 615–626 (2016).

[44] I. Duchemin, D. Jacquemin, and X. Blase, *Combining the GW formalism with the polarizable continuum model: A state-specific non-equilibrium approach*, J. Chem. Phys. **144**, 164106 (2016).

[45] P. Boulanger, D. Jacquemin, I. Duchemin, and X. Blase, *Fast and Accurate Electronic Excitations in Cyanines with the Many-Body Bethe–Salpeter Approach*, J. Chem. Theory Comput. **10**, 1212–1218 (2014).

[46] F. Bruneval, S. M. Hamed, and J. B. Neaton, *A systematic benchmark of the ab initio Bethe-Salpeter equation approach for low-lying optical excitations of small organic molecules*, J. Chem. Phys. **142**, 244101 (2015).

[47] S. Körbel, P. Boulanger, I. Duchemin, X. Blase, M. A. L. Marques, and S. Botti, *Benchmark Many-Body GW and Bethe–Salpeter Calculations for Small Transition Metal Molecules*, J. Chem. Theory Comput. **10**, 3934–3943 (2014).

[48] X. Blase, P. Boulanger, F. Bruneval, M. Fernandez-Serra, and I. Duchemin, *GW and Bethe-Salpeter study of small water clusters*, J. Chem. Phys. **144**, 034109 (2016).

[49] D. Jacquemin, I. Duchemin, and X. Blase, *Assessment of the convergence of partially self-consistent BSE/GW calculations*, Mol. Phys. **114**, 957–967 (2016).

[50] D. Jacquemin, I. Duchemin, and X. Blase, *0–0 Energies Using Hybrid Schemes: Benchmarks of TD-DFT, CIS(D), ADC(2), CC2, and BSE/GW formalisms for 80 Real-Life Compounds*, J. Chem. Theory Comput. **11**, 5340–5359 (2015).

[51] X. Gonze, *A brief introduction to the ABINIT software package*, Z. Kristallogr. **220**, 558–562 (2005).

[52] J. Deslippe, G. Samsonidze, D. A. Strubbe, M. Jain, M. L. Cohen, and S. G. Louie, *BerkeleyGW: A massively parallel computer package for the calculation of the quasiparticle and optical properties of materials and nanostructures*, Comput. Phys. Commun. **183**, 1269–1289 (2012).

[53] H. Jiang, R. I. Gómez-Abal, X.-Z. Li, C. Meisenbichler, C. Ambrosch-Draxl, and M. Scheffler, *FHI-gap: A code based on the all-electron augmented plane wave method*, Comput. Phys. Commun. **184**, 348–366 (2013).

[54] M. Shishkin and G. Kresse, *Implementation and performance of the frequency-dependent GW method within the PAW framework*, Phys. Rev. B **74**, 035101 (2006).

[55] M. Shishkin and G. Kresse, *Self-consistent GW calculations for semiconductors and insulators*, Phys. Rev. B **75**, 235102 (2007).

[56] M. Shishkin, M. Marsman, and G. Kresse, *Accurate Quasiparticle Spectra from Self-Consistent GW Calculations with Vertex Corrections*, Phys. Rev. Lett. **99**, 246403 (2007).

[57] F. Fuchs, J. Furthmüller, F. Bechstedt, M. Shishkin, and G. Kresse, *Quasiparticle band structure based on a generalized Kohn-Sham scheme*, Phys. Rev. B **76**, 115109 (2007).

[58] A. Marini, C. Hogan, M. Grüning, and D. Varsano, *yambo: An ab initio tool for excited state calculations*, Comput. Phys. Commun. **180**, 1392–1403 (2009).

[59] C. Friedrich, S. Blügel, and A. Schindlmayr, *Efficient implementation of the GW approximation within the all-electron FLAPW method*, Phys. Rev. B **81**, 125102 (2010).

[60] L. Martin-Samos and G. Bussi, *SaX: An open source package for electronic-structure and optical-properties calculations in the GW approximation*, Comput. Phys. Commun. **180**, 1416–1425 (2009).

[61] P. Umari, G. Stenuit, and S. Baroni, *Optimal representation of the polarization propagator for large-scale GW calculations*, Phys. Rev. B **79**, 201104 (2009).

[62] M. Usuda, N. Hamada, T. Kotani, and M. van Schilfgaarde, *All-electron* GW *calculation based on the LAPW method: Application to wurtzite ZnO*, Phys. Rev. B **66**, 125101 (2002).

[63] T. Kotani and M. van Schilfgaarde, *All-electron GW approximation with the mixed basis expansion based on the full-potential LMTO method*, Solid State Comm. **121**, 461–465 (2002).

[64] B. Arnaud and M. Alouani, *All-electron projector-augmented-wave GW approximation: Application to the electronic properties of semiconductors*, Phys. Rev. B **62**, 4464 (2000).

[65] J. A. Berger, L. Reining, and F. Sottile, *Efficient GW calculations for SnO_2, ZnO, and rubrene: The effective-energy technique*, Phys. Rev. B **85**, 085126 (2012).

[66] A. Kutepov, K. Haule, S. Y. Savrasov, and G. Kotliar, *Electronic structure of Pu and Am metals by self-consistent relativistic GW method*, Phys. Rev. B **85**, 155129 (2012).

[67] F. Aryasetiawan and O. Gunnarsson, *The GW method*, Rep. Prog. Phys. **61**, 237 (1998).

[68] G. Onida, L. Reining, and A. Rubio, *Electronic excitations: density-functional versus many-body Green's-function approaches*, Rev. Mod. Phys. **74**, 601 (2002).

[69] J. Lischner, S. Sharifzadeh, J. Deslippe, J. B. Neaton, and S. G. Louie, *Effects of self-consistency and plasmon-pole models on GW calculations for closed-shell molecules*, Phys. Rev. B **90**, 115130 (2014).

[70] P. Umari, G. Stenuit, and S. Baroni, *GW quasiparticle spectra from occupied states only*, Phys. Rev. B **81**, 115104 (2010).

[71] M. J. van Setten, F. Caruso, S. Sharifzadeh, X. Ren, M. Scheffler, F. Liu, J. Lischner, L. Lin, J. R. Deslippe, S. G. Louie, C. Yang, F. Weigend, J. B. Neaton, F. Evers, and P. Rinke, *GW100: Benchmarking G_0W_0 for Molecular Systems*, J. Chem. Theory Comput. **11**, 5665–5687 (2015).

[72] The CP2K developers group, CP2K is freely available from: http://www.cp2k.org/ (2017).

[73] J. Hutter, M. Iannuzzi, F. Schiffmann, and J. VandeVondele, *cp2k: atomistic simulations of condensed matter systems*, WIREs Comput. Mol. Sci. **4**, 15–25 (2014).

[74] M. Del Ben, J. Hutter, and J. VandeVondele, *Second-Order Møller–Plesset Perturbation Theory in the Condensed Phase: An Efficient and Massively Parallel Gaussian and Plane Waves Approach*, J. Chem. Theory Comput. **8**, 4177–4188 (2012).

[75] M. Del Ben, J. Hutter, and J. VandeVondele, *Electron Correlation in the Condensed Phase from a Resolution of Identity Approach Based on the Gaussian and Plane Waves Scheme*, J. Chem. Theory Comput. **9**, 2654–2671 (2013).

[76] M. Del Ben, O. Schütt, T. Wentz, P. Messmer, J. Hutter, and J. VandeVondele, *Enabling simulation at the fifth rung of DFT: Large scale RPA calculations with excellent time to solution*, Comput. Phys. Commun. **187**, 120–129 (2015).

[77] M. Del Ben, J. Hutter, and J. VandeVondele, *Forces and stress in second order Møller-Plesset perturbation theory for condensed phase systems within the resolution-of-identity Gaussian and plane waves approach*, J. Chem. Phys. **143**, 102803 (2015).

[78] M. Del Ben, M. Schönherr, J. Hutter, and J. VandeVondele, *Bulk Liquid Water at Ambient Temperature and Pressure from MP2 Theory*, J. Phys. Chem. Lett. **4**, 3753–3759 (2013).

[79] M. Del Ben, M. Schönherr, J. Hutter, and J. VandeVondele, *Correction to "Bulk Liquid Water at Ambient Temperature and Pressure from MP2 Theory"*, J. Phys. Chem. Lett. **5**, 3066–3067 (2014).

[80] M. Del Ben, J. VandeVondele, and B. Slater, *Periodic MP2, RPA, and Boundary Condition Assessment of Hydrogen Ordering in Ice XV*, J. Phys. Chem. Lett. **5**, 4122–4128 (2014).

[81] M. A. L. Marques, M. J. T. Oliveira, and T. Burnus, *Libxc: A library of exchange and correlation functionals for density functional theory*, Comput. Phys. Commun. **183**, 2272–2281 (2012).

[82] N. Marom, F. Caruso, X. Ren, O. T. Hofmann, T. Körzdörfer, J. R. Chelikowsky, A. Rubio, M. Scheffler, and P. Rinke, *Benchmark of GW methods for azabenzenes*, Phys. Rev. B **86**, 245127 (2012).

[83] V. Atalla, M. Yoon, F. Caruso, P. Rinke, and M. Scheffler, *Hybrid density functional theory meets quasiparticle calculations: A consistent electronic structure approach*, Phys. Rev. B **88**, 165122 (2013).

[84] N. Marom, X. Ren, J. E. Moussa, J. R. Chelikowsky, and L. Kronik, *Electronic structure of copper phthalocyanine from G_0W_0 calculations*, Phys. Rev. B **84**, 195143 (2011).

[85] C. Adamo and V. Barone, *Toward reliable density functional methods without adjustable parameters: The PBE0 model*, J. Chem. Phys. **110**, 6158 (1999).

[86] K. Okuno, Y. Shigeta, R. Kishi, H. Miyasaka, and M. Nakano, *Tuned CAM-B3LYP functional in the time-dependent density functional theory scheme for excitation energies and properties of diarylethene derivatives*, J. Photochem. Photobiol. A **235**, 29 (2012).

[87] *http://cccbdb.nist.gov* (accessed Jun 16, 2015).

[88] R. Korytár, D. Xenioti, P. Schmitteckert, M. Alouani, and F. Evers, *Signature of the Dirac cone in the properties of linear oligoacenes*, Nat. Commun. **5**, 5000 (2014).

[89] S. Kivelson and O. L. Chapman, *Polyacene and a new class of quasi-one-dimensional conductors*, Phys. Rev. B **728**, 7236 (1983).

[90] H. Katauro, Y. Kumazawa, Y. Maniwa, I. Umezu, S. Suzuki, Y. Ohtsuka, and Y. Achiba, *Optical Properties of Single-Wall Carbon Nanotubes*, Synt. Met. **103**, 2555–2558 (1999).

[91] J.-C. Charlier, X. Blase, and S. Roche, *Electronic and transport properties of nanotubes*, Rev. Mod. Phys. **79**, 677 (2007).

[92] K. Wakabayashi, M. Fujita, H. Ajiki, and M. Sigrist, *Electronic and magnetic properties of nanographite ribbons*, Phys. Rev. B **59**, 8271 (1999).

[93] M. Y. Han, B. Özyilmaz, Y. Zhang, and P. Kim, *Energy Band-Gap Engineering of Graphene Nanoribbons*, Phys. Rev. Lett. **98**, 206805 (2007).

[94] J. Wilhelm, M. Walz, and F. Evers, *Ab initio quantum transport through armchair graphene nanoribbons: Streamlines in the current density*, Phys. Rev. B **89**, 195406 (2014).

[95] A. H. Castro Neto, F. Guinea, N. M. R. Peres, K. S. Novoselov, and A. K. Geim, *The electronic properties of graphene*, Rev. Mod. Phys. **81**, 109 (2009).

[96] J. P. Perdew, K. Burke, and M. Ernzerhof, *Generalized Gradient Approximation Made Simple*, Phys. Rev. Lett. **77**, 3865 (1996).

[97] F. Plasser, H. Pašalić, M. H. Gerzabek, F. Libisch, R. Reiter, J. Burgdörfer, T. Müller, R. Shepard, and H. Lischka, *The Multiradical Character of One- and Two-Dimensional Graphene Nanoribbons*, Angew. Chem. Int. Ed. **52**, 2581–2584 (2013).

[98] J. Hachmann, J. J. Dorando, M. Avilés, and G. K.-L. Chan, *The radical character of the acenes: A density matrix renormalization group study*, J. Chem. Phys. **127**, 134309 (2007).

[99] M. Bendikov, H. M. Dong, K. Starkey, K. N. Houk, E. A. Carter, and F. Wudl, *Oligoacenes: theoretical prediction of open-shell singlet diradical ground states*, J. Am. Chem. Soc. **126**, 7416–7417 (2004).

[100] B. Hajgató, D. Szieberth, P. Geerlings, F. De Proft, and M. S. Deleuze, *A benchmark theoretical study of the electronic ground state and of the singlet-triplet split of benzene and linear acenes*, J. Chem. Phys. **131**, 224321 (2009).

[101] Z. Qu, D. Zhang, C. Liu, and Y. Jiang, *Open-Shell Ground State of Polyacenes: A Valence Bond Study*, J. Phys. Chem. A **113**, 7909–7914 (2009).

[102] E. S. Kadantsev, M. J. Stott, and A. Rubio, *Electronic structure and excitations in oligoacenes from ab initio calculations*, J. Chem. Phys. **124**, 134901 (2006).

[103] H. F. Bettinger, *Electronic structure of higher acenes and polyacene: The perspective developed by theoretical analyses*, Pure Appl. Chem. **82**, 905–915 (2010).

[104] G. Malloci, G. Cappellini, G. Mulas, and A. Mattoni, *Electronic and optical properties of families of polycyclic aromatic hydrocarbons: A systematic (time-dependent) density functional theory study*, Chem. Phys. **384**, 19–27 (2011).

[105] K. Kuribara, H. Wang, N. Uchiyama, K. Fukuda, T. Yokota, U. Zschieschang, C. Jaye, D. Fischer, H. Klauk, T. Yamamoto, K. Takimiya, M. Ikeda, H. Kuwabara, T. Sekitani, Y.-L. Loo, and T. Someya, *Organic transistors with high thermal stability for medical applications*, Nat. Commun. **3**, 723 (2012).

[106] Q. Miao, M. Lefenfeld, T.-Q. Nguyen, T. Siegrist, C. Kloc, and C. Nuckolls, *Self-Assembly and Electronics of Dipolar Linear Acenes*, Adv. Mater. **17**, 407–412 (2005).

[107] J. Shi and C. W. Tang, *Anthracene derivatives for stable blue-emitting organic electroluminescence devices*, Appl. Phys. Lett. **80**, 3201 (2002).

[108] M. Zhu, T. Ye, C.-G. Li, X. Cao, C. Zhong, D. Ma, J. Qin, and C. Yang, *Efficient Solution-Processed Nondoped Deep-Blue Organic Light-Emitting Diodes Based on Fluorene-Bridged Anthracene Derivatives Appended with Charge Transport Moieties*, J. Phys. Chem. C **115**, 17965–17972 (2011).

[109] T. Yelin, R. Korytár, N. Sukenik, R. Vardimon, B. Kumar, C. Nuckolls, F. Evers, and O. Tal, *Conductance saturation in a series of highly transmitting molecular junctions*, Nat. Mater. **15**, 1476 (2016).

[110] B. Kippelen and J.-L. Bredas, *Organic photovoltaics*, Energy Environ. Sci. **2**, 251–261 (2009).

[111] Y. Lin, Y. Li, and X. Zhan, *Small molecule semiconductors for high-efficiency organic photovoltaics*, Chem. Soc. Rev. **41**, 4245–4272 (2012).

[112] D. M. N. M. Dissanayake, A. A. D. T. Adikaari, and S. R. P. Silva, *Enhanced photovoltaic performance in nanoimprinted pentacene-PbS nanocrystal hybrid device*, Appl. Phys. Lett **92**, 093308 (2008).

[113] L. Huang, D. Rocca, S. Baroni, K. E. Gubbins, and M. B. Nardelli, *Molecular design of photoactive acenes for organic photovoltaics*, J. Chem. Phys. **130**, 194701 (2009).

[114] A. Szabo and N. S. Ostlund, *Modern Quantum Chemistry*, McGraw-Hill (1989).

[115] M. Guidon, F. Schiffmann, J. Hutter, and J. VandeVondele, *Ab initio molecular dynamics using hybrid density functionals*, J. Chem. Phys. **128**, 214104 (2008).

[116] M. Guidon, J. Hutter, and J. VandeVondele, *Robust Periodic Hartree-Fock Exchange for Large-Scale Simulations Using Gaussian Basis Sets*, J. Chem. Theory Comput. **5**, 3010–3021 (2009).

[117] J. Paier, C. V. Diaconu, G. E. Scuseria, M. Guidon, J. VandeVondele, and J. Hutter, *Accurate Hartree-Fock energy of extended systems using large Gaussian basis sets*, Phys. Rev. B **80**, 174114 (2009).

[118] J. L. Whitten, *Coulombic potential energy integrals and approximations*, J. Chem. Phys. **58**, 4496 (1973).

[119] B. I. Dunlap, J. W. D. Connolly, and J. R. Sabin, *On some approximations in applications of Xα theory*, J. Chem. Phys. **71**, 3396 (1979).

[120] O. Vahtras, J. Almlöf, and M. Feyereisen, *Integral approximations for LCAO-SCF calculations*, Chem. Phys. Lett. **213**, 514–518 (1993).

[121] F. Weigend, M. Häser, H. Patzelt, and R. Ahlrichs, *RI-MP2: optimized auxiliary basis sets and demonstration of efficiency*, Chem. Phys. Lett. **294**, 143–152 (1998).

[122] J. P. Boyd, *Exponentially convergent Fourier/Chebyshev quadrature schemes on bounded and infinite intervals*, J. Sci. Comput. **2**, 99–109 (1987).

[123] H. Eshuis, J. Yarkony, and F. Furche, *Fast computation of molecular random phase approximation correlation energies using resolution of the identity and imaginary frequency integration*, J. Chem. Phys. **132**, 234114 (2010).

[124] M. M. Rieger, L. Steinbeck, I. White, H. Rojas, and R. Godby, *The GW space-time method for the self-energy of large systems*, Comput. Phys. Commun. **117**, 211–228 (1999).

[125] T. A. Pham, H.-V. Nguyen, D. Rocca, and G. Galli, *GW calculations using the spectral decomposition of the dielectric matrix: Verification, validation, and comparison of methods*, Phys. Rev. B **87**, 155148 (2013).

[126] C. Friedrich, M. Betzinger, M. Schlipf, S. Blügel, and A. Schindlmayr, *Hybrid functionals and GW approximation in the FLAPW method*, J. Phys. Condens. Matter **24**, 293201 (2012).

[127] J. VandeVondele, M. Krack, F. Mohamed, M. Parrinello, T. Chassaing, and J. Hutter, *Quickstep: Fast and accurate density functional calculations using a mixed Gaussian and plane waves approach*, Comput. Phys. Commun. **167**, 103–128 (2005).

[128] J. VandeVondele and J. Hutter, *An efficient orbital transformation method for electronic structure calculations*, J. Chem. Phys **118**, 4365 (2003).

[129] U. Borštnik, J. VandeVondele, V. Weber, and J. Hutter, *Sparse matrix multiplication: The distributed block-compressed sparse row library*, Parallel Comput. **40**, 47–58 (2014).

[130] S. Goedecker, M. Teter, and J. Hutter, *Separable dual-space Gaussian pseudopotentials*, Phys. Rev. B **54**, 1703 (1996).

[131] M. Krack, *Pseudopotentials for H to Kr optimized for gradient-corrected exchange-correlation functionals*, Theor. Chem. Acc. **114**, 145–152 (2005).

[132] S. H. Vosko, L. Wilk, and M. Nusair, *Accurate spin-dependent electron liquid correlation energies for local spin density calculations: a critical analysis*, Can. J. Phys. **58**, 1200–1211 (1980).

[133] T. H. Dunning, *Gaussian basis sets for use in correlated molecular calculations. I. The atoms boron through neon and hydrogen*, J. Chem. Phys. **90**, 1007 (1989).

[134] D. E. Woon and T. H. Dunning, *Gaussian basis sets for use in correlated molecular calculations. III. The atoms aluminum through argon*, J. Chem. Phys. **98**, 1358 (1993).

[135] J. VandeVondele and J. Hutter, *Gaussian basis sets for accurate calculations on molecular systems in gas and condensed phases*, J. Chem. Phys. **127**, 114105 (2007).

[136] F. Weigend, A. Köhn, and C. Hättig, *Efficient use of the correlation consistent basis sets in resolution of the identity MP2 calculations*, J. Chem. Phys. **116**, 3175 (2002).

[137] L. Genovese, T. Deutsch, A. Neelov, S. Goedecker, and G. Beylkin, *Efficient solution of Poisson's equation with free boundary conditions*, J. Chem. Phys. **125**, 074105 (2006).

[138] M. Guidon, J. Hutter, and J. VandeVondele, *Auxiliary Density Matrix Methods for Hartree-Fock Exchange Calculations*, J. Chem. Theory Comput. **6**, 2348–2364 (2010).

[139] P. Merlot, R. Izsák, A. Borgoo, T. Kjærgaard, T. Helgaker, and S. Reine, *Charge-constrained auxiliary-density-matrix methods for the Hartree-Fock exchange contribution*, J. Chem. Phys. **141**, 094104 (2014).

[140] G. Nemeth, H. Selzle, and E. Schlag, *Magnetic ZEKE experiments with mass analysis*, Chem. Phys. Lett. **215**, 151–155 (1993).

[141] T. Yanai, D. P. Tew, and N. C. Handy, *A new hybrid exchange–correlation functional using the Coulomb-attenuating method (CAM-B3LYP)*, Chem. Phys. Lett. **393**, 51–57 (2004).

[142] G. Bieri, L. Åsbrink, and W. J. Niessen, *30.4-nm He (II) photoelectron spectra of organic molecules: Part VII. Miscellaneous compounds*, J. Electron. Spectrosc. Relat. Phenom. **27**, 129–178 (1982).

[143] L. Gallandi and T. Körzdörfer, *Long-Range Corrected DFT Meets GW: Vibrationally Resolved Photoelectron Spectra from First Principles*, J. Chem. Theory Comput. **11**, 5391–5400 (2015).

[144] K. Krause, M. E. Harding, and W. Klopper, *Coupled-cluster reference values for the GW27 and GW100 test sets for the assessment of GW methods*, Mol. Phys. **113**, 1952–1960 (2015).

[145] M. Del Ben, R. W. A. Havenith, R. Broer, and M. Stener, *Density Functional Study on the Morphology and Photoabsorption of CdSe Nanoclusters*, J. Phys. Chem. C **115**, 16782–16796 (2011).

[146] C. B. Murray, D. J. Norris, and M. G. Bawendi, *Synthesis and characterization of nearly monodisperse CdE (E = sulfur, selenium, tellurium) semiconductor nanocrystallites*, J. Am. Chem. Soc. **115**, 8706–8715 (1993).

[147] M. M. Sigalas, E. N. Koukaras, and A. D. Zdetsis, *Size dependence of the structural, electronic, and optical properties of $(CdSe)_n$, $n = 6 - 60$, nanocrystals*, RSC Adv. **4**, 14613–14623 (2014).

[148] A. Puzder, A. J. Williamson, F. Gygi, and G. Galli, *Self-Healing of CdSe Nanocrystals: First-Principles Calculations*, Phys. Rev. Lett. **92**, 217401 (2004).

[149] S. Kilina, S. Ivanov, and S. Tretiak, *Effect of Surface Ligands on Optical and Electronic Spectra of Semiconductor Nanoclusters*, J. Am. Chem. Soc. **131**, 7717–7726 (2009).

[150] M. L. del Puerto, M. L. Tiago, and J. R. Chelikowsky, *Excitonic Effects and Optical Properties of Passivated CdSe Clusters*, Phys. Rev. Lett. **97**, 096401 (2006).

[151] T. M. Inerbaev, A. E. Masunov, S. I. Khondaker, A. Dobrinescu, A.-V. Plamadă, and Y. Kawazoe, *Quantum chemistry of quantum dots: Effects of ligands and oxidation*, J. Chem. Phys. **131**, 044106 (2009).

[152] A. E. Kuznetsov and D. N. Beratan, *Structural and Electronic Properties of Bare and Capped $Cd_{33}Se_{33}$ and $Cd_{33}Te_{33}$ Quantum Dots*, J. Phys. Chem. C **118**, 7094–7109 (2014).

[153] S. A. Fischer, A. M. Crotty, S. V. Kilina, S. A. Ivanov, and S. Tretiak, *Passivating ligand and solvent contributions to the electronic properties of semiconductor nanocrystals*, Nanoscale **4**, 904–914 (2012).

[154] P. Deglmann, R. Ahlrichs, and K. Tsereteli, *Theoretical studies of ligand-free cadmium selenide and related semiconductor clusters*, J. Chem. Phys. **116**, 1585 (2002).

[155] M. Yu, G. W. Fernando, R. Li, F. Papadimitrakopoulos, N. Shi, and R. Ramprasad, *First principles study of CdSe quantum dots: Stability, surface unsaturations, and experimental validation*, Appl. Phys. Lett. **88**, 231910 (2006).

[156] A. Kasuya, R. Sivamohan, Y. A. Barnakov, I. M. Dmitruk, T. Nirasawa, V. R. Romanyuk, V. Kumar, S. V. Mamykin, K. Tohji, B. Jeyadevan, K. Shinoda, T. Kudo, O. Terasaki, Z. Liu, R. V. Belosludov, and Y. Sundararajan, Vand Kawazoe, *Ultra-stable nanoparticles of CdSe revealed from mass spectrometry*, Nat. Mater. **3**, 99 (2004).

[157] M. Solà, *Forty years of Clar's aromatic π-sextet rule*, Front. Chem. **1**, 22 (2013).

[158] Z. Sun, Z. Zeng, and J. Wu, *Benzenoid Polycyclic Hydrocarbons with an Open–Shell Biradical Ground State*, Chem. Asian J. **8**, 2894–2904 (2013).

[159] I. Kaur, M. Jazdzyk, N. N. Stein, P. Prusevich, and G. P. Miller, *Design, Synthesis, and Characterization of a Persistent Nonacene Derivative*, J. Am. Chem. Soc. **132**, 1261–1263 (2010).

[160] T. Rangel, K. Berland, S. Sharifzadeh, F. Brown-Altvater, K. Lee, P. Hyldgaard, L. Kronik, and J. B. Neaton, *Structural and excited-state properties of oligoacene crystals from first principles*, Phys. Rev. B **93**, 115206 (2016).

[161] F. Kaplan, M. E. Harding, C. Seiler, F. Weigend, F. Evers, and M. J. van Setten, *Quasi-Particle Self-Consistent GW for Molecules*, J. Chem. Theory Comput. **12**, 2528–2541 (2016).

[162] T. Rangel, S. M. Hamed, F. Bruneval, and J. B. Neaton, *Evaluating the GW Approximation with CCSD(T) for Charged Excitations Across the Oligoacenes*, J. Chem. Theory. Comput. **12**, 2834–2842 (2016).

[163] J. Wilhelm and J. Hutter, *Periodic GW calculations in the Gaussian and Plane Waves Scheme*, Phys. Rev. B (2017).

[164] C. Rostgaard, K. W. Jacobsen, and K. S. Thygesen, *Fully self-consistent GW calculations for molecules*, Phys. Rev. B **81**, 085103 (2010).

[165] F. Caruso, M. Dauth, M. J. van Setten, and P. Rinke, *Benchmark of GW Approaches for the GW100 Test Set*, J. Chem. Theory Comput. **12**, 5076–5087 (2016).

[166] P. Scherpelz, M. Govoni, I. Hamada, and G. Galli, *Implementation and Validation of Fully Relativistic GW Calculations: Spin–Orbit Coupling in Molecules, Nanocrystals, and Solids*, J. Chem. Theory Comput. **12**, 3523–3544 (2016).

[167] F. Bruneval, *Optimized virtual orbital subspace for faster GW calculations in localized basis*, J. Chem. Phys. **145**, 234110 (2016).

[168] M. Shao, L. Lin, C. Yang, F. Liu, F. H. Da Jornada, J. Deslippe, and S. G. Louie, Sci. China Math. **59**, 1593–1612 (2016).

[169] H.-V. Nguyen, T. A. Pham, D. Rocca, and G. Galli, *Improving accuracy and efficiency of calculations of photoemission spectra within the many-body perturbation theory*, Phys. Rev. B **85**, 081101 (2012).

[170] Y. Ping, D. Rocca, and G. Galli, *Electronic excitations in light absorbers for photoelectrochemical energy conversion: first principles calculations based on many body perturbation theory*, Chem. Soc. Rev. **42**, 2437–2469 (2013).

[171] F. Giustino, M. L. Cohen, and S. G. Louie, *GW method with the self-consistent Sternheimer equation*, Phys. Rev. B **81**, 115105 (2010).

[172] A. P. Gaiduk, M. Govoni, R. Seidel, J. H. Skone, B. Winter, and G. Galli, *Photoelectron Spectra of Aqueous Solutions from First Principles*, J. Am. Chem. Soc. **138**, 6912–6915 (2016).

[173] D. Opalka, T. A. Pham, M. Sprik, and G. Galli, *Electronic Energy Levels and Band Alignment for Aqueous Phenol and Phenolate from First Principles*, J. Phys. Chem. B **119**, 9651–9660 (2015).

[174] D. Opalka, T. Pham, M. Sprik, and G. Galli, *The ionization potential of aqueous hydroxide computed using many-body perturbation theory*, J. Chem. Phys. **141**, 034501 (2014).

[175] F. Bruneval, T. Rangel, S. M. Hamed, M. Shao, C. Yang, and J. B. Neaton, *molgw 1: Many-body perturbation theory software for atoms, molecules, and clusters*, Comp. Phys. Comm. **208**, 149–161 (2016).

[176] M. Rohlfing, P. Krüger, and J. Pollmann, *Quasiparticle band-structure calculations for C, Si, Ge, GaAs, and SiC using Gaussian-orbital basis sets*, Phys. Rev. B **48**, 17791–17805 (1993).

[177] M. Rohlfing, P. Krüger, and J. Pollmann, *Efficient scheme for GW quasiparticle band-structure calculations with applications to bulk Si and to the Si(001)-(2×1) surface*, Phys. Rev. B **52**, 1905–1917 (1995).

[178] T. Rangel, S. M. Hamed, F. Bruneval, and J. B. Neaton, *Evaluating the GW Approximation with CCSD(T) for Charged Excitations Across the Oligoacenes*, J. Chem. Theory Comput. **12**, 2834–2842 (2016).

[179] N. Marom, T. Körzdörfer, X. Ren, A. Tkatchenko, and J. R. Chelikowsky, *Size effects in the interface level alignment of dye-sensitized TiO2 clusters*, J. Phys. Chem. Lett. **5**, 2395–2401 (2014).

[180] N. Marom, *Accurate description of the electronic structure of organic semiconductors by GW methods*, J. Phys. Condens. Matter **29**, 103003 (2017).

[181] C. Faber, I. Duchemin, T. Deutsch, and X. Blase, *Many-body Green's function study of coumarins for dye-sensitized solar cells*, Phys. Rev. B **86**, 155315 (2012).

[182] X. Leng, J. Feng, T. Chen, C. Liu, and Y. Ma, *Optical properties of acene molecules and pentacene crystal from the many-body Green's function method*, Phys. Chem. Chem. Phys. **18**, 30777–30784 (2016).

[183] E. Maggio, P. Liu, M. J. van Setten, and G. Kresse, *GW100: A Plane Wave Perspective for Small Molecules*, J. Chem. Theory Comput. **13**, 635–648 (2017).

[184] C. Freysoldt, P. Eggert, P. Rinke, A. Schindlmayr, R. W. Godby, and M. Scheffler, *Dielectric anisotropy in the GW space–time method*, Comp. Phys. Comm. **176**, 1–13 (2007).

[185] J. McClain, Q. Sun, G. K.-L. Chan, and T. C. Berkelbach, *Gaussian-Based Coupled-Cluster Theory for the Ground-State and Band Structure of Solids*, J. Chem. Theory Comput. **13**, 1209–1218 (2017).

[186] Q. Sun, T. C. Berkelbach, N. S. Blunt, G. H. Booth, S. Guo, Z. Li, J. Liu, J. McClain, S. Sharma, S. Wouters, *et al.*, *The Python-based Simulations of Chemistry Framework (PySCF)*, arXiv preprint arXiv:1701.08223 (2017).

[187] F. Gygi and A. Baldereschi, *Self-consistent Hartree-Fock and screened-exchange calculations in solids: Application to silicon*, Phys. Rev. B **34**, 4405–4408 (1986).

[188] J. Spencer and A. Alavi, *Efficient calculation of the exact exchange energy in periodic systems using a truncated Coulomb potential*, Phys. Rev. B **77**, 193110 (2008).

[189] R. Sundararaman and T. A. Arias, *Regularization of the Coulomb singularity in exact exchange by Wigner-Seitz truncated interactions: Towards chemical accuracy in nontrivial systems*, Phys. Rev. B **87**, 165122 (2013).

[190] T. Kotani, M. van Schilfgaarde, and S. V. Faleev, *Quasiparticle self-consistent GW method: A basis for the independent-particle approximation*, Phys. Rev. B **76**, 165106 (2007).

[191] A. Yamasaki and T. Fujiwara, *Electronic Structure of Transition Metals Fe, Ni and Cu in the GW Approximation*, J. Phys. Soc. Jpn. **72**, 607–610 (2003).

[192] M. Gajdoš, K. Hummer, G. Kresse, J. Furthmüller, and F. Bechstedt, *Linear optical properties in the projector-augmented wave methodology*, Phys. Rev. B **73**, 045112 (2006).

[193] J. Yan, J. J. Mortensen, K. W. Jacobsen, and K. S. Thygesen, *Linear density response function in the projector augmented wave method: Applications to solids, surfaces, and interfaces*, Phys. Rev. B **83**, 245122 (2011).

[194] S. Baroni and R. Resta, *Ab initio calculation of the macroscopic dielectric constant in silicon*, Phys. Rev. B **33**, 7017–7021 (1986).

[195] J. Wilhelm, P. Seewald, M. Del Ben, and J. Hutter, *Large-Scale Cubic-Scaling Random Phase Approximation Correlation Energy Calculations Using a Gaussian Basis*, J. Chem. Theory Comput. **12**, 5851–5859 (2016).

[196] P. P. Ewald, *Die Berechnung optischer und elektrostatischer Gitterpotentiale*, Ann. Phys. **369**, 253–287 (1921).

[197] V. V. Rybkin and J. VandeVondele, *Spin-Unrestricted Second-Order Møller-Plesset (MP2) Forces for the Condensed Phase: From Molecular Radicals to F-Centers in Solids*, J. Chem. Theory Comput. **12**, 2214–2223 (2016).

[198] C. Spreafico and J. VandeVondele, *The nature of excess electrons in anatase and rutile from hybrid DFT and RPA*, Phys. Chem. Chem. Phys. **16**, 26144–26152 (2014).

[199] J. Cheng and J. VandeVondele, *Calculation of Electrochemical Energy Levels in Water Using the Random Phase Approximation and a Double Hybrid Functional*, Phys. Rev. Lett. **116**, 086402 (2016).

[200] C. Spreafico and J. VandeVondele, *Excess Electrons and Interstitial Li Atoms in TiO_2 Anatase: Properties of the (101) Interface*, J. Phys. Chem. C **119**, 15009–15018 (2015).

[201] M. J. McGrath, J. I. Siepmann, I.-F. Kuo, and C. J. Mundy, *Spatial correlation of dipole fluctuations in liquid water*, Mol. Phys. **105**, 1411–1417 (2007).

[202] M. J. McGrath, J. N. Ghogomu, C. J. Mundy, I.-F. W. Kuo, and J. I. Siepmann, *First principles Monte Carlo simulations of aggregation in the vapor phase of hydrogen fluoride*, Phys. Chem. Chem. Phys. **12**, 7678–7687 (2010).

[203] S. Luber, M. Iannuzzi, and J. Hutter, *Raman spectra from ab initio molecular dynamics and its application to liquid S-methyloxirane*, J. Chem. Phys. **141**, 094503 (2014).

[204] S. Luber, *Local electric dipole moments for periodic systems via density functional theory embedding*, J. Chem. Phys. **141**, 234110 (2014).

[205] P. Partovi-Azar and T. D. Kühne, *Efficient "On-the-Fly" calculation of Raman Spectra from Ab-Initio molecular dynamics: Application to hydrophobic/hydrophilic solutes in bulk water*, J. Comput. Chem. **36**, 2188–2192 (2015).

[206] S. Luber, *Sum Frequency Generation of Acetonitrile on a Rutile (110) Surface from Density Functional Theory-Based Molecular Dynamics*, J. Phys. Chem. Lett **7**, 5183–5187 (2016).

[207] J. G. Brandenburg, M. Alessio, B. Civalleri, M. F. Peintinger, T. Bredow, and S. Grimme, *Geometrical Correction for the Inter- and Intramolecular Basis Set Superposition Error in Periodic Density Functional Theory Calculations*, J. Phys. Chem. A **117**, 9282–9292 (2013).

[208] J. Klimeš, M. Kaltak, and G. Kresse, *Predictive GW calculations using plane waves and pseudopotentials*, Phys. Rev. B **90**, 075125 (2014).

[209] D. Nabok, A. Gulans, and C. Draxl, *Accurate all-electron G_0W_0 quasiparticle energies employing the full-potential augmented plane-wave method*, Phys. Rev. B **94**, 035118 (2016).

[210] M. J. van Setten, V. A. Popa, G. A. de Wijs, and G. Brocks, *Electronic structure and optical properties of lightweight metal hydrides*, Phys. Rev. B **75**, 035204 (2007).

[211] V. G. Plekhanov, V. A. Pustovarov, A. A. O'Konel-Bronin, T. A. Betenekova, and S. O. Cholakh, *Excitons and characteristics of exciton-phonon interaction in LiH and LiD*, Sov. Phys. Solid State Phys. **18**, 2438 (1976).

[212] H. Eshuis, J. Bates, and F. Furche, *Electron correlation methods based on the random phase approximation*, Theor. Chem. Acc. **131**, 1–18 (2012).

[213] X. Ren, P. Rinke, C. Joas, and M. Scheffler, *Random-phase approximation and its applications in computational chemistry and materials science*, J. Mater. Sci. **47**, 7447–7471 (2012).

[214] M. P. Johansson, I. Warnke, A. Le, and F. Furche, *At What Size Do Neutral Gold Clusters Turn Three-Dimensional?*, J. Phys. Chem. C **118**, 29370–29377 (2014).

[215] H. Eshuis and F. Furche, *A Parameter-Free Density Functional That Works for Noncovalent Interactions*, J. Phys. Chem. Lett. **2**, 983–989 (2011).

[216] M. Fuchs and X. Gonze, *Accurate density functionals: Approaches using the adiabatic-connection fluctuation-dissipation theorem*, Phys. Rev. B **65**, 235109 (2002).

[217] F. Furche and T. Van Voorhis, *Fluctuation-dissipation theorem density-functional theory*, J. Chem. Phys. **122**, 164106 (2005).

[218] A. Heßelmann and A. Görling, *Random-phase approximation correlation methods for molecules and solids*, Mol. Phys. **109**, 2473 (2011).

[219] J. Toulouse, I. C. Gerber, G. Jansen, A. Savin, and J. G. Ángyán, *Adiabatic-Connection Fluctuation-Dissipation Density-Functional Theory Based on Range Separation*, Phys. Rev. Lett. **102**, 096404 (2009).

[220] F. Furche, *Molecular tests of the random phase approximation to the exchange-correlation energy functional*, Phys. Rev. B **64**, 195120 (2001).

[221] F. Aryasetiawan, T. Miyake, and K. Terakura, *Total Energy Method from Many-Body Formulation*, Phys. Rev. Lett. **88**, 166401 (2002).

[222] H.-V. Nguyen and S. de Gironcoli, *Efficient calculation of exact exchange and RPA correlation energies in the adiabatic-connection fluctuation-dissipation theory*, Phys. Rev. B **79**, 205114 (2009).

[223] M. Del Ben, J. Hutter, and J. VandeVondele, *Probing the structural and dynamical properties of liquid water with models including non-local electron correlation*, J. Chem. Phys. **143**, 054506 (2015).

[224] L. Schimka, R. Gaudoin, J. Klimeš, M. Marsman, and G. Kresse, *Lattice constants and cohesive energies of alkali, alkaline-earth, and transition metals: Random phase approximation and density functional theory results*, Phys. Rev. B **87**, 214102 (2013).

[225] S. Lebègue, J. Harl, T. Gould, J. Ángyán, G. Kresse, and J. Dobson, *Cohesive properties and asymptotics of the dispersion interaction in graphite by the random phase approximation*, Phys. Rev. Lett **105**, 196401 (2010).

[226] X. Ren, P. Rinke, and M. Scheffler, *Exploring the random phase approximation: Application to CO adsorbed on Cu(111)*, Phys. Rev. B **80**, 045402 (2009).

[227] T. Olsen, J. Yan, J. J. Mortensen, and K. S. Thygesen, *Dispersive and Covalent Interactions between Graphene and Metal Surfaces from the Random Phase Approximation*, Phys. Rev. Lett. **107**, 156401 (2011).

[228] F. Mittendorfer, A. Garhofer, J. Redinger, J. Klimeš, J. Harl, and G. Kresse, *Graphene on Ni(111): Strong interaction and weak adsorption*, Phys. Rev. B **84**, 201401 (2011).

[229] L. Schimka, J. Harl, A. Stroppa, A. Grüneis, M. Marsman, F. Mittendorfer, and G. Kresse, *Accurate surface and adsorption energies from many-body perturbation theory*, Nat. Mater. **9**, 741–744 (2010).

[230] J. Harl, L. Schimka, and G. Kresse, *Assessing the quality of the random phase approximation for lattice constants and atomization energies of solids*, Phys. Rev. B **81**, 115126 (2010).

[231] J. Harl and G. Kresse, *Cohesive energy curves for noble gas solids calculated by adiabatic connection fluctuation-dissipation theory*, Phys. Rev. B **77**, 045136 (2008).

[232] M. Macher, J. Klimeš, C. Franchini, and G. Kresse, *The random phase approximation applied to ice*, J. Chem. Phys. **140**, 084502 (2014).

[233] T. Miyake, F. Aryasetiawan, T. Kotani, M. van Schilfgaarde, M. Usuda, and K. Terakura, *Total energy of solids: An exchange and random-phase approximation correlation study*, Phys. Rev. B **66**, 245103 (2002).

[234] B. Xiao, J. Sun, A. Ruzsinszky, J. Feng, and J. P. Perdew, *Structural phase transitions in Si and SiO_2 crystals via the random phase approximation*, Phys. Rev. B **86**, 094109 (2012).

[235] M. Rohlfing and T. Bredow, *Binding Energy of Adsorbates on a Noble-Metal Surface: Exchange and Correlation Effects*, Phys. Rev. Lett. **101**, 266106 (2008).

[236] A. Marini, P. García-González, and A. Rubio, *First-Principles Description of Correlation Effects in Layered Materials*, Phys. Rev. Lett. **96**, 136404 (2006).

[237] D. Lu, Y. Li, D. Rocca, and G. Galli, *Ab initio Calculation of van der Waals Bonded Molecular Crystals*, Phys. Rev. Lett. **102**, 206411 (2009).

[238] Y. Li, D. Lu, H.-V. Nguyen, and G. Galli, *van der Waals Interactions in Molecular Assemblies from First-Principles Calculations*, J. Phys. Chem. A **114**, 1944–1952 (2010).

[239] F. Göltl, A. Grüneis, T. Bučko, and J. Hafner, *Van der Waals interactions between hydrocarbon molecules and zeolites: Periodic calculations at different levels of theory, from density functional theory to the random phase approximation and Møller-Plesset perturbation theory*, J. Chem. Phys. **137**, 114111 (2012).

[240] J. Paier, X. Ren, P. Rinke, G. E. Scuseria, A. Grüneis, G. Kresse, and M. Scheffler, *Assessment of correlation energies based on the random-phase approximation*, New J. Phys. **14**, 043002 (2012).

[241] S. Grimme and M. Steinmetz, *A computationally efficient double hybrid density functional based on the random phase approximation*, Phys. Chem. Chem. Phys. **18**, 20926–20937 (2016).

[242] J. Toulouse, W. Zhu, J. G. Ángyán, and A. Savin, *Range-separated density-functional theory with the random-phase approximation: Detailed formalism and illustrative applications*, Phys. Rev. A **82**, 032502 (2010).

[243] W. Zhu, J. Toulouse, A. Savin, and J. G. Ángyán, *Range-separated density-functional theory with random phase approximation applied to noncovalent intermolecular interactions*, J. Chem. Phys. **132**, 244108 (2010).

[244] J. Harl and G. Kresse, *Accurate Bulk Properties from Approximate Many-Body Techniques*, Phys. Rev. Lett. **103**, 056401 (2009).

[245] T. Olsen and K. S. Thygesen, *Random phase approximation applied to solids, molecules, and graphene-metal interfaces: From van der Waals to covalent bonding*, Phys. Rev. B **87**, 075111 (2013).

[246] D. Rocca, *Random-phase approximation correlation energies from Lanczos chains and an optimal basis set: Theory and applications to the benzene dimer*, J. Chem. Phys. **140**, 18A501 (2014).

[247] J. E. Moussa, *Cubic-scaling algorithm and self-consistent field for the random-phase approximation with second-order screened exchange*, J. Chem. Phys. **140**, 014107 (2014).

[248] M. Kaltak, J. Klimeš, and G. Kresse, *Low Scaling Algorithms for the Random Phase Approximation: Imaginary Time and Laplace Transforms*, J. Chem. Theory Comput. **10**, 2498–2507 (2014).

[249] M. Kaltak, J. Klimeš, and G. Kresse, *Cubic scaling algorithm for the random phase approximation: Self-interstitials and vacancies in Si*, Phys. Rev. B **90**, 054115 (2014).

[250] M. Kállay, *Linear-scaling implementation of the direct random-phase approximation*, J. Chem. Phys. **142**, 204105 (2015).

[251] D. Neuhauser, E. Rabani, and R. Baer, *Expeditious Stochastic Calculation of Random-Phase Approximation Energies for Thousands of Electrons in Three Dimensions*, J. Phys. Chem. Lett. **4**, 1172–1176 (2013).

[252] Y. Gao, D. Neuhauser, R. Baer, and E. Rabani, *Sublinear scaling for time-dependent stochastic density functional theory*, J. Chem. Phys. **142**, 034106 (2015).

[253] H. F. Schurkus and C. Ochsenfeld, *Communication: An effective linear-scaling atomic-orbital reformulation of the random-phase approximation using a contracted double-Laplace transformation*, J. Chem. Phys. **144**, 031101 (2016).

[254] Y. Jung, A. Sodt, P. M. Gill, and M. Head-Gordon, *Auxiliary basis expansions for large-scale electronic structure calculations*, Proc. Natl. Acad. Sci. U.S.A. **102**, 6692–6697 (2005).

[255] S. Reine, E. Tellgren, A. Krapp, T. Kjærgaard, T. Helgaker, B. Jansik, S. Høst, and P. Salek, *Variational and robust density fitting of four-center two-electron integrals in local metrics*, J. Chem. Phys. **129**, 104101 (2008).

[256] O. Schütt, P. Messmer, J. Hutter, and J. VandeVondele, *GPU-Accelerated Sparse Matrix–Matrix Multiplication for Linear Scaling Density Functional Theory*, pages 173–190, John Wiley & Sons, Ltd (2016).

[257] S. Obara and A. Saika, *Efficient recursive computation of molecular integrals over Cartesian Gaussian functions*, J. Chem. Phys. **84**, 3963–3974 (1986).

[258] D. C. Lengreth and J. P. Perdew, *Exchange-correlation energy of a metallic surface: Wave-vector analysis*, Phys. Rev. B **15**, 2884 (1977).

[259] M. Häser and J. Almlöf, *Laplace transform techniques in Møller–Plesset perturbation theory*, J. Chem. Phys. **96**, 489 (1992).

[260] B. Doser, D. S. Lambrecht, J. Kussmann, and C. Ochsenfeld, *Linear-scaling atomic orbital-based second-order Møller–Plesset perturbation theory by rigorous integral screening criteria*, J. Chem. Phys. **130**, 064107 (2009).

[261] S. A. Maurer, L. Clin, and C. Ochsenfeld, *Cholesky-decomposed density MP2 with density fitting: Accurate MP2 and double-hybrid DFT energies for large systems*, J. Chem. Phys. **140**, 224112 (2014).

[262] A. Takatsuka, S. Ten-no, and W. Hackbusch, *Minimax approximation for the decomposition of energy denominators in Laplace-transformed Møller–Plesset perturbation theories*, J. Chem. Phys. **129**, 044112 (2008).

[263] D. Kats, D. Usvyat, S. Loibl, T. Merz, and M. Schütz, *Comment on "Minimax approximation for the decomposition of energy denominators in Laplace-transformed Møller–Plesset perturbation theories" [J. Chem. Phys. 129, 044112 (2008)]*, J. Chem. Phys. **130**, 127101 (2009).

[264] A. C. Ihrig, J. Wieferink, I. Y. Zhang, M. Ropo, X. Ren, P. Rinke, M. Scheffler, and V. Blum, *Accurate localized resolution of identity approach for linear-scaling hybrid density functionals and for many-body perturbation theory*, New J. Phys. **17**, 093020 (2015).

[265] S. V. Levchenko, X. Ren, J. Wieferink, R. Johanni, P. Rinke, V. Blum, and M. Scheffler, *Hybrid functionals for large periodic systems in an all-electron, numeric atom-centered basis framework*, Comp. Phys. Comm. **192**, 60–69 (2015).

[266] A. Sodt and M. Head-Gordon, *Hartree-Fock exchange computed using the atomic resolution of the identity approximation*, J. Chem. Phys. **128**, 104106 (2008).

[267] F. Della Sala and A. Görling, *Efficient localized Hartree–Fock methods as effective exact-exchange Kohn–Sham methods for molecules*, J. Chem. Phys. **115**, 5718–5732 (2001).

[268] C. Köppl and H.-J. Werner, *Parallel and Low-Order Scaling Implementation of Hartree–Fock Exchange Using Local Density Fitting*, J. Chem. Theory Comput. **12**, 3122–3134 (2016).

[269] E. Rebolini, R. Izsák, S. S. Reine, T. Helgaker, and T. B. Pedersen, *Comparison of Three Efficient Approximate Exact-Exchange Algorithms: The Chain-of-Spheres Algorithm, Pair-Atomic Resolution-of-the-Identity Method, and Auxiliary Density Matrix Method*, J. Chem. Theory Comput. **12**, 3514–3522 (2016).

[270] P. Merlot, T. Kjærgaard, T. Helgaker, R. Lindh, F. Aquilante, S. Reine, and T. B. Pedersen, *Attractive electron–electron interactions within robust local fitting approximations*, J. Comput. Chem. **34**, 1486–1496 (2013).

[271] J. Dziedzic, Q. Hill, and C.-K. Skylaris, *Linear-scaling calculation of Hartree-Fock exchange energy with non-orthogonal generalised Wannier functions*, J. Chem. Phys. **139**, 214103 (2013).

[272] C. Pisani, L. Maschio, S. Casassa, M. Halo, M. Schütz, and D. Usvyat, *Periodic local MP2 method for the study of electronic correlation in crystals: Theory and preliminary applications*, J. Comput. Chem. **29**, 2113–2124 (2008).

[273] L. Maschio, *Local MP2 with Density Fitting for Periodic Systems: A Parallel Implementation*, J. Chem. Theory Comput. **7**, 2818–2830 (2011).

[274] S. A. Maurer, J. Kussmann, and C. Ochsenfeld, *Communication: A reduced scaling J-engine based reformulation of SOS-MP2 using graphics processing units*, J. Chem. Phys. **141**, 051106 (2014).

[275] D. Kats, D. Usvyat, and M. Schütz, *On the use of the Laplace transform in local correlation methods*, Phys. Chem. Chem. Phys. **10**, 3430–3439 (2008).

[276] A. F. Izmaylov and G. E. Scuseria, *Resolution of the identity atomic orbital Laplace transformed second order Møller–Plesset theory for nonconducting periodic systems*, Phys. Chem. Chem. Phys. **10**, 3421–3429 (2008).

[277] P. Y. Ayala, K. N. Kudin, and G. E. Scuseria, *Atomic orbital Laplace-transformed second-order Møller–Plesset theory for periodic systems*, J. Chem. Phys. **115**, 9698–9707 (2001).

[278] P. Y. Ayala and G. E. Scuseria, *Linear scaling second-order Møller–Plesset theory in the atomic orbital basis for large molecular systems*, J. Chem. Phys. **110**, 3660–3671 (1999).

[279] J. Wilhelm, D. Golze, C. A. Pignedoli, and J. Hutter, in preparation (2017).

[280] I. Duchemin, J. Li, and X. Blase, *Hybrid and Constrained Resolution-of-Identity Techniques for Coulomb Integrals*, J. Chem. Theory Comput. **13**, 1199–1208 (2017).

[281] D. Golze, N. Benedikter, M. Iannuzzi, J. Wilhelm, and J. Hutter, *Fast evaluation of solid harmonic Gaussian integrals for local resolution-of-the-identity methods and range-separated hybrid functionals*, J. Chem. Phys. **146**, 034105 (2017).

[282] A. Lazzaro, J. VandeVondele, J. Hutter, and O. Schütt, *Increasing the Efficiency of Sparse Matrix-Matrix Multiplication with a 2.5 D Algorithm and One-Sided MPI*, arXiv preprint arXiv:1705.10218 (2017).

[283] G. Lippert, J. Hutter, and M. Parrinello, *The Gaussian and augmented-plane-wave density functional method for ab initio molecular dynamics simulations*, Theor. Chem. Acc. **103**, 124–140 (1999).

[284] D. Golze, M. Iannuzzi, and J. Hutter, *Local Fitting of the Kohn–Sham Density in a Gaussian and Plane Waves Scheme for Large-Scale Density Functional Theory Simulations*, J. Chem. Theory Comput. **13**, 2202–2214 (2017).

[285] S. Wang, L. Talirz, C. A. Pignedoli, X. Feng, K. Müllen, R. Fasel, and P. Ruffieux, *Giant edge state splitting at atomically precise graphene zigzag edges*, Nat. Commun. **7**, 11507 (2016).

[286] L. Yang, C.-H. Park, Y.-W. Son, M. L. Cohen, and S. G. Louie, *Quasiparticle Energies and Band Gaps in Graphene Nanoribbons*, Phys. Rev. Lett. **99**, 186801 (2007).

[287] C. A. Rozzi, D. Varsano, A. Marini, E. K. U. Gross, and A. Rubio, *Exact Coulomb cutoff technique for supercell calculations*, Phys. Rev. B **73**, 205119 (2006).

[288] S. Ismail-Beigi, *Truncation of periodic image interactions for confined systems*, Phys. Rev. B **73**, 233103 (2006).

[289] O. Deniz, C. Sánchez-Sánchez, T. Dumslaff, X. Feng, A. Narita, K. Müllen, N. Kharche, V. Meunier, R. Fasel, and P. Ruffieux, *Revealing the Electronic Structure of Silicon Intercalated Armchair Graphene Nanoribbons by Scanning Tunneling Spectroscopy*, Nano Lett. **17**, 2197–2203 (2017).

List of Publications

[9] J. Wilhelm and J. Hutter, *Periodic GW calculations in the Gaussian and plane waves scheme*, Phys. Rev. B **95**, 235123 (2017).

[8] D. Golze, N. Benedikter, M. Iannuzzi, J. Wilhelm, and J. Hutter, *Fast evaluation of solid harmonic Gaussian integrals for local resolution-of-the-identity methods and range-separated hybrid functionals*, J. Chem. Phys. **146**, 034105 (2017).

[7] J. Wilhelm, P. Seewald, M. Del Ben, and J. Hutter, *Large-Scale Cubic-Scaling Random Phase Approximation Correlation Energy Calculations Using a Gaussian Basis*, J. Chem. Theory Comput. **12**, 5851–5859 (2016).

[6] J. Wilhelm, M. Del Ben, and J. Hutter, *GW in the Gaussian and Plane Waves Scheme with Application to Linear Acenes*, J. Chem. Theory Comput. **12**, 3623–3635 (2016).

[5] J. Wilhelm, M. Walz, and F. Evers, *Ab initio spin-flip conductance of hydrogenated graphene nanoribbons: Spin-orbit interaction and scattering with local impurity spins*, Phys. Rev. B **92**, 014405 (2015).

[4] M. Walz, J. Wilhelm, and F. Evers, *Current Patterns and Orbital Magnetism in Mesoscopic dc Transport*, Phys. Rev. Lett. **113**, 136602 (2014).

[3] J. Wilhelm, M. Walz, and F. Evers, *Ab initio quantum transport through armchair graphene nanoribbons: Streamlines in the current density*, Phys. Rev. B **89**, 195406 (2014).

[2] N. Bajales, S. Schmaus, T. Miyamashi, W. Wulfhekel, J. Wilhelm, M. Walz, M. Stendel, A. Bagrets, F. Evers, S. Ulas, B. Kern, A. Böttcher, and M. M. Kappes, *C_{58} on Au(111): A scanning-tunnelling-microscopy study*, J. Chem. Phys. **138**, 104703 (2013).

[1] J. Wilhelm, M. Walz, M. Stendel, A. Bagrets, and F. Evers, *Ab initio simulations of scanning-tunneling-microscope images with embedding techniques and application to C_{58} dimers on Au(111)*, Phys. Chem. Chem. Phys. **15**, 6684–6690 (2013).

Acknowledgments

My sincere gratitude goes to Jürg Hutter for his generous support. I am grateful to him for sharing his wide experience in quantum chemistry. He also provided various resources to perform computations and to attend conferences and summer schools which I really enjoyed.

This work builds on the extensive computational MP2 and RPA methodology which has been developed and implemented by Mauro Del Ben. I kindly thank him for introducing me into his comprehensive code, for interesting discussions and remote support after moving to Berkeley.

Many thanks goes to Patrick Seewald for the pleasant collaborations on Gaussian integrals, sparse-tensor operations and the Hartree-Fock exchange. Hopefully, many people will enjoy the use of his sparse-tensor library and the Hartree-Fock in the future.

I deeply thank Carlo Pignedoli and Leopold Talirz for sharing their knowledge about graphene nanoribbons. This exciting application added substantial benefit to this thesis. I am also pleased to thank Vladimir Rybkin for remembering *GW* when he started his studies on the solvated electron and very interesting discussions on various topics.

Special thanks goes to Dorothea Golze for including me in the LRI integral team and sharing insights in *GW* beyond the numerics. Tiziano Müller is acknowledged for running the automated Fatman calculations. I kindly thank Andreas Glöß for constant technical support and Joost VandeVondele for useful help and discussions on the code.

Finally, I thank all former and current members of the Hutter group for the good time at UZH.